Aalto University
School of Chemical Engineering

Aalto University

School of Chemical Engineering

Degree Programme of Chemical, Biochemical and Materials Engineering

Janez Košir

Fabrication and characterization of suspended pyrolytic carbon microstructures in various pyrolysis temperatures

Thesis submitted for examination for the degree of Master of Science in Technology.

Espoo, 28th March 2019.

Supervisor	Prof. Sami Franssila
Thesis Advisor	M.Sc. Joonas Heikkinen

Aalto University
School of Chemical
Engineering

Aalto University, P.O. BOX 11000, 00076 AALTO
www.aalto.fi

Abstract of master's thesis

Author Janez Košir

Title of thesis Fabrication and characterization of suspended pyrolytic carbon microstructures in various pyrolysis temperatures

Degree Program Chemical, Biochemical and Materials Engineering

Major Functional Materials

Thesis supervisor Sami Franssila

Thesis advisor(s) / Thesis examiner(s) Joonas Heikkinen

Date 28.03.2019 **Number of pages** 98+7 **Language** English

Abstract

The aim of this Master's thesis is to fabricate and study the issues related to the fabrication of suspended C-MEMS microstructures, as well as to investigate the properties of unpatterned pyrolytic carbon films in relation to the pyrolysis temperatures. In recent years, suspended pyrolytic carbon microstructures have started to emerge as part of the next generation C-MEMS devices. Although the use of such structures can greatly improve the quality and expands the application of C-MEMS devices, suspended pyrolytic carbon microstructures are far more susceptible to fabrication issues than substrate-bound structures. So, in order to further advance the C-MEMS process we must first understand the underlying fabrication issues that these structures face.

Suspended SU-8 microstructures with varying shapes and sizes were prepared with the use of sacrificial layers and pyrolyzed in an inert atmosphere, in order to obtain suspended pyrolytic carbon microstructures. The structures were then analyzed in terms of their structural stability (optical microscope, SEM) and contraction (profilometer). The pyrolytic carbon films were prepared by pyrolyzing unpatterned SU-8 films at four different pyrolysis temperatures between 800 and 1100 °C. The films were characterized in terms of their electrical resistivity (4-point probe), crystallinity (Raman spectroscopy) and surface roughness (AFM).

During the fabrication process various issues were observed. This allowed us to determine a correlation between the shape and size of the microstructures with the specific fabrication issue, a potential reasoning as to why these issues would occur and how they can be avoided in the future. Based on the obtained results, a new analysis of the pyrolysis process was performed from a structural standpoint of SU-8 microstructures. Novel microstructures were also presented in the form of pyrolytic carbon cups, which show great promise as structures used for the trapping of micro and nanoparticles. Analysis of the pyrolytic carbon films show an increase in the electrical conductivity, surface roughness and crystallinity of the material with higher pyrolysis temperatures. The electrical resistivity drops from $1.29 \cdot 10^{-4}$ to $2.92 \cdot 10^{-5}$ Ωm as the pyrolysis temperature is increased from 800 to 1100 °C. At the same time, the surface roughness of the pyrolytic carbon films increases from 0.33 to 1.27 nm. The Raman spectra indicate a very high level of structural disorder and small crystallinity of the material. The crystallite size was calculated to increase from 6.45 to 9.15 nm with higher pyrolysis temperatures. Furthermore, detailed analysis of the Raman spectra also indicates a buildup of intrinsic stress at temperatures up to 1000 °C. Upon increasing the pyrolysis temperature further, the stress is gradually reduced from the material as the structure begins to anneal.

Keywords C-MEMS, photolithography, pyrolysis, pyrolytic carbon, SU-8

Preface

I would like to thank my thesis supervisor, professor Sami Franssila, for taking me into his research group and giving me the opportunity to conduct my Master's thesis under his guidance on such an interesting topic. I appreciate all the time that he has taken in order to provide me with very comprehensive feedback and comments on my thesis. Without his support, the thesis would not have been as coherent as it is.

Huge gratitude also goes to my thesis advisor, Joonas Heikkinen, who introduced me into the world of microfabrication, gave me very helpful advice during my experimental work and helped patiently guide me every step of the way. It has definitely been a steep learning curve for me, but a fulfilling one nonetheless. I would also like to thank Joonas for designing the photomasks used in my thesis and for carrying out the PECVD depositions.

Greatest thanks also go to my academic advisor Kirsi Yliniemi who offered tremendous support in my academic choices during my studies and has always been there for me when I needed her advice, for which I will always be grateful.

I would also like to thank my good friends Anna and Rubina for helping me keep my spirits up and for cheering me on all the way throughout my thesis. You have truly been great friends who were always there for me when I needed to take my mind off my thesis. A big thank you also go to all my ″FunMat″ peers that I've gotten to know during my studies and who made Aalto University truly feel like my second home.

In the end, I would especially like to thank my wonderful parents for all their love and support. Without you, none of this would have been possible!

Espoo, 28th of March 2019

Janez Košir

Table of Contents

Abbreviations and symbols

Abbreviations

3D	Three-dimensional
a-C	Amorphous carbon
AFM	Atomic force microscopy
BHF	Buffered oxide etch
C-MEMS	Carbon microelectromechanical systems
CNT	Carbon nanotubes
CVD	Chemical vapor deposition
DIW	Deionized water
DNQ	Diazonaphthoquinone
EELS	Electron energy loss spectroscopy
FWHM	Full width at half maximum
GBL	*gamma*-butyrolactone
HAR	High-aspect ratio
HMDS	Hexamethyldisilazane
IDA	Interdigitated array
ITO	Indium tin oxide
MEMS	Microelectromechanical systems
PECVD	Plasma-enhanced chemical vapor deposition
PGMEA	Propylene glycol methyl ether acetate
PVD	Physical vapor deposition
SC	Soft contact
SEM	Scanning electron microscopy
ta-C	Tetrahedral amorphous carbon
TEM	Transmission electron microscopy
UV	Ultraviolet
XPS	X-ray photoelectron spectroscopy
XRD	X-ray diffraction

Symbols

D	Exposure energy [J/cm^2]
E_l	Excitation laser energy [eV]
h_0	SU-8 film thickness [m]
h	Pyrolytic carbon film thickness [m]
I	Exposure intensity [W/cm^2]
$I_{(i)}$	Intensity of peak i
L	Length [m]
L_a	Intraplanar size of graphitic domains [nm]
R	Resistance [Ω]
R_s	Sheet resistance [Ω]
S_a	Mean surface roughness [nm]
T_g	Glass transition temperature [°C]
t	Time [s]
W	Width [m]
λ_l	Excitation laser wavelength [nm]
ρ	Resistivity [Ωm]

1. Introduction

Throughout the years, the various technological advancements have allowed for a progressive miniaturization of sensors, actuators and other mechanical devices. Their smaller size offers several benefits including, reduced weight, better portability, lower power consumption and higher precision [1]. The desire to reduce the size of such devices to microscopic levels has led to the development of microelectromechanical systems (MEMS).

MEMS refers to the technology of microscale integrated devices and miniature embedded systems. These devices are comprised of various physical microstructures, with sizes ranging from tens of nanometers to hundreds of microns. Due to their small size, the fabrication of microstructures requires a special set of microfabrication tools and techniques which allow for the patterning of bulk materials on such a small scale [1].

Within the last two decades, carbon materials have garnered a significant amount of attention as a material for MEMS fabrication. Carbon is a versatile element which can form several different allotropes, including graphite, diamond and amorphous carbon. The differences in the morphology and crystallinity between the various allotropes give carbon materials a wind range of attractive properties, such as a good electrical conductivity, high electrochemical stability, good mechanical stability and outstanding biocompatibility [2], [3]. In turn, this allows MEMS devices to be used in a variety of applications ranging from electrochemical sensors [2] and energy storage devices [4], [5] to substrates used in tissue engineering applications [6]. However, one of the biggest drawbacks of carbon materials is that the patterning of bulk carbons requires the use of complex etching techniques. This not only increase the fabrication times and costs, but also limits the geometry of the patterned microstructures [3]. In light of these issues, an alternative method to the fabrication of carbon microstructures was developed in the form of carbon microelectromechanical systems (C-MEMS).

C-MEMS refers to a set of tools and devices where carbon microstructures are derived through pyrolysis of a patterned photoactive polymer, i. e. photoresists, in an inert atmosphere. Pyrolysis leads to the thermal decomposition of the photoresist and outgassing of non-carbon atoms, leaving behind a carbon material known as pyrolytic carbon, which preserves the general shape of the precursor. Compared to the patterning of bulk carbons, patterning of photoresists is typically performed with the use of ultraviolet (UV) photolithography which is a much faster, simpler and less expensive patterning technique, thereby presenting C-MEMS as a far better method for the fabrication of carbon microstructures [3], [7].

Initially, C-MEMS technology was used for the fabrication of microstructures with very simple planar geometries [8]. With the development of photoresists and the photolithographic process, highly complex microstructures with extreme topographies could be fabricated [3]. In recent years, suspended pyrolytic carbon microstructures have started to emerge as part of the next generation C-MEMS devices, due to the numerous advantages that these structures can offer [9]–[11]. However, due to their complex geometry, the

fabrication of suspended C-MEMS still presents a significant challenge as these structures are far more susceptible to fabrication issues than substrate-bound structures.

To date, very little studies have been conducted that address the issues surrounding the fabrication of suspended C-MEMS microstructures [9], [12]. These studies can be very valuable as they allow us to better understand the fabrication methods and parameters that can be used in the development of suspended C-MEMS, thereby helping us to further develop the C-MEMS process.

Another issue with C-MEMS is that the properties of pyrolytic carbons are strongly related to the specific fabrication parameters, including the pyrolysis conditions [3], [13]–[21], choice of precursor [15]–[17], [22] as well as the geometry of the pyrolyzed structures [7], [17], [23]. Therefore, pyrolytic carbons can experience a poor repeatability of their morphology and show widely varying properties. Although several studies on the properties on pyrolytic carbons have been done in the past, further research is still needed in order to fully understand the correlation between the various fabrication parameters and the specific properties of pyrolytic carbons.

The aim of this work is to fabricate and study the issues related to the fabrication of suspended C-MEMS microstructures with varying shapes and sizes, as well as to investigate the properties of unpatterned pyrolytic carbon films in relation to the pyrolysis temperature. In both cases, the pyrolytic carbon was derived through pyrolysis of SU-8, a common photoresist used in C-MEMS fabrication, at four different pyrolysis temperatures between 800 and 1100 °C. The suspended microstructures were fabricated with the use of sacrificial layers with AZ 4562, a positive photoresist, as the sacrificial material. These structures were analyzed in terms of their contraction, structural stability as well as the fabrication issues that the structures would experience. This allowed us to determine a correlation between the shape and size of the microstructures with the specific fabrication issue, a potential reasoning as to why these issues would occur and how they can be avoided in the future. The pyrolytic carbon films were analyzed in terms of their electrical resistivity, surface roughness and crystallinity in relation to the pyrolysis temperature.

The thesis is divided into six sections. First, a general outlook on the fabrication of C-MEMS is conducted, along with the specific application and advantages of HAR and suspended pyrolytic carbon microstructures. Basic microfabrication techniques are also introduced as part of this section. Afterwards, pyrolytic carbon is analyzed in terms of its properties and crystal structures. The next section gives an outlook on the properties, photolithography and pyrolysis of SU-8. Various techniques used for the fabrication of suspended SU-8 microstructures are also presented in this section. Next, methodology and experimental details are presented, followed by the result and discussion. The conclusions are drawn in the final section.

2. Carbon microelectromechanical systems

Carbon microelectromechanical systems (C-MEMS) refers to the technology of micro-scale carbon devices and systems where carbon microstructures are derived through pyrolysis of patterned photoactive polymers in an inert atmosphere. The pyrolysis of the polymers leads to the outgassing of heteroatoms, leaving behind a highly disordered carbon material known as pyrolytic carbon. The pyrolytic carbon preserves the general shape of the precursor, thereby allowing for a relatively simple, fast and inexpensive fabrication method from which complex carbon micro and nanostructures can be obtained [3], [7].

Pyrolytic carbon is a highly disordered nanocrystalline graphitic carbon material whose specific structure and properties are strongly dependent on the fabrication parameters. The material exhibits several attractive properties, including a wide electrochemical stability window, excellent thermal and chemical stability, very high biocompatibility [3], good electrical conductivity, low gas permeability, as well as the ability of lithium intercalation/de-intercalation [4], thus making pyrolytic carbon an exceptionally good material for many MEMS applications. On top of that, the specific electrical, electrochemical and mechanical properties can easily be modified by optimizing the pyrolysis process [4]. A further discussion on the properties and crystal structure of pyrolytic carbon can be found in chapter 3.

Since pyrolytic carbon is derived directly through pyrolysis of the photoresist, the final quality, geometry and resolution of the carbon microstructures, as well as the cost of fabrication, predominantly depend on the properties of the precursor [4], [24]. One of the most commonly used photoresists in C-MEMS fabrication is SU-8 [7]. SU-8 is an epoxy-based negative photoresist whose large popularity comes courtesy of its exceptional chemical, mechanical and thermal properties, which allow for the fabrication of very complex microstructures with extreme topographies and high resolutions [7], [25], [26]. A further discussion on the properties and pyrolysis of SU-8 can be found in chapter 4.

Patterning of photoresists is typically performed with the use of UV photolithography, as it is a very fast, simple, inexpensive and highly reproducible technique which allows for batch processing. The use of photoresists in conjunction with UV photolithography make C-MEMS a much simpler and cost-effective technique for the fabrication of patterned carbon micro and nanostructures, as opposed to the patterning of bulk carbons [3]. A further discussion on the properties of photoresists as well as the photolithographic process can be found in section 2.2.1 and chapter 4. Figure 1 shows a schematic presentation for a typical C-MEMS fabrication process with the use of UV photolithography.

Today, C-MEMS are used in numerous different applications. These include their use as microelectrodes in electrochemical sensors [6], [9], [27]–[32] and Li-ion micro-batteries [4], [33], [34], carbon plates in proton-exchange membrane fuel cells [5], [35] as well as microelectrodes in micro-supercapacitors [36]. C-MEMS have also been used as a substrate for cell and tissue engineering applications [6], [37], microelectrodes in carbon-electrode dielectrophoretic applications [7], [23] as well as micro and nanomechanical resonators in resonant sensors [12].

Although C-MEMS have already successfully demonstrated their use in several different applications in the past, the designs of such systems are improving on a daily basis. The two most important factors, upon which the performance of C-MEMS depends upon, are the geometry microstructures and the properties of pyrolytic carbon [3], [7].

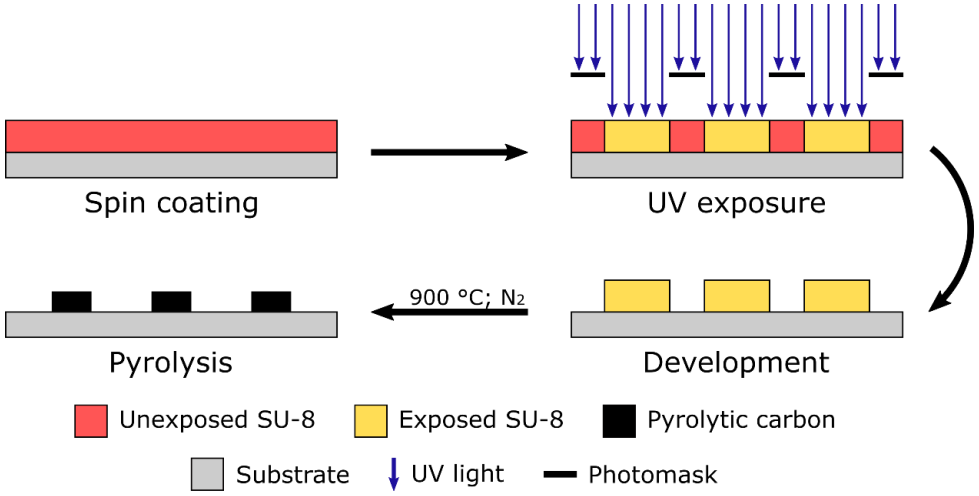

Figure 1: Schematic presentation of a typical C-MEMS fabrication process, through the use of UV photolithography of SU-8. First the photoresist is deposited on a rigid substrate by means of spin coating. Next the SU-8 is exposed through a photomask with UV light and developed, in order to obtain physical microstructures. The final step involves the pyrolysis of the photoresist in an inert atmosphere. The pyrolysis is typically performed at temperatures above 900 °C.

2.1 Geometry of C-MEMS microstructures

The geometry of the pyrolytic carbon microstructures plays an important role in the performance of C-MEMS devices. Initially, C-MEMS were used for the fabrication of carbon microstructures with very simple planar geometries [8]. Over time, the development of photoresists and advances in the photolithographic process allowed for a progressive move towards the fabrication of highly complex three-dimensional (3D) pyrolytic carbon microstructures with extreme topographies. Today, two of the most common types of structures encountered in C-MEMS devices include high-aspect ratio (HAR) and suspended microstructures [3]. The development of HAR and suspended pyrolytic carbon microstructures has gained a considerable amount of attention within the last decade due to the numerous benefits that such geometries can offer C-MEMS devices [6], [28], [29], [31], [33].

In general, the fabrication of complex 3D microstructures typically relies on the patterning of thick layers of a given material. This can often times be very difficult as the complexity for any fabrication process increases exponentially with an increasing material thickness [3]. Here, C-MEMS have a significant advantage over other common MEMS materials as photoresists allow for a much simpler deposition and patterning of very thick layers (up to hundreds of microns) within the matter of minutes [38], [39].

2.1.1 High-aspect ratio microstructures

High-aspect ratio microstructures are microstructures with a very high height-to-width ratio (typically 10:1 or more). The high aspect ratio of these structures significantly increases the surface-to-volume ratio of the material which can, in-turn, greatly enhance the performance of a selected C-MEMS device. HAR C-MEMS microstructures were first reported by Wang *et al.* [3], [33] in 2004 and have since become a staple of C-MEMS technology. Figure 2 shows scanning electron microscope (SEM) images of HAR C-MEMS scaffolds derived through pyrolysis of SU-8.

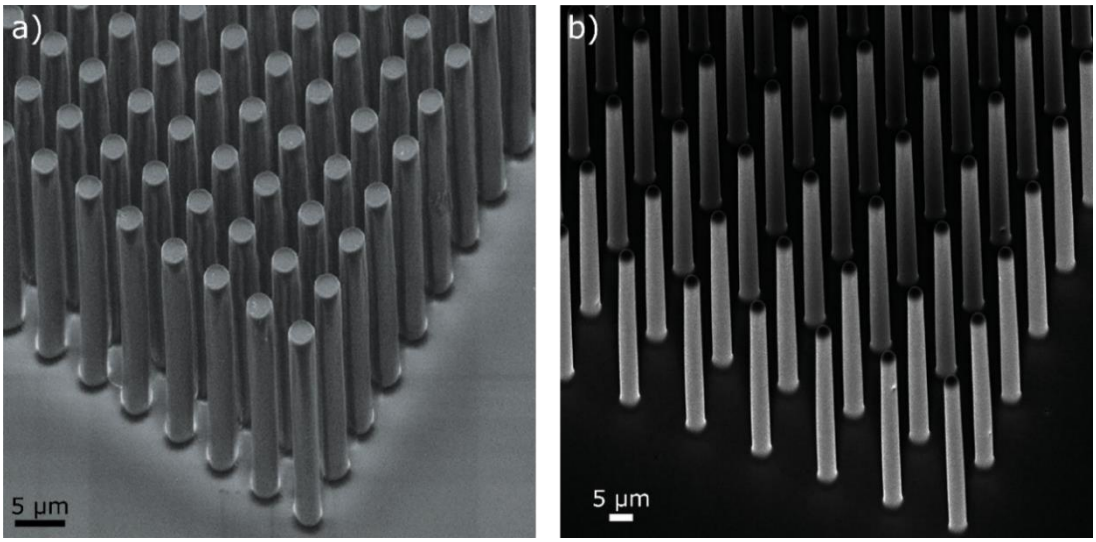

Figure 2: SEM images of HAR SU-8 scaffolds (a) before and (b) after pyrolysis [6].

One of the most common application of HAR C-MEMS microstructures is as microelectrodes in redox-based electrochemical sensors. Redox-based electrochemical sensors are used for the quantitative detection of ions and molecules, including glucose [40] and dopamine [6], [28], through redox reactions of the analyte. The redox reactions pass electrons between the electrode and electroactive species, thus generating an electric current proportional to the concentration of the analyte [27].

Redox-based electrochemical sensors commonly utilize microelectrodes in the form of interdigitated arrays (IDA), as seen in figure 3. IDA consist of two comb-shaped electrodes that are biased at different potentials, so that both oxidation and reduction reactions can occur within the system. This creates a sequence of alternating electrodes which allows for the analyte to undergo a redox cycling process between the two electrodes. Redox cycling of the analyte greatly increases the generated electric current, which amplifies the signal strength and lowers the detection limit of the analyte [27]. The performance of IDA microelectrodes can further be improved by reducing the distances between the electrode pairs and by increasing the overall surface area of the microelectrodes. A higher surface area allows for a greater number of simultaneous redox reactions to occur on the electrode surface, while smaller distances increase the diffusion flux of the electroactive species between the electrode pair. Both of these factors greatly increase the signal amplification factor and further lower the detection limit of the analyte [27].

HAR IDA microelectrodes offer several advantages over planar electrodes both in terms of reduced diffusion distances and increased surface areas. The small height of planar microelectrodes allows for the analyte to undergo a redox reaction only on the top of the electrode, as seen in figure 3 (a). This means that the diffusion path of the analyte, between the electrode pair, will not be linear but rather elliptical [27]. By implementing HAR microelectrodes, the vast majority of the analyte will undergo a redox reaction on the electrodes sidewalls, thus allowing for a linear diffusion between the electrode pair, as seen in figure 3 (b). The reduced distances of the linear diffusion pathways between the electrode sidewalls, compared to the longer curved diffusion paths over the top of the electrodes, increases the diffusion flux of the electroactive species, thus leading to enhanced redox cycling and greater signal amplification [27], [29]. The higher surface area of HAR microelectrodes also enhance the generated redox current due to the greater number of simultaneous redox reactions [27]. Furthermore, the increased height of the HAR structures also confines the analyte within the trenches of the electrodes for longer periods of time, allowing for higher number of redox cycles [29].

By utilizing 300 nm tall HAR IDA microelectrodes Heo *et al.* [27], [28] were able to achieve a signal amplification factor of 25, compared to a redox amplification factor of 5 for planar microelectrodes. Similarly, Kamath and Madou [29] were able to achieve a redox amplification factor of 37 with 1.1 µm tall HAR microelectrodes, compared to a redox amplification factor of 9 for planar microelectrodes. To put these values into perspective, a redox amplification factor of 37 allows for the detection of 5 µM of dopamine with of cyclic voltammetry [30].

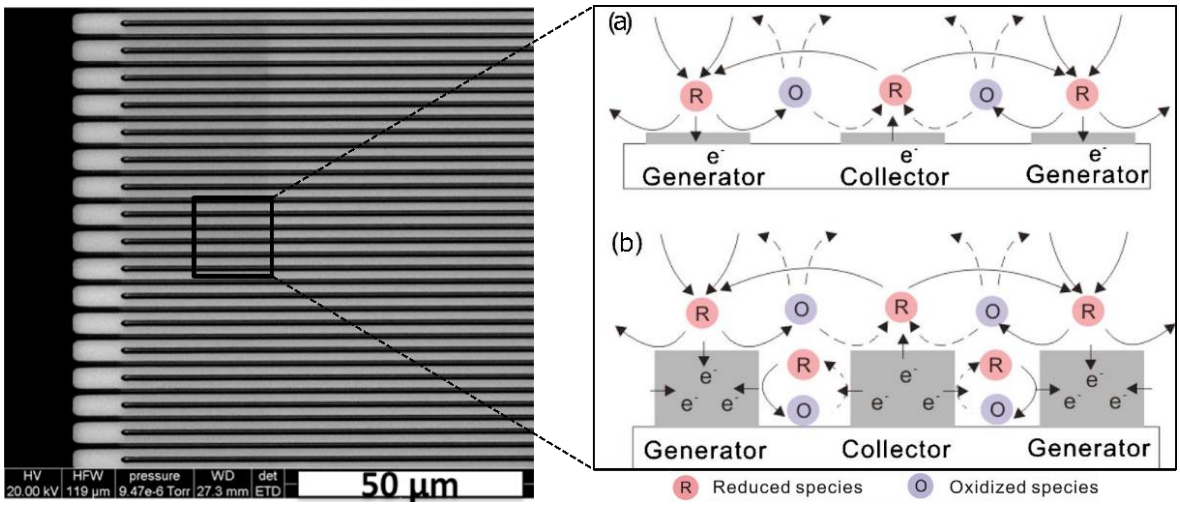

Figure 3: SEM image of pyrolytic carbon IDA microelectrodes with a schematic presentation on the principle of the redox cycling for (a) planar microelectrodes and (b) HAR microelectrodes [27], [41].

HAR C-MEMS microstructures have also been used successfully as microelectrodes in cell-based electrochemical biosensors [6]. Cell-based electrochemical sensors form a special group of biosensors in which a living cell is attached directly to the surface of an electrode, as seen in figure 4. This allows for the monitoring of a cell's extracellular activity and biopotential in real-time, by analyzing the released biomolecules and ions. Cell-based sensors can subsequently be used to study a cells response to various changes in its

surrounding environment and could potentially even be used to detect early onsets of severe neurological diseases, such as Parkinson's and Alzheimer's disease [42].

The use of HAR microstructures offer cell-based biosensors significant advantages over planar microelectrodes. For example, the high surface-to-volume ratio of HAR microstructures provides the cells a larger surface area to which the cells wan attach themselves to and enables the detection of a significantly larger fractions of released biomolecules [6], [37]. Furthermore, the 3D shape of the HAR microstructures mimics the cells natural environment much better than planar electrodes, leading to a more physiologically realistic and reliable response of the cell [6].

Similarly, HAR C-MEMS microstructures have also be used as a substrate for the growth and differentiation of neural stem cells [6]. The 3D environment has shown to provide cells with a much better structural support, thus enhancing their growth and promoting the formation of neural networks. Furthermore, the pyrolytic carbon substrate not only facilitates but also enhances the spontaneous differentiation of neural stem cells into dopaminergic neurons [6]. These systems could potentially be used to glow larger amounts of dopaminergic neurons which would then be transplanted in an attempt cure neurological diseases [43]. Figure 4 shows a comparison between neural cells attached to a planar pyrolytic carbon substrate and a HAR pyrolytic carbon substrate.

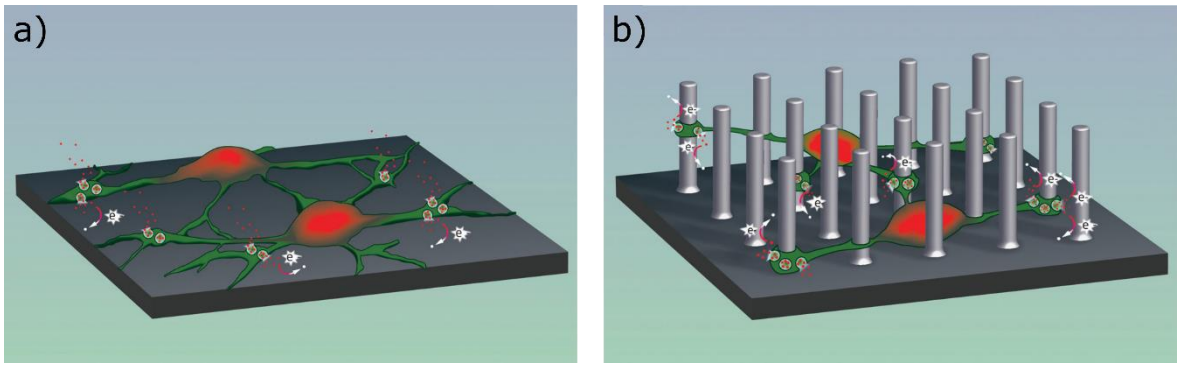

Figure 4: Schematic presentation of natural cells attached to a (a) planar substrate and (b) 3D substrate consisting of HAR pillars [6].

Another application of HAR C-MEMS is their use as microelectrodes in Li-ion micro-batteries. Wang *et al.* [4], [33] demonstrated that by utilizing 150 µm tall HAR pyrolytic carbon pillars, a nearly 80 % higher electrode capacity could be achieved compared to that of planar carbon films with the same surface area. The higher capacity came courtesy of the increased active volume of the HAR electrode, compared to planar carbon films [33]. By modifying the design of the HAR C-MEMS structures, Teixidor *et al.* [34] were able to further improve the capacity of the microelectrodes by three to six times, compared to that of planar carbon films with the same surface area. Similarly, HAR C-MEMS have also been used as microelectrodes in micro-supercapacitors where they were able to produce a very high specific capacitance of the device, due to a highly effective surface area of the microelectrodes [36].

2.1.2 Suspended microstructures

Suspended microstructures are structures that are suspended above the surface of the substrate. The suspended structure is attached to a substrate-bound structure, also known as an anchor point, which provides structural support to the suspended structure and enables the structure to be suspended above the substrate [44].

The design of suspended microstructures offers several advantages over traditional substrate-bound structures. For example, suspended structures are free from substrate interactions which can cause deleterious effects due to contaminations, temperature changes and the formation of stagnant layers [9], [10]. In electrochemical sensors, the analyte can approach a suspended structure from nearly all directions, thus enhancing the mass transport to and from the electrode [9], [11]. Another aspect of suspended microstructures are also the very large changes in the materials resistance due to various surface effects. This is particularly useful in electrochemical sensors that operate on the basis of changes in the materials resistance due to the adsorption of molecules onto the materials surface, as it greatly increases the sensors sensitivity [11].

Suspended C-MEMS were first developed by Wang *et al.* [3] in 2005. Although such structures have already been reported more than a decade ago, they have only begun to see widespread use within the last couple of years. To date, several different designs of suspended C-MEMS microstructures have been developed, many of which have also been successfully utilized in practical applications. These structures include wires/bridges [3], [4], [9]–[12], [44], [45], membranes/meshes [9], [30]–[32], [45], mushrooms [44] cantilevers [12] and plates [3], [4].

As with HAR C-MEMS microstructures, suspended C-MEMS microstructures are most commonly utilized as microelectrodes in redox based electrochemical sensors. Lim *et al.* [9], [30] and Lee *et al.* [31] developed a stacked C-MEMS microelectrode set consisting of a substrate-bound planar electrode located underneath a suspended pyrolytic carbon microelectrode mesh, as seen in figure 5. The design of the system has shown to offer several advantages over HAR IDA microelectrodes. For example, the electrode stack allows the analyte to reach the microelectrode set much easier than with HAR microelectrodes, while simultaneously confining the analyte between the electrodes for longer periods of time [31]. Furthermore, the suspended mesh experiences a much more uniform diffusion of the electroactive species throughout the entire surface of the electrode, in comparison to HAR microelectrodes, meaning that the electrodes surface is better utilized [31], [46]. Similarly, the suspended microelectrode stack also experiences a much more uniform electric field than HAR microelectrodes. A non-uniform electric field of HAR electrodes limits their efficiency in electrophoretic separation of an electroactive species, which a key applications of microelectrodes in microfluidic devices [31].

By utilizing the proposed microelectrode set, Lim *et al.* [30] and Lee *et al.* [31] were able to achieve a redox amplification factor of 37 and 29.7, respectively. Lee was later able to further increase the redox amplification factor by sealing off the top of the electrode stack with a polydimethylsiloxane (PDMS) plate. This resulted in a redox amplification factor of 74.7 for

cyclic voltammetry measurements and 839.7 for chronoamperometry measurements. Both of these results show massive improvements in the detection limits when compared to HAR IDA microelectrodes [29]. Lim also reported that a suspended nanowire would experience an almost 70 % increase in the redox current compared to that of a substrate-bound nanowire, indicating an increased mass transfer to the suspended microelectrode [9].

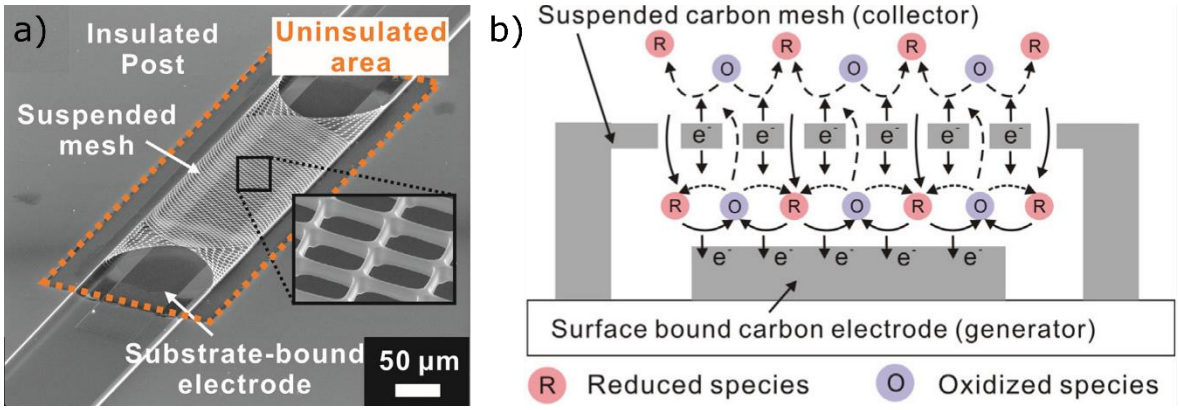

Figure 5: (a) SEM image of a stacked C-MEMS microelectrode set developed by Lee et al. [31] *and (b) a schematic presentation on the principles of redox cycling for the stacked microelectrode set* [30].

Another design of suspended C-MEMS was proposed by Lee *et al.* [44], who developed pyrolytic carbon mushrooms-shaped microstructures, as seen in figure 6. Although such structures have yet to see any practical implementations, their design could potentially be used as an inexpensive alternative to the golden mushroom microelectrodes developed by Hai *et al.* [47] and Ojovan *et al.* [48].

The golden mushroom microelectrodes were used as part of a cell-based sensor, in order to determine the intracellular activity of neural cells. Typically, measurements on the intracellular activity is performed by physically pushing a sharp microelectrode tip into the cell [47]. On the other hand, the specific geometry and size of the golden microelectrodes allowed for the neural cells to wrap themselves around the mushroom-shaped structures and completely engulf the microelectrodes. This, in turn, resulted in a signal indicative to the intracellular activities of the cells [48].

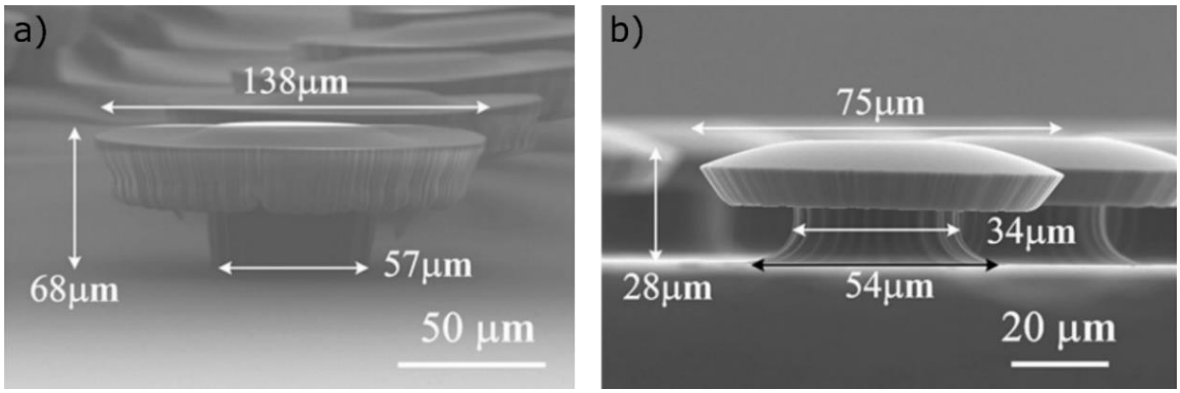

Figure 6: SEM images of SU-8 mushrooms-shaped microstructures (a) before and (b) after pyrolysis. After pyrolysis there is a clear reduction in size of the structure due to the shrinking of SU-8 [44].

Kurek *et al.* [12] also developed suspended C-MEMS wires and cantilevers which were used as micromechanical resonators in resonant sensors. Resonant sensors operate on the basis of changes in the resonant frequency of a structure due to external factors, such as the addition of mass or changes in temperature. The quality of such sensors strongly depends upon the presence of high levels of tensile stress within the resonating material. The tensile stress increases the energy stored in the resonator which, in turn, decreases the effect of energy loss on the resulting quality factor. This effect is also known as dumping dilution [12].

The C-MEMS resonators exhibited very high quality factors as pyrolysis of the resist generated a significant amount of stress within the pyrolytic carbon structures. Pyrolytic carbon also has an advantage in terms of its low density, which is more than two-times lower than that of silicon nitride. The low density provides C-MEMS resonators with a much higher sensitivity, over that of traditional MEMS resonators. Figure 7 shows SEM images of the pyrolytic carbon micromechanical resonators developed by Kurek *et al.* [12].

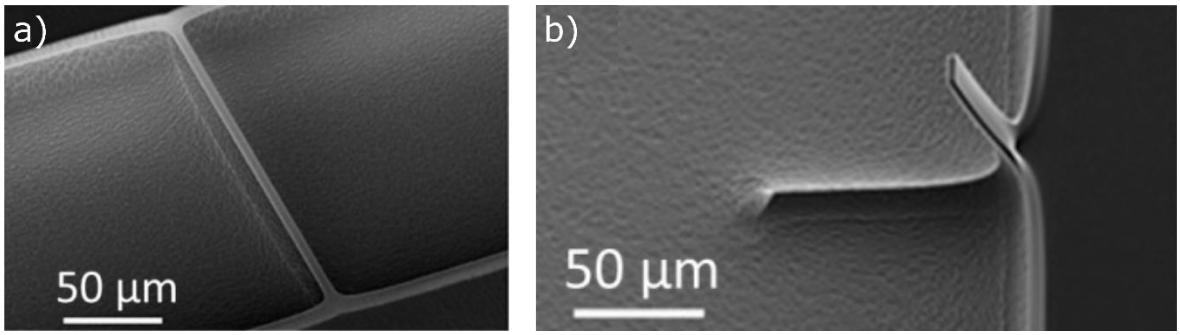

Figure 7: SEM images of pyrolytic carbon (a) wire and (b) cantilever resonators. The distinctive upward bend of the cantilever is caused by the uneven lateral contraction of the anchor points during pyrolysis [12].

2.2 Microfabrication

MEMS are comprised of numerous physical microstructures with sizes ranging from tens of nanometers to hundreds of microns. Due to their small size, the fabrication of microstructures requires a set of tools and processes that can operate on such a small scale with high levels of precision and consistency. Today, standard fabrication tools, such as drills, saws and lathes, have already been developed to the point where they are able to reach dimensional accuracies of less than one millimeter. However, as the size of structures is reduced towards the micro and nanoscale, these tools are no longer useful.

In 1959 physicist Richard Feynman had his famous talk “There's Plenty of Room at the Bottom” [49] in which he expressed the need for advancements in technologies that will be able to operate within micro and nanoworld. Throughout the years, a set of tools and techniques were developed which would allow for the fabrication of microstructures with high resolutions and high levels of consistency [39]. Today, these techniques are gathered under the name of microfabrication and include thin film deposition methods, photolithography and etching techniques, all of which are presented in figure 8. The specific process used in each step of development depends upon the material used, as well as the shape and size of the fabricated microstructures [39].

2.2.1 Photolithography

Photolithography is a microfabrication technique in which photoactive polymer films are patterned by selectively exposing them to light (typically UV light). It is one of the most fundamental microfabrication techniques not only in the development of C-MEMS, but also other MEMS devices. Photolithography includes the use of several components; (i) a photoresist which is to be patterned, (ii) a photomask, used to selectively expose the photoresist, (iii) an exposure tool/mask aligner, used to irradiate the photoresist as well as to align the photomask with the substrate, and (iv) a developer, used to selectively dissolve and remove the photoresist from the substrate based on the exposure patterns [39].

The key component of photolithography is the photoresist. Photoresists are polymeric materials which undergo various chemical changes when exposed to certain wavelengths of electromagnetic radiation, such as UV light or X-rays. They can be categorized into positive and negative photoresists, based upon how the material reacts when exposed. Upon exposure, positive photoresists will begin to soften and become more soluble in the developer. On the other hand, negative photoresists will begin to cross-link and harden when exposed, making them insoluble in the developer. This means that positive photoresists must be exposed in areas that will be remove from the substrate, while negative photoresist must be exposed in areas that will remain on the substrate [39].

Photoresists are comprised of three main components; (i) a polymeric resin, (ii) a solvent and (iii) a photoactive initiator. (i) The polymeric resin forms the matrix of the photoresist, which defines the mechanical and thermal properties of the material, as well as provides the developed microstructures with the required structural support. Typically, photoresists are comprised of either an epoxy or phenol formaldehyde resin. (ii) The primary function of the solvent is to modify the viscosity of the photoresist, thereby allowing it to be deposited by means of spin coating. The concentration of the solvent defines the thickness range in which the film can be deposited, whereby resists with higher viscosities can form thicker layers. (iii) The photoactive initiator is used to change and control the solubility of the polymeric resin upon exposure. By itself, the resin is typically not sensitive to exposure thus, a photoactive initiator is required in order to alter the properties of the resist. The photoinitiator is comprised of photoactive molecules which undergo various chemical changes when exposed. The newly formed molecules react with the polymeric resin thereby making it either more soluble (positive photoresists) or insoluble (negative photoresists) in the developer [25], [39].

Patterning of photoresists is done by exposing the material through a photomask. A photomask consists of various transparent and opaque patterns which selectively block the passage of light through the mask. The mask is placed between the radiation source and the substrate, resulting in a 1:1 transfer of the photomask pattern onto the photoresist during exposure [39]. Often times the photoresist patterns must correlate with other preexisting patterns on the substrate, thus the photomask and the substrate must be properly aligned prior to exposure. This is performed with the use of a mask aligner. Exposure of the photoresist can also be done without the use of a photomask, which is known as a flood exposure. Exposures are typically performed with wavelengths in the deep UV (150 – 300 nm) or near

UV (300 – 500 nm) range, and exposure energies between 10 and 500 mJ/cm^2, depending on the properties and thickness of the resist [38], [39].

After exposure, the substrate is immersed in a developer which dissolves the unpolymerized resist, thereby transforming the latent resist image, formed during exposure, into physical microstructures [39]. A schematic presentation of the main photolithographic steps along with the difference between positive and negative photoresists can be seen in figure 8.

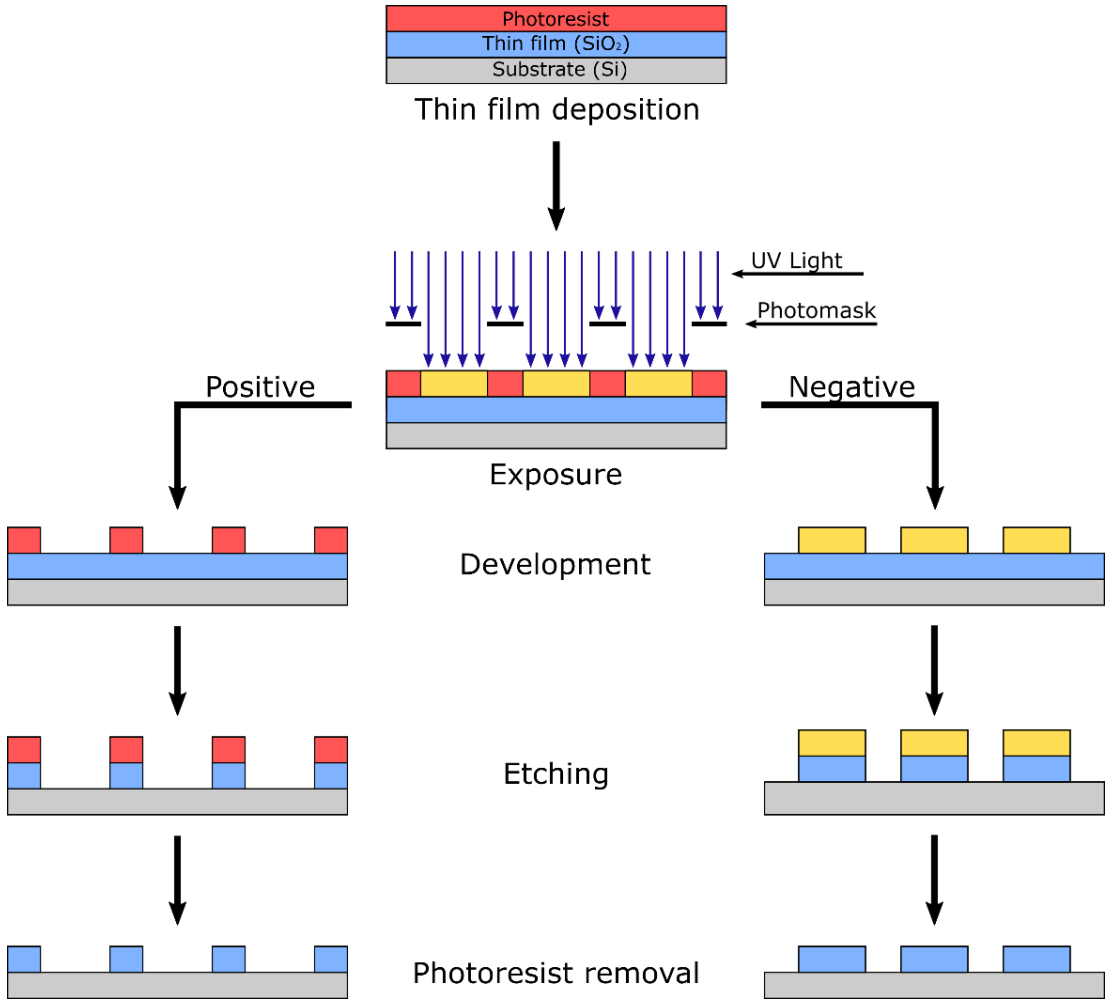

Figure 8: Schematic presentation of a basic microfabrication process, showcasing the difference between positive and negative photoresists. First, the materials are deposited on a substrate in the form of thin films. Next, the photoresist is patterned with the use of UV photolithography, where the material is exposed with UV light through a photomask, followed by a dissolution of the resist in a developer. Afterwards, the underlying layers can be patterned with the use of various etching techniques, while the patterned photoresist acts as an etching mask. Finally, the photoresist is removed from the substrate and the whole process can be repeated until all desired microstructures are fabricated.

Photoresists can be used either as a structural material, meaning that they will remain on the substrate as part of the final device, or as an intermediate material used in subsequent microfabrication processes, such as an etching mask for the underlying films or as a sacrificial layer used in lift-off processes [39]. A further discussion on the photolithographic process can be found in chapter 4.

2.2.2 Thin film deposition

Typically, microstructures are fabricated through the patterning of bulk materials. The small size of microstructures requires that the patterned materials be deposited on the substrate in the form of a thin film, with thicknesses ranging anywhere from a few nanometers to hundreds of microns. Due to their limiting thickness, the deposition of thin films is performed with special methods and tools that allow for a precise control over the films thickness, quality and uniformity. The depositions are generally performed on silicon wafers, although other substrates, such as quartz or glass wafers, can also be used [39].

The deposition methods for inorganic films can be divided into physical vapor deposition (PVD) and chemical vapor deposition (CVD) techniques [39]. On the other hand, organic photoresists are typically deposited through spin coating. A detailed description of the spin coating process can be found in chapter 4.

Physical vapor deposition

The general principle behind PVD methods is the ejection, transportation and condensation of atoms from a selected solid material that is to be deposited (a target), onto the surface of the substrate. These methods work by placing the substrate and target into a vacuum chamber and vaporizing the outermost layers of the target material. The ejected atoms spread throughout the vacuum chamber and deposit themselves on all available surfaces, including the substrate, in the form of a thin film. In order to reduce the deposition of the target material onto the chamber walls, the distance between the target and substrate must kept to a minimum. Two of the most common PVD methods include sputtering and evaporation [38].

Sputtering involves the ejection of atoms from the target material by bombarding the target with inert gas ions (typically Ar^+). The method works by introducing the ionic gas into the vacuum chamber and accelerating the ions towards the target. The energy of the accelerated ions is so great that they proceed to eject atoms from the outermost layers of the target material. The ejected atoms fill the vacuum chamber and deposit themselves on the substrate [39].

Evaporation, on the other hand, involves the use of heat in order to vaporize the outermost layers of the target material. The target can be heated either by means of resistive heating or with the use of high-intensity electron beams. The vaporized atoms travel towards the substrate where they deposit themselves in the form of a thin film [39].

Chemical vapor deposition

CVD methods operate on the principle of chemical reactions and/or thermal decomposition of precursor gases on the surface of the substrate. The deposition is performed by placing the substrate into a vacuum chamber, upon which the substrate is exposed to the precursor gases. The resulting reactions between the precursor gases form a solid thin film of a given material on the surface of the substrate [39].The reactions of the precursors can be induced either by a plasma (plasma enhanced CVD; PECVD) or by high temperatures (low-pressure CVD; LPCVD).

PECVD processes utilize a glow discharge in order to initiate the decomposition and/or reactions between the precursor gases. The process is typically performed at temperatures around 300 °C and is commonly used for the deposition of oxide and nitride films, including SiO_2 and Si_3N_4 [38]. The chemical reactions used for the PECVD deposition of SiO_2 and Si_3N_4 are presented in equations 1 and 2, respectively;

$$SiH_{4(g)} + 2\ N_2O_{(g)} \rightarrow SiO_{2(s)} + 2\ H_{2(g)} + 2\ N_{2(g)} \quad (1)$$

$$3\ SiH_{4(g)} + 4\ NH_{3(g)} \rightarrow Si_3N_{4(s)} + 12\ H_{2(g)} \quad (2)$$

2.2.3 Etching

Etching refers to the selective removal of a material from the substrate by chemical or physical means. The process if typically used in conjunction with photolithography as patterned photoresist can act as etching masks for the underlying layers. The etching mask works by protecting parts of the material that are covered by the mask, while the exposed areas are removed. This results in a 1:1 copy of the photoresist pattern onto the underlying layers [39].

In general, etching processes can be divided into wet and dry etching. Wet etching works by submerging the substrate into an etching solution. The etching solution reacts with the etched material, resulting in its dissolution in the etchant. Equations 3 and 4 show the reactions for the wet etching of SiO_2 and chromium with hydrofluoric acid (HF) and ceric ammonium nitrate ($(NH_4)_2[Ce(NO_3)_6]$), respectively [50], [51]:

$$SiO_{2(s)} + 4\ HF_{(l)} \rightarrow SiF_{4(aq)} + 2\ H_2O_{(l)} \quad (3)$$

$$3\ (NH_4)_2[Ce(NO_3)_6]_{(aq)} + Cr_{(s)} \rightarrow Cr(NO_3)_{3(aq)} + 3\ (NH_4)_2[Ce(NO_3)_5]_{(aq)} \quad (4)$$

Dry etching techniques utilize a vapor or plasma in order to etch the material by physical and/or chemical means. A commonly used dry etching technique is plasma etching, in which the etched material is bombarded with chemically reactive ions. The ions hit the etched material, creating chemical bonds with atoms located on the materials surface. If the newly formed bond is stronger than that of the existing bonds between the atoms, the resulting molecule detaches itself from the surface, thus slowly etching away the material [52].

Common etching rates, for both wet and dry etching, range between 10 and 1000 nm/min. Wet etching is typically more favorable as it allows for batch processing and does not require the use of expensive equipment (e. g. vacuum chamber) [38].

The etching process can be either isotropic or anisotropic. Isotropic etchants remove the material uniformly in all directions, resulting in a more rounded profile of the etched features. On the other hand, anisotropic etchants remove the material at varying rates, based on the direction of etching. This allows for a better control over the etching process, resulting in features with better resolutions and more defined cross-sectional profiles [52]. Figure 9 shows the etching profiles that are formed by the various etching methods.

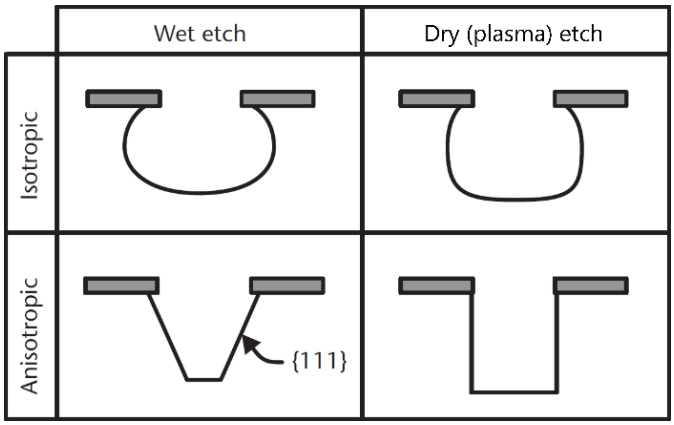

Figure 9: Schematic presentation of the cross-sections for various etching processes. Isotropic etchants produce much more rounded profiles in comparison to anisotropic etchants. The shaded areas represent the etching mask, which protects the underlying material [52].

Since isotropic etchants remove the material uniformly in all directions, they are capable of etching the material from underneath the etching mask. This effect is also known as undercutting and can present a significant issue as it reduces the resolution of the patterned microstructures and limits their geometry. For wet etchants, the level of undercutting is similar to the vertical etch depth, meaning that for a 500 nm tall structure the undercutting will also be approximately 500 nm [38].

Undercutting can be compensated by making the initial features of the etching mask larger than the desired size of the fabricated microstructures. While this approach works fairly well with isolated structures, it cannot be used for the fabrication of densely packed HAR arrays. Instead, other highly-complex patterning methods must be used, such as lift-off processes. On the other hand, undercutting can also be desirable as it can be used to release suspended microstructures from the substrate [38].

3. Pyrolytic carbon

Pyrolytic carbon is a highly disordered nanocrystalline graphitic carbon material, derived through pyrolysis of organic hydrocarbon precursors. Pyrolysis refers to the thermal decomposition of a material at elevated temperatures in an inert atmosphere [7]. The process is commonly used for the treatment of organic materials including polymers [13]–[17], [53], [54], gaseous hydrocarbons (e. g. acetylene and methane) [22], [55] and various forms of biomass [56]. The high temperatures cause several different reactions including, isomerization, cleaving of atomic bonds, outgassing of heteroatoms, dehydrogenation, rearrangement of carbon atoms and the formation of new carbon–carbon bonds [7], [57]. Today, pyrolysis is used in numerous industrial applications, from the synthesis of solid carbon materials [57] to the production of biofuels [56].

Pyrolytic carbons possess varying crystal structures and properties, which depend upon their specific fabrication parameters. These parameters include the chemistry of the precursor [15]–[17], [22], [57], pyrolysis conditions [3], [13]–[21], the shape and size of the precursor [7], [17], [23] an even the forces that act upon the precursor during pyrolysis [58]. Studies have shown that the primary factor that defines the nature of pyrolytic carbon is the chemical composition of the precursor [57]. Since C-MEMS technology is based around the use of photoactive polymers as a precursor material, in this chapter we will be primarily focusing on photoresist-derived pyrolytic carbons. A further discussion on the pyrolysis of SU-8 can be found in chapter 4.

The nature of carbon

To better understand the properties of pyrolytic carbons, we must first have a look at the underlying nature of carbon atoms. Elemental carbon can form three different hybridizations of its atomic orbitals; sp^1, sp^2 and sp^3. The ability of carbon atoms to possess different hybridizations allows carbon to form numerous allotropes with varying morphologies and crystallinities. Carbon films are predominantly comprised of sp^2 and/or sp^3 hybridized atoms, while sp^1 hybridizations are mainly present in chain-like linear structures [59].

In the sp^2 configuration, three of the four valence electrons are assigned to sp^2 hybridized orbitals. These orbitals are placed in a planar trigonal assembly, with 120° angles between them, and form strong σ bonds with the adjacent carbon atoms. As a result, the sp^2 carbon atoms form hexagonal rings, which are arranged in planar honeycomb networks. The fourth valence electron is assigned to the *p* orbital, which lies perpendicular to the sp^2 orbitals, and forms weak π bonds. While σ electrons exists only between two neighboring atoms, the π electron is highly delocalized and shared between one or more atoms [59].

In the sp^3 configuration, all four valence electrons are placed in tetrahedrally oriented sp^3 orbitals. These electrons form only strong and directional σ bonds with their neighboring carbon atoms [59]. Figure 10 shows the atomic orbitals in all three configurations.

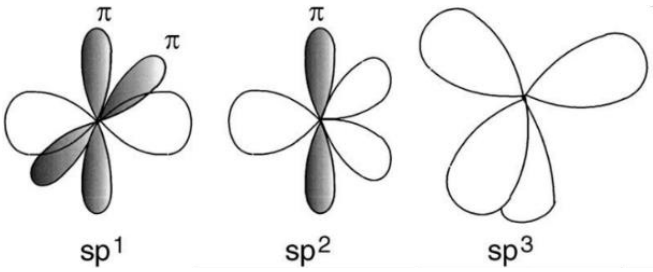

Figure 10: Different hybridizations of carbon atoms. The unshaded orbitals are hybridized, while the shaded orbitals are not [59].

In general, carbon materials can be divided into three groups, based on the hybridization of the carbon atoms; graphitic carbons, diamond-like carbons and amorphous carbons. Graphitic carbons are comprised predominantly of sp^2 hybridized atoms, while diamond-like carbons consist of only sp^3 hybridized atoms. Amorphous carbons (a-C) and tetrahedral amorphous carbons (ta-C) contain of a mixture of both sp^2 and sp^3 hybridized atoms. The hybridization of carbon atoms is, however, not the only factor that defines a carbon material. Other key parameters include [60]:

- The ratio of sp^2 and sp^3 hybridized carbon atoms.
- The ordering and orientation of the sp^2 phase.
- The cross-sectional nanostructure of the material.
- The hydrogen content.

The composition of the various carbon materials can be displayed in a ternary phase diagram, as depicted in figure 11.

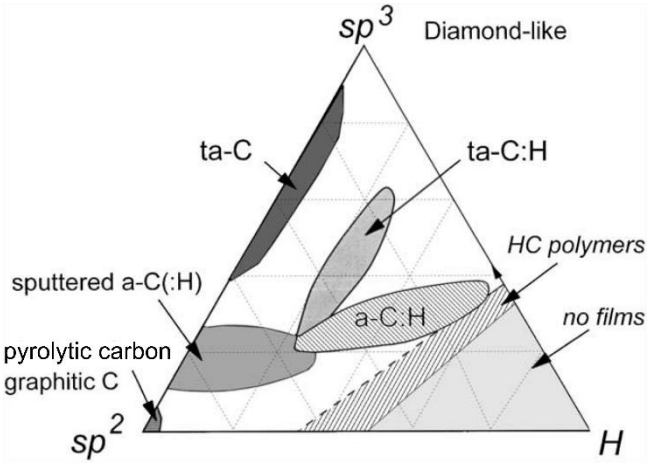

Figure 11: Ternary phase diagram of carbon films. The three corners correspond to diamond-like carbons (sp^3), graphitic carbons (sp^2) and hydrocarbons (H). Pyrolytic carbon can be found amongst graphitic carbons, meaning that its crystal structure is comprised predominantly of sp^2 hybridized atoms [59].

3.1 Properties of pyrolytic carbon

When discussing the properties of pyrolytic carbon, one must always account for the fact that the specific properties of the material depend upon the fabrication parameters, as presented above. Although the properties between different pyrolytic carbons may vary, some general conclusions can still be made in order to provide an outline on the material.

Pyrolytic carbon exhibits a very high chemical stability and extreme inertness, with an excellent resistance to strong acids and other corrosive agents. The material is highly biocompatible, allowing for its use in biological and biomedical applications. Pyrolytic carbon also possesses a wider electrochemical stability window over that of platinum and gold, making it an excellent electrode material for electrochemical sensors [3]. Its electrical resistivity typically ranges from 10 to 50 μΩm when pyrolyzed at 900 °C, and decreases further with increasing pyrolysis temperatures [17], [53].

Despite its excellent chemical stability, pyrolytic carbon does react with oxygen at elevated temperatures, allowing for the material to undergo oxygen plasma etching [7]. This process is commonly used to clean the surface of pyrolytic carbons, thereby improving their surface properties [6], [22]. Oxygen plasma etching can also be used to fabricate carbon microstructures from pyrolytic carbon films [61], [62]. However, this is not common practice due to the slow etching rates.

Pyrolytic carbon exhibits a very high isotropy of its structural and physical properties. Its density ranges between 1.4 and 1.5 g/cm^3 [63], which is lower than that of graphite (2.3 g/cm^3), indicating a high degree of porosity within the materials structure [7]. X-ray diffraction (XRD) studies have confirmed the presence of very small closed pores, approximately 5 nm in diameter, that form due to the materials disordered nature [64]. The presence of closed pores renders pyrolytic carbon impenetrable to most gasses and liquids, as well as highly resistant to crack propagation [57]. The high resistance to crack propagation along with the materials low coefficient of thermal expansion, 2.2 – 3.2·10^{-6} /K, make pyrolytic carbon thermally inert and highly resistant to thermal shock [7], [57]. The material possesses a Young's modulus between 10 and 40 GPa and a hardness between 3 and 6 GPa, making pyrolytic carbon a hard but brittle material [7], [54]. Pyrolytic carbon also experiences a very low surface roughness, with values typically below 1 nm [20], [22].

3.2 Crystal structure of pyrolytic carbon

The crystal structure of pyrolytic carbon has been the subject of numerous debates for more than half a century. Although several different models have been proposed in the past, a consensus on this matter has yet to be reached, as the high structural disorder of pyrolytic carbon creates numerous uncertainties on its underlying morphology [7].

In general, the crystal structure of pyrolytic carbon is comprised predominantly of sp^2 hybridized carbon atoms, which form highly curved graphitic planes [54]. The in-plane size of the graphitic crystallites (L_a) is typically around 6 nm, for pyrolytic carbons pyrolyzed at 900 °C, and increases in size with higher pyrolysis temperatures [54], [65]. The small size of the crystallites give pyrolytic carbon a structure closely resembling that of paracrystalline materials [66]. Pyrolytic carbon also consists of small amount of sp^3 hybridized atoms, which form amorphous zones between the graphitic crystallites [54], [66]. The material will typically consist of approximately 5 % of sp^3 hybridized atoms when pyrolyzed at 600 °C and less than 1 % when pyrolyzed at 1000 °C [54].

One of the first and most widely accepted models of pyrolytic carbon was proposed in 1971 by Jenkins and Kawamura [67]. In their model, Jenkins and Kawamura suggest that the structure of pyrolytic carbon is comprised of aromatic carbon molecules. The carbon molecules are connected to each other through highly strained covalent bonds, thus forming highly entangled and wrinkled graphitic carbon sheets. At higher pyrolysis temperatures, the graphitic sheets begin to stack and form graphitic carbon ribbons, as presented in figure 12.

This model is based on the assumption that the molecular orientation of the polymeric precursor is partially preserved after carbonization thus, the structure of pyrolytic carbon bears some resemblance to that of a polymer. The size of the entangled ribbons and the number of stacked graphitic sheets increases with higher pyrolysis temperature. However, even at temperatures above 3000 °C the structure does not fully transform into crystalline graphite but rather preserves its nanocrystalline nature, due to chain morphology restrictions in the structure of the polymer precursor as well as spatial constraints [67].

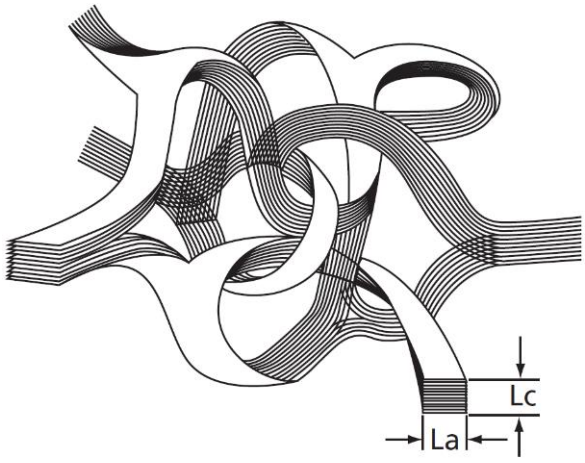

Figure 12: The structural model of pyrolytic carbon proposed by Jenkins and Kawamura. L_a and L_c indicate the intraplanar and interplanar graphitic crystallite size, respectively [67].

More recently, a new model on the crystal structure of pyrolytic carbon was proposed by Harris [68]. In his model, Harris suggests that the structure of pyrolytic carbon is comprised of highly curved sp^2 hybridized graphene-like layers, which form broken or imperfect fullerene-like structures. Most of these structures enclose pores with sizes ranging from 1 to 10 nm. The curvature of the graphitic planes is attributed to the presence of pentagonal and heptagonal carbon rings, which were observed directly with the use of transmission electron microscopy (TEM). At higher pyrolysis temperatures, the pentagon carbon rings begin to transform into hexagonal rings, thereby leading to the straightening of the graphitic layers. Higher pyrolysis temperatures also lead to an increase in the size and number of stacked graphitic layers, with two to four layers in each stack.

Jurkiewicz *et al.* [54] later further expanded on the work of Harris by suggesting that the structure of the graphitic layers resembles that of fragmented carbon nanotubes, fullerenes, and nanoonions. Figure 13 shows the model of pyrolytic carbon proposed by Harris, for both low-temperature and high-temperature pyrolytic carbons, along with the TEM images upon which the models are based.

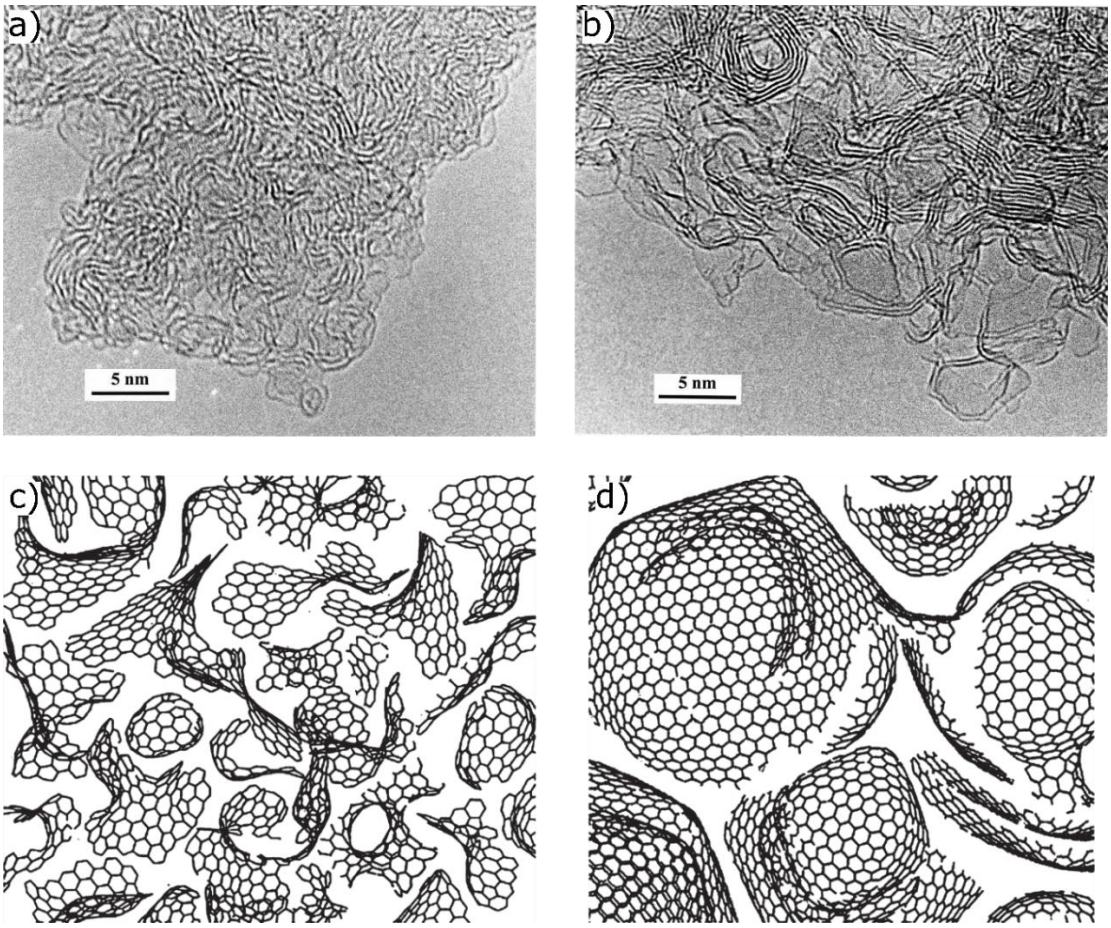

Figure 13: TEM images of pyrolytic carbon pyrolyzed at (a) 1000 °C and (b) 3000 °C. These TEM images served as a basis for the model on (c) low-temperature pyrolytic carbons and (d) high-temperature pyrolytic carbons, proposed by Harris [68].

The structure of pyrolytic carbon is often analyzed in terms of its crystallinity and crystallite size, the sp^2:sp^3 ratio of hybridized carbon atoms as well as the degree to which the precursor is carbonized [14], [54], [57]. The crystallinity and crystallite size are typically determined with the use of Raman spectroscopy, TEM or XRD. On the other hand, studies on the sp^2:sp^3 ratio and degree of carbonization require the use of electron energy loss spectroscopy (EELS), UV Raman spectroscopy or X-ray photoelectron spectroscopy (XPS) [14], [54].

3.2.1 Raman spectroscopy

Raman spectroscopy is a non-destructive technique commonly used for the structural characterization of carbon materials. Its high popularity comes courtesy of its simple use, the amount of information that the technique provides and the requirement of a very small sample size. Raman spectroscopy is often used to analyze the bonding type between carbon atoms, the degree of crystallinity, the size of the carbon crystallites, as well as the presence of defects [60], [69]–[72]. The technique can also provide information on the curling and imposed strain on the graphitic carbon sheets [73], [74], the number of stacked graphitic layers [22], the presence of hydrogen and nitrogen in the material [60], intercalation of lithium ions [2], and can also be used to obtain information on the sp^2:sp^3 ratio of hybridized carbon atoms [60], [69], [70].

The Raman spectrum of pyrolytic carbons shows three distinctive peaks; the G, D and 2D peaks. The graphitic or "G" peak is located at approximately 1580 cm^{-1} and stems from an E_{2g} symmetry mode associated with in-plane stretching of sp^2 carbon atom pairs, as presented in figure 14 (c). The E_{2g} symmetry mode does not depend on the arrangement of carbon atoms in hexagonal rings but can instead occur on all sites where sp^2 hybridized carbon atoms are present [69], [71].

The disorder or "D" peak is located at approximately 1360 cm^{-1} and is associated with the breathing motion of hexagonal carbon rings in an A_{1g} symmetry mode, as presented in figure 14 (c). The A_{1g} mode is forbidden in perfectly crystalline graphite and becomes active only in the presence of a disordered lattice (e. g. edges, vacancies, dopants). This means that the intensity of the D peak is proportional the level of disorder within the graphitic planes [22], [60], [69].

The 2D peak is located at approximately 2700 cm^{-1} and is an overtone of the D peak. However, unlike the D peak, the 2D peak does not require the presence of a defect for its activation. Its intensity is related to the spatial uniformity in either the graphitic plane or the interlayer spacing [22].

Figure 14 (a) shows a comparison between the Raman spectrums of pyrolytic carbon and highly crystalline graphitic powder. The Raman spectrum of pyrolytic carbon shows a much more intensive D peak than the graphitic powder, indicating a highly disordered structure. Similarly, the G peak is much broader for pyrolytic carbon, indicating a smaller crystallite size. Furthermore, the very broad 2D peak implies a lack of special uniformly of the pyrolytic carbon structure [22].

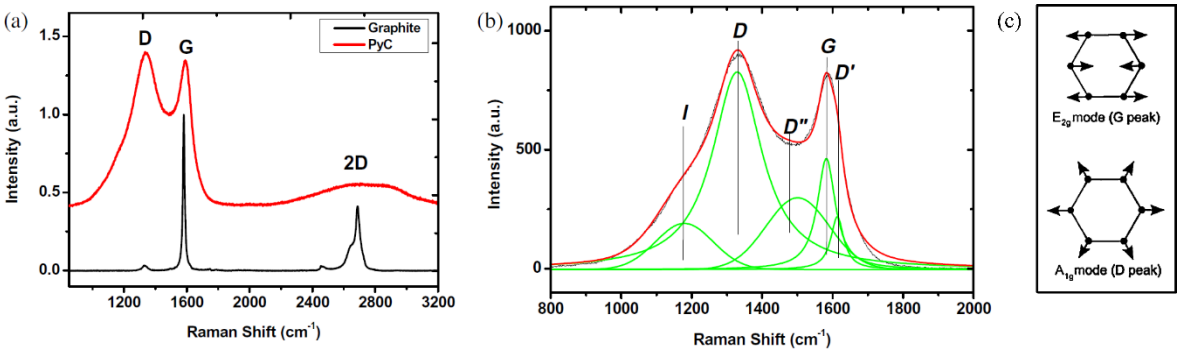

Figure 14: (a) The Raman spectrum of pyrolytic carbon (PyC) in comparison to that of highly ordered graphitic powder. (b) Deconvoluted Raman spectrum of pyrolytic carbon showing the location and intensity of all first-order peaks [22]. *(c) E_{2g} and A_{1g} symmetry modes associated with the G and D peak, respectively* [69].

While typically only the G, D and 2D bands will be directly visible in the Raman spectrum of pyrolytic carbon, several other minor bands, associated with nanocrystalline graphitic carbons, can be fitted into the overall shape of the Raman shift curve. These peaks include the D', D" and I peak [22], [54]. A fitting of all first-order peaks into the Raman curve can be seen in figure 14 (b). A short description on the origin and approximate positions of the D', D" and I peak can be found in table 1.

Table 1: Origin and position of minor first-order peaks in the Raman spectrum of pyrolytic carbon [22].

Peak	Position [cm^{-1}]	Description
D'	~1620	Occurs in defective graphitic systems and manifests itself as a shoulder of the G band.
D''	~1500	Related to the presence of amorphous carbon.
I	~1180	Linked with the disorder of the graphitic lattice, sp^2-sp^3 bonds and the presence of polyenes.

Analyzing the Raman spectrum of graphitic carbons

The Raman spectrum of graphitic carbons is typically analyzed in terms of the intensity, position as well as the width of the G and D peaks. In order to obtain such information, first the peaks need to be fitted with appropriate functions. For highly disordered graphite, fitting is typically done with the use of Lorentzian curves. The intensities of the G ($I_{(G)}$) and D ($I_{(D)}$) peaks are defined as the integrated areas underneath the fitted curve for the respected peaks. On the other hand, the width of the peaks are represented by the full width at half maximum (FWHM) of the fitted curves [69].

The Raman spectrum of carbon materials can be analyzed with the use of a three-stage model of increasing disorder, developed by Ferrari and Robertson [69]. Represented in figure 15, the three-stage model describes the changes in the $I_{(D)}/I_{(G)}$ ratio and position of the G peak as the structure of carbon materials moves from a highly crystalline graphite to a predominantly sp^3 bonded tetrahedral amorphous carbon. This is known as the amorphization trajectory which consists of three stages [60]:

1) Graphite → nanocrystalline graphite
2) Nanocrystalline graphite → amorphous carbon
3) Amorphous carbon → tetrahedral amorphous carbon

Stage 1 corresponds to a progressive decrease in crystallinity from a highly ordered graphitic carbon to nanocrystalline graphite. Starting from a perfectly crystalline graphite, the Raman spectrum consists only of a sharp G peak as there is no disorder within the material. Hence, the $I_{(D)}/I_{(G)}$ ratio will be 0. As the crystal structure begins to break down into smaller crystallites, the $I_{(D)}$ increases due an increasing disorder. This, in turn, leads to an increase in the $I_{(D)}/I_{(G)}$ ratio, depending on the level of disorder. At the same time, the position of the G peak moves towards higher frequencies due to the appearance of the D' peak, which manifests itself as a shoulder of the G band. The end of stage 1 coincides with a highly disordered nanocrystalline graphite [60], [69].

Stage 2 corresponds to an increase in the topological disorder of the graphitic layers. By further introducing defects into the structure of nanocrystalline graphite and reducing the crystallite size (L_a) below 2 nm, the number of hexagonal aromatic rings begins to decline. Since the D peak relies on the arrangement of sp^2 atoms in rings, the $I_{(D)}$ decreases. On the other hand, the G peak retains its intensity as its presence is related only to the bond stretching of sp^2 pairs. Thus, the $I_{(D)}/I_{(G)}$ ratio decreases with increasing amorphization. At the same time, the position of the G peak moves towards lower frequencies due to the weaker

sp^2 bonds. The end of stage 2 coincides with a completely disordered amorphous carbon consisting of distorted sp^2-bonded rings and up to 20 % of sp^3 hybridized amorphous carbon zones [60], [69].

Stage 3 corresponds to the progressive conversion of sp^2 sites to sp^3 sites and the change of the sp^2 configuration from rings to chains. At this point, the position of the G peak shifts towards higher frequencies due to the confinement of π electrons in shorter olefinic chains. Simultaneously, the $I_{(D)}/I_{(G)}$ ratio decreases to 0 as all sp^2 rings are replaced with sp^2 chains. The end of stage 3 coincides with a completely disordered tetrahedral amorphous carbon, consisting of up to 85 % of sp^3 bonded carbon atoms [60], [69].

For pyrolytic carbons, the three-stage model can be used to determine how various changes in the fabrication process effect the crystal structure of the material.

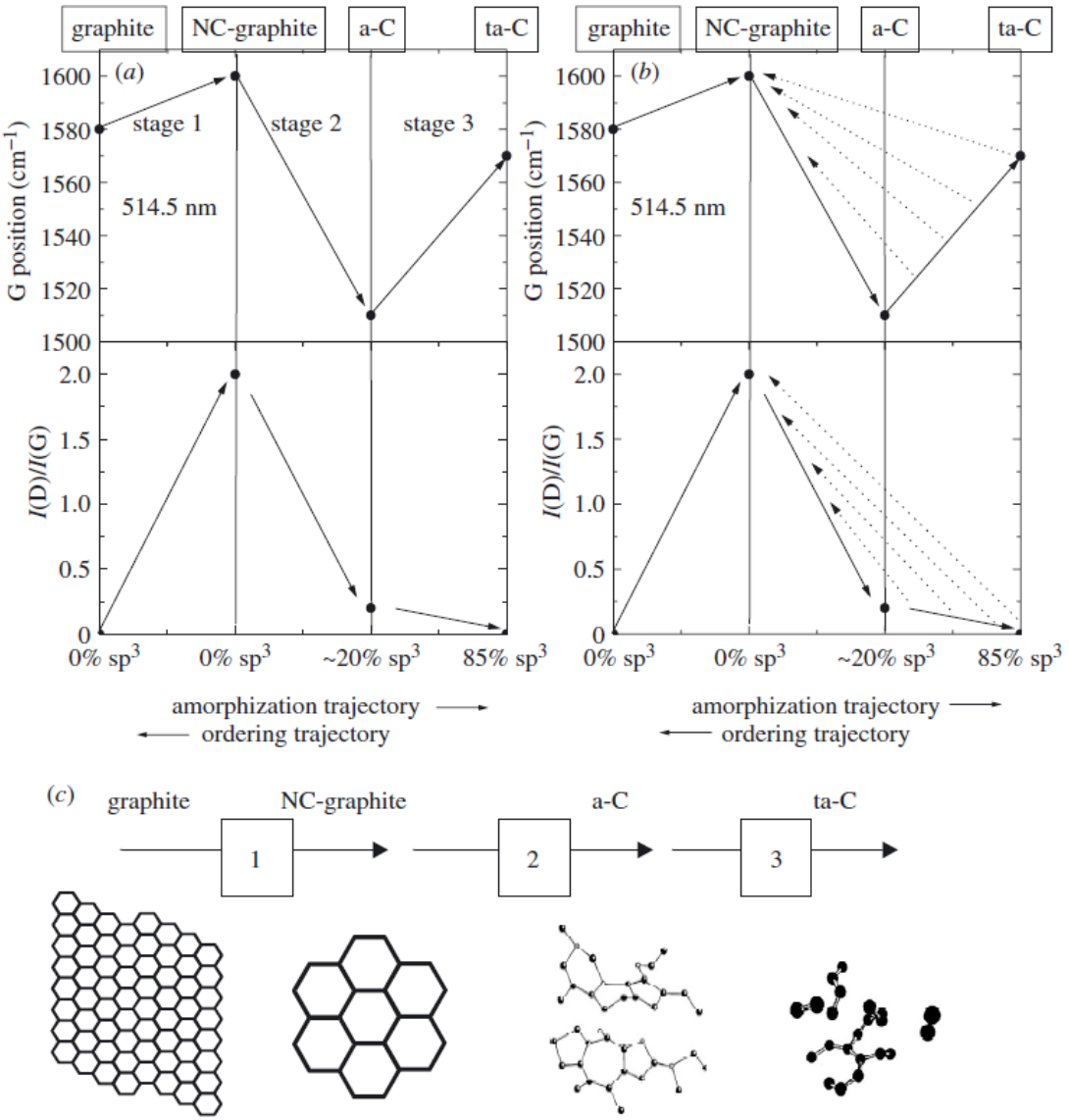

Figure 15: The three-stage model of increasing disorder proposed by Ferrari and Robertson. (a) The model relates the $I_{(D)}/I_{(G)}$ ratio and the position of the G peak to the crystal structure of the material. (b) The dotted left-pointing arrows mark the non-uniqueness region in the ordering trajectory, where a carbon material transitions from ta-C to crystalline graphitic carbon. It should also be noted that the exact peak positions in the three-stage model are not definitive but rather depend on the excitation laser wavelength of the Raman spectrometer. (c) The structure of the various carbon material encountered within the three-stage model [60].

Since $I_{(D)}$ is related to the presence of disorder in graphitic carbon materials, the $I_{(D)}/I_{(G)}$ ratio can also be used to determine the in-plane crystallite size, L_a. Equations 5 and 6 show how L_a can be approximated based on either the excitation laser energy, E_l (in eV), or the excitation laser wavelength of the Raman spectrometer, λ_l (in nm) [75];

$$L_a = \frac{560}{E_l^4}\left(\frac{I_{(D)}}{I_{(G)}}\right)^{-1} \tag{5}$$

$$L_a = (2.4 \cdot 10^{-10})\lambda_l^4\left(\frac{I_{(D)}}{I_{(G)}}\right)^{-1} \tag{6}$$

3.3 Other carbon materials

Due to their highly complex microstructure and wide range of properties, pyrolytic carbons are often analyzed in comparison to other carbon materials. Since C-MEMS are predominantly used as microelectrodes in electrochemical sensors, one particular property of interest is the materials electrical resistivity. The electrical resistivity of a material is a key parameters that defines the heterogeneous electron transfer rate between the electrode and electroactive species, whereby a lower resistivity leads to a higher electron transfer rate [2].

3.3.1 Graphitic carbons

Graphitic carbons are comprised of sp^2 hybridized atoms. The strong covalent σ bonds give graphitic carbon sheets their high mechanical strength, while the highly delocalized π electrons provides them with a good electrical conductivity [76]. Based on how the graphitic sheets stack and bend, several different types of graphitic carbons can be formed. Figure 16 shows the microstructure of some of the most common graphitic carbon allotropes, including graphite, graphene, carbon nanotubes (CNT) and fullerenes.

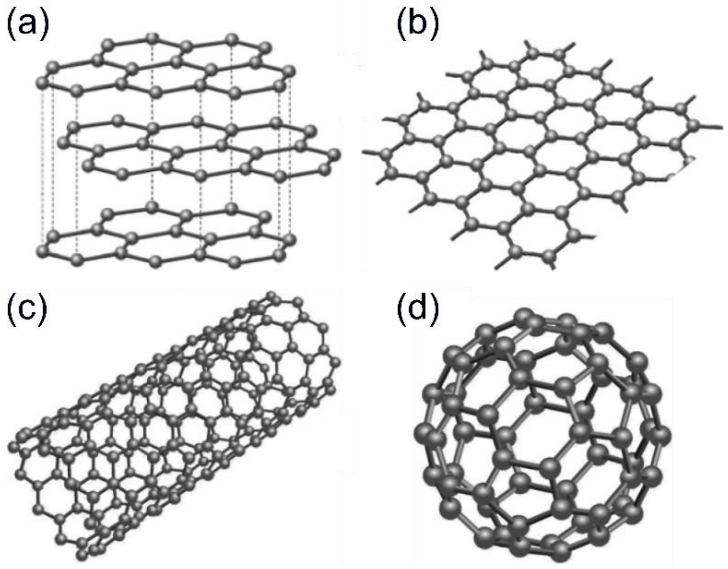

Figure 16: Microstructures of some of the most common graphitic carbon allotropes; (a) graphite, (b) graphene, (c) carbon nanotubes and (d) fullerenes [77].

Graphite

One of the most commonly known graphitic carbon materials in graphite. Graphite consists of several stacked graphitic sheets that are held together by weak van der Waals bonds, as presented in figure 16 (a). Due to the different bond types between the carbon atoms, graphite exhibits anisotropic properties whether they are measured within the basal plane or in-between the basal planes. For example, the graphite exhibits a very good electrical and thermal conductivity along the basal plane but very poor conductivity between the planes. This is caused by the π electrons which can easily move within the graphitic planes but not between the planes [2], [76]. Typical electrical resistivity values for highly crystalline graphite range from $4 \cdot 10^{-7}$ Ωm across the plane to $1.7 \cdot 10^{-3}$ Ωm between the planes [2].

Figure 17 shows the Raman spectrums of perfectly crystalline graphite and commercially available graphite. The perfectly crystalline graphite shows only a G peak as there is no disorder in the material. One the other hand, the commercially available graphite shows a small D peak which indicates the presence of disorder within the crystal structure.

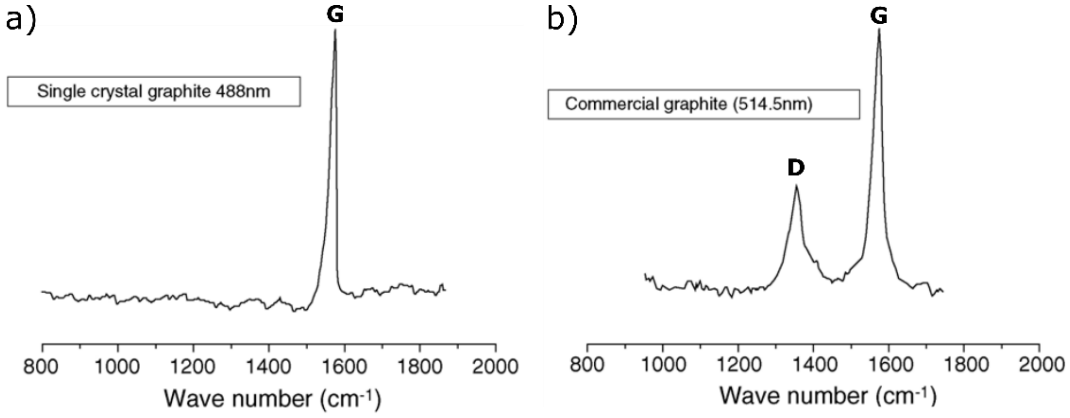

Figure 17: The Raman spectrum of (a) perfectly crystalline graphite and (b) commercially available graphite [71].

Graphene

Graphene consists of a single planar graphitic sheet, as presented in figure 16 (b). Compared to graphite, graphene shows better electrical properties both across and through the basal plane, due to the absence of van der Waals bonds [2].

Carbon nanotubes

Carbon nanotubes (CNT) consist of rolled-up graphitic sheets that form hollow tubes, as presented in figure 16 (c). The ends of the tubes can either be left open or can be closed with a fullerene-like structure [2]. The electrical properties of CNT depend on their chirality (the angle at which the graphene sheets are rolled) and can act as either metals or semiconductors. The reason for this is that by curving the graphene sheets, the position of the sp^2 orbitals becomes distorted, thereby causing them to be shaped more like sp^3 orbitals. This essentially means that the electrical properties of CNT is dictated by their radius [2].

3.3.2 Diamond

Diamond and diamond-like carbons consists of only sp^3 hybridized carbon atoms. The strong and highly localized σ bonds between the carbon atoms give diamond its extremely high hardness and very low electrical conductivity, thereby making diamond an electrical insulator [76]. The electrical conductivity can, however, be increased by doping the material with boron or nitrogen, which changes the electronic properties of diamond to that of a semiconductor [2]. Figure 18 shows the microstructure of diamond.

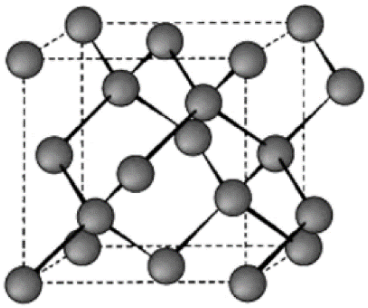

Figure 18: Microstructure of diamond [77].

The Raman spectrum of diamond shows a single peak located at 1332 cm^{-1}. This peak is often referred to as the ″diamond″ peak and stems from a T_{2g} symmetry motion of sp^3 hybridized carbon atoms. The degree of disorder within the material can be evaluated based on the width of the peak [71]. Perfectly crystalline diamond experiences a peak width of ~2 cm^{-1}, while microcrystalline diamond exhibits a peak width of ~10 cm^{-1} [2]. Diamond also shows a second peak located at ~1060 cm^{-1}, labeled the "T" peak. However, this peak is only visible with the use of UV Raman spectroscopy [60]. Figure 19 shows the Raman spectrum of perfectly crystalline diamond.

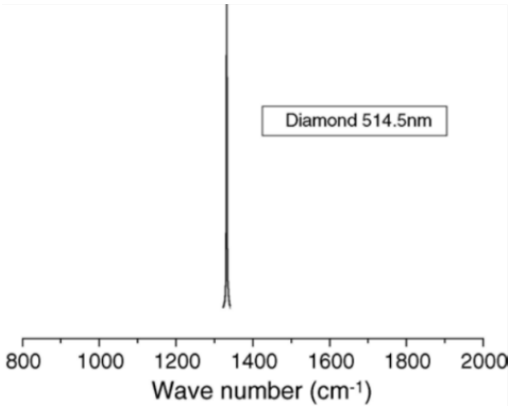

Figure 19: The Raman spectrum of perfectly crystalline diamond [71].

3.3.3 Amorphous carbons

Amorphous and tetrahedral amorphous carbons contain an unstructured mixture of both sp^2 and sp^3 hybridized atoms. a-C consists predominantly of sp^2 sites, while ta-C are dominated by sp^3 sites. These materials do not show any long-range order that can be find in diamond or graphite although, the bonds can sometimes intermix and exhibit an extended order on a nano-scale [71].

The exact distinction between nanocrystalline graphitic carbon and amorphous carbon is often times unclear as the small crystallite size of nanocrystalline carbon can be presented as a borderline case of amorphous carbon. According to the three-stage model [69], nanocrystalline graphite begins to transition into amorphous carbon when the crystallite size falls below 2 nm. Amorphous carbons also typically contain a higher amount of sp^3 sites than nanocrystalline graphitic carbons [59].

When analyzing the structure of amorphous carbons, one property that is of particular interest is the ratio of sp^2 and sp^3 hybridized atoms. The Raman spectrum of amorphous carbons is dominated by features indicative to that of graphitic carbons, as the π bonds are far more polarizable than the σ bonds. As a result, visible Raman spectroscopy is 50 to 250 times more sensitive to that of sp^2 than sp^3 sites and the diamond peak will only be visible as the sp^3 content exceeds 80 % of the materials composition. This means that the sp^2:sp^3 ratio cannot be directly analyzed with the use of visible Raman spectroscopy. On the other hand, UV Raman spectroscopy is capable of exciting the σ electrons to the point where sp^3 sites can be observed even at lower concentrations. Alternatively, the sp^2:sp^3 ratio can be determined with the use of EELS [60].

Figure 20 shows the Raman spectrums of a-C and ta-C. The Raman spectrum of a-C shows a significant overlap and high distortion of the G and D peaks due to the amorphous nature of the material. In the Raman spectrum of ta-C, the peaks can no longer be distinguished from one another due to the severely reduced number of sp^2 rings.

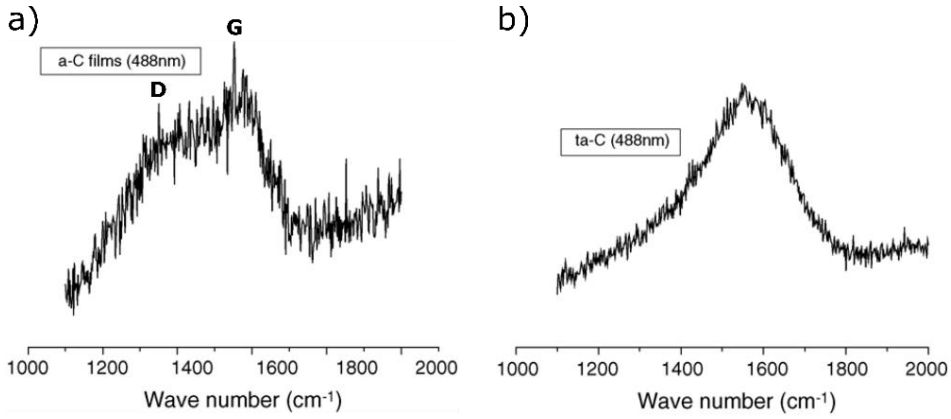

Figure 20: The Raman spectrum of (a) amorphous and (b) tetrahedral amorphous carbon [71].

4. SU-8

SU-8 is an epoxy-based negative photoresist developed by IBM in the late 1980's. Since its first introduction, SU-8 has become one of the leading materials used for the fabrication of highly complex 3D microstructures. The high popularity of SU-8 comes courtesy of its excellent mechanical, chemical and optical properties, which allow for the deposition and patterning of very thick layers with high resolutions [25]. Patterning of SU-8 is most commonly performed with UV light, although other exposure sources, including X-rays, laser beams, electron beams and proton beams, can also be used [25], [26]. In this chapter, we will be primarily focusing on the processing of SU-8 with the use of UV photolithography.

4.1 Properties of SU-8

SU-8 is comprised of a Bisphenol A Novolak epoxy resin (EPON SU-8) dissolved in an organic solvent, either propylene glycol methyl ether acetate (PGMEA), cyclopentanone or *gamma*-butyrolactone (GBL), and up to 10 wt. % of triarylsulfonium hexafluoroantimonate salt, which acts as the photoinitiator. The SU-8 resin is a highly branched epoxy derivative that consists of Bisphenol A Novolak glycidyl ether monomers, as seen in figure 21 [25].

Upon exposure, the photoinitiator starts a sequence of chemical reactions which lead to the cross-linking of the SU-8 monomers. First, the triarylsulfonium hexafluoroantimonate salt decomposes and forms small concentrations of hexafluoroantimonic acid. The acid activates the SU-8 molecules by protonating the epoxides on the edge of the monomers and opening them up. During this process, the acid is not consumed but rather acts as a catalyst meaning that one acidic molecule can open up several epoxy rings. The protonated epoxides react with other neutral epoxides in a series of cross-linking reactions under the application of heat, resulting in a highly polymerized matrix [25].

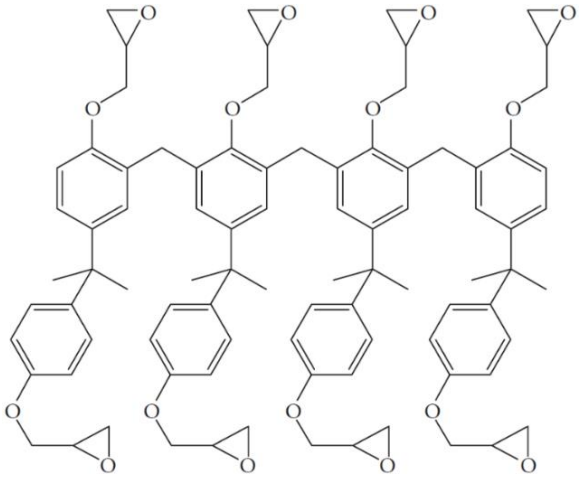

Figure 21: Molecular structure of the SU-8 resin. The name is derived from the 8 epoxy groups at the edge of the molecule [25].

The low molecular weight of the SU-8 monomers (~7000 ± 1000 Da) translates into a very high solubility of the resin in the solvent. As a result, highly concentrated formulations of the resists can be prepared which allow for the deposition of very thick layers. In fact, SU-8 films with thicknesses of up to 500 µm can be deposited in a single spin coating process and up to 3 mm in a multi-spin coating process [26]. The low molecular weight of the resin also gives SU-8 its high contrast, allowing for the fabrication of very fine microstructures. A high epoxy content makes SU-8 highly sensitive to UV light and promotes a strong adhesion of the resist to a variety of different substrates [25], [26]. Furthermore, SU-8's high optical transparency allows for exposure depths of up to 2 mm and the fabrication of microstructures with very high resolutions (< 1 µm) [25].

The highly cross-linked matrix provides SU-8 with a good chemical stability, allowing the resist to withstand various harsh chemicals, including nitric acid and acetone. SU-8 is also highly biocompatible, leading to its use in numerous biological and biomedical applications [78]. Furthermore, the high level of cross-linking gives SU-8 a high thermal stability, with a glass transition temperature (T_g) of over 200 °C and a decomposition temperature (T_d) of approximately 380 °C. This allows SU-8 to be used in applications where high temperatures are required [25].

The Young's modulus (E) of fully cross-linked SU-8 ranges from 4 to 5 GPa, which provides HAR and suspended SU-8 microstructures, with the required structural stability [26]. Today, HAR SU-8 microstructures with a 10:1 ratio can easily be fabricated with a very high consistency, while Yang and Wang [79] were able to fabricate SU-8 structures with an aspect ratio of 190:1. Figure 22 shows SU-8 HAR microstructures developed by Yang and Wang.

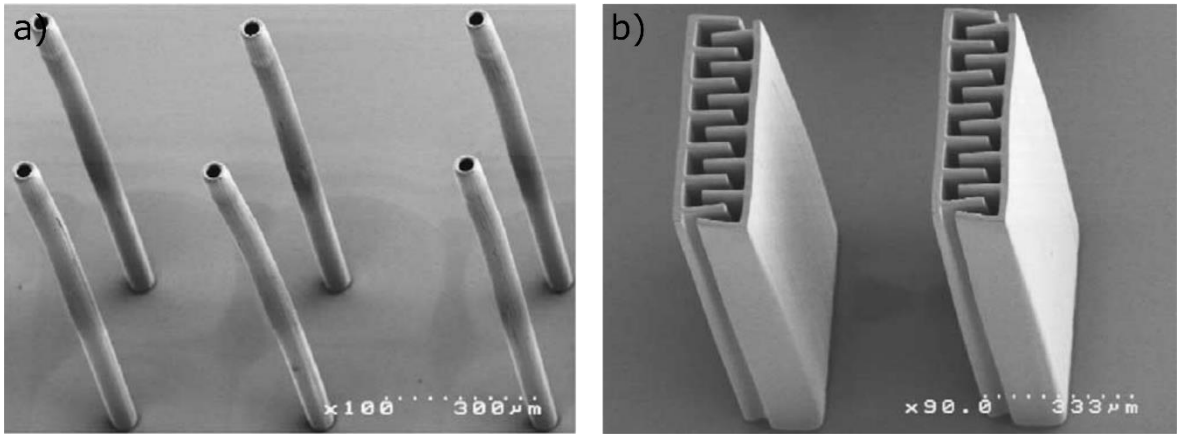

Figure 22: SEM images of (a) HAR SU-8 microcylinders with a height of 1150 µm and diameter of 55 µm. (b) HAR SU-8 IDA microstructures with a height of 1150 µm and width of 20 µm [79].

Today, there are several different commercially available SU-8 formulations with varying viscosities and solvents. The specific SU-8 formulation is selected based upon the desired film thickness, as well as the substrate material [26]. Table 2 shows the properties of some of the most commonly used SU-8 photoresists in C-MEMS fabrication.

Table 2: Properties of different SU-8 formulations and the deposition thickness range [25], [26].

Type	Solvent	Viscosity [cSt]	Solid [%]	Density [g/ml]	Thickness [µm]
SU-8 25	GBL	2 500	63	1.200	15 – 40
SU-8 50	GBL	12 250	69	1.219	40 – 100
SU-8 100	GBL	51 500	73.5	1.233	100 – 250
SU-8 2010	Cyclopentanone	380	58	1.187	13 – 15
SU-8 2050	Cyclopentanone	12 900	71.65	1.233	50 – 165
SU-8 2100	Cyclopentanone	45 000	75	1.237	100 – 260

4.2 Photolithography of SU-8

Photolithography of SU-8 involves a number of sequential processing steps, including; substrate preparation, photoresist deposition, soft baking, exposure, post-exposure baking, development and an optional hard baking step. Each of these steps has an effect on the final properties of the SU-8 microstructures. Thereby, every processing parameter must be carefully optimized in order to obtain microstructures with a high structural stability and high level of dimensional accuracies [25].

4.2.1 Substrate preparation

Photolithography of SU-8 is typically performed on silicon wafers. Prior to the deposition of the resist, the substrate must be sufficiently prepared in order to ensure a homogeneous and stable coating with good adhesion to the substrate [26].

The most common preparation step involves cleaning of the wafers, so that any impurities, such as native surface oxides, solvent stains or dust particles, are removed from the substrates surface. Cleaning of silicon wafers is typically performed by means of wet etching in hydrofluoric acid (HF) or in a Piranha solution (mixture of sulfuric acid and hydrogen peroxide). Hydrofluoric acid readily reacts with SiO_2 and is thus used to remove any native oxides that may have formed on the wafers surface. On the other hand, the Piranha solution is used to remove any organic materials from the substrate, such as other photoresists [25].

Other materials commonly used in microfabrication can also be used as a substrate for SU-8 photolithography. However, in order to ensure a good adhesion of the photoresist to the substrate, a good wetting of the substrate by SU-8 is crucial. SU-8 is hydrophobic and has thus difficulties wetting hydrophilic surfaces [26]. Studies have shown that SU-8 exhibits a good adhesion to Si, SiO_2, Al, Ti and Au substrates, but poor adhesion to glass substrates [25], [80]. Wetting of the substrate can be improved by applying a primer coating to the substrate surface. Primers are organic molecules which are either adsorbed or react with the substrate. This creates a thin organic layer with a low surface energy on the substrates surface, thereby allowing for a better wetting of the substrate by SU-8. Common commercial primers include hexamethyldisilazane (HMDS) and methacryloxypropyltrimethoxysilane (MPTS) [26].

4.2.2 Spin coating

The deposition of photoresists is most commonly done through spin coating. Spin coating operates on the principle that a photoresist is uniformly spread over the surface of a rotating substrate due to centrifugal forces which act upon the resist. This allows for the deposition of very thick layers (up to hundreds of microns) within the matter of minutes. The final thickness of the photoresist depends on the spinning speed, time and acceleration, as well as the viscosity of the resist. Higher speeds and longer spinning times will result in thinner and more homogeneous coatings [25]. Figure 23 shows the film thickness for SU-8 50 and SU-8 100 as a function of the spinning speed.

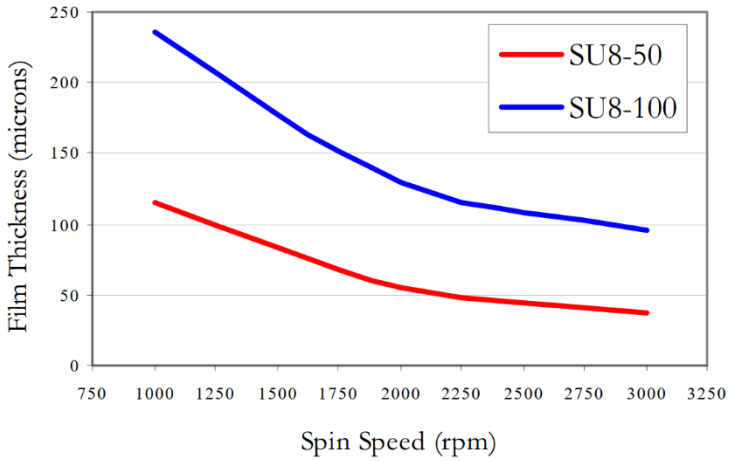

Figure 23: Film thickness as a function of the spinning speed for SU-8 50 and SU-8 100. The greater thickness of the SU-8 100 resist is due to its higher viscosity [81].

The spin coating process is divided into three consecutive steps; dispensing, spreading and coating. First, the wafer is placed on a vacuum actuated chuck, which holds the substrate in place during spinning. Next the photoresist is dispensed in the center of the substrate. It is important that an appropriate amount of photoresist be dispensed as too much photoresist can lead to planarization defects and flatness errors of the film, while too little photoresist can result in an insufficient coating of the substrate [25]. Dispensing is followed by spreading, where the wafer is rotated with a speed of approximately 500 rpm for 5 to 10 seconds, in order to spread the photoresist over the substrate surface [81]. After spreading, the substrate is immediately accelerated to its final rotation speed. This step reduces the thickness of the photoresist to its final value and completely coats the substrate. Typical parameters used in the coating process involve a rotation speed between 1000 and 4000 rpm, an acceleration between 200 and 500 rpm/s and spinning times between a few seconds up to several minutes. Once the wafer has stopped spinning it can be left on the spinner for a short period of time in order to allow the resist to relax and reflow. Relaxation and reflow of the resist eliminates any planarization defects, air bubbles and stress that may have formed in the material during the coating process, thereby enhancing its adhesion to the substrate [25].

The spin coating process is designed to render homogeneous coatings with planar surfaces. However, the risk of planarization defects and flatness errors becomes greater as the viscosity of the resist (and therefore the coating thickness) increases. Planarization defects hinder the conformal contact between the photomask and resist during exposure, thereby

causing the diffraction of light off the photomask patterns and a non-uniform exposure of the resist. This can lead to lower resolutions, negative sloped sidewalls and T-topping of the patterned microstructures [25], [26].

A common planarization defects is the buildup of photoresist on the edges of the substrate, also known as an edge bead. For photoresists with lower viscosities, the edge bead can be removed by allowing the resist to relax and reflow. On the other hand, photoresists with higher viscosities cannot reflow as easily so, the edge bead is removed by spraying the edges of a slowly spinning wafer with either acetone, GBL or other commercially available edge bead removers [25].

4.2.3 Soft baking

Deposition is followed by a soft baking step, where the photoresist is heated up in an effort to evaporate the solvent. Evaporation of the solvent restricts the flow of the resist and enhances its adhesion to the substrate. On the other hand, removal of the solvent also creates high levels of intrinsic stress which can lead to reduced mechanical stability of the resist, the formation of cracks and even a complete delamination of the resist from the substrate [26]. In fact, studies have shown that soft baking is the largest contributor to the formation of stress in the resist [82]. So, in order to minimize the formation of stress, the heating steps must be carefully optimized.

Soft baking of SU-8 is performed at temperatures between 65 and 100 °C (typically at 95 °C), with baking times ranging from minutes to hours [25]. Although the main purpose of soft baking is to evaporate the solvent, a sufficient amount of residual solvent should remain in the resist after baking. The residual solvent increases the sensitivity of SU-8 and enhances the cross-linking process during exposure, as well as allows for a better relaxation of the polymer matrix during subsequent processing steps, thereby reducing the formation of residual stress and improving the mechanical stability of the photoresist. However, reduced baking temperatures and times can leave behind an excess amount of residual solvent which can cause the formation of bubbles and residual stress during post-exposure baking, reduce the mechanical stability of the SU-8 microstructures, as well as lower the contrast of the resist. On the other hand, elevated or prolonged baking can reduce the hardness of SU-8, induce the formation of cracks and can even lead to the thermal cross-linking of the resist [25], [26].

Soft baking can be performed either on a hotplate or in a convection oven. Convection ovens work by heating the resist uniformly from all sides. Often times, this will cause the solvent to evaporate from the upper layers of the resist first, thereby resulting in the formation of an impenetrable layer which restricts the evaporation of the remaining solvent. On the other hand, hot plates work by heating the resist from below by means of conductive heating. This causes the formation of a temperature gradient which allows for a more uniform evaporation of the resist and prevents the formation of an impenetrable layer [3]. Figure 24 shows SEM images of the impenetrable layer caused by the soft baking of SU-8 in a convection oven.

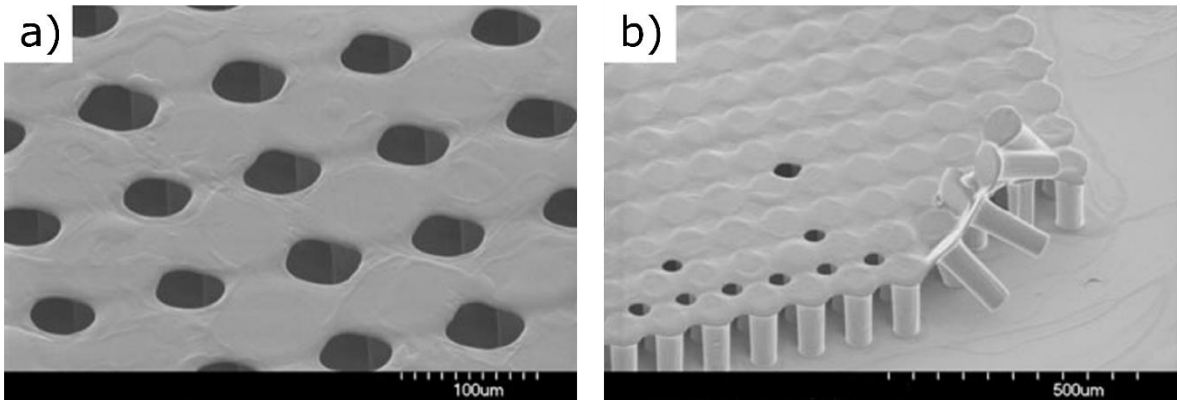

Figure 24: SEM images of an impenetrable layer formed during soft baking of SU-8 in a convection oven. The layer remains present even after the development of the resist [3].

4.2.4 Exposure

After soft baking, the photoresist is ready to be exposed. UV photolithography of SU-8 is typically performed with 365 nm (i-line) or 435 nm (g-line) wavelengths. The optimal exposure dose depends on the thickness of the resist and is required in order to fully polymerize the SU-8 throughout the whole depth of the exposed area [25]. The exposure energy, D (J/cm^2), can be varied by either changing the exposure time, t (s), or the intensity of the UV light, I (W/cm^2), and can be calculated by using the following equation:

$$D = I \cdot t \tag{7}$$

Underexposure of the resist lowers the concentration of the cross-linking acid, resulting in an insufficient polymerization of the SU-8 and its subsequent dissolution in the developer. On the other hand, overexposure of the resist generates an excess amount of cross-linking acid which can diffuse sideways and lead to the broadening of the exposed areas [25]. Figure 25 (a) shows the recommended exposure doses for SU-8 as a function of the resist thickness.

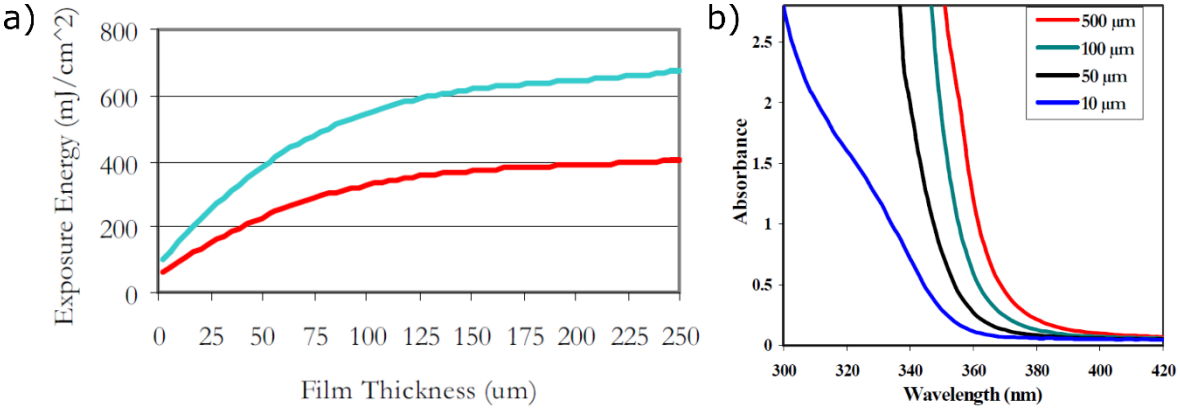

Figure 25: (a) Recommended exposure energies as a function of the resist thickness, for 365 nm wavelengths. The green line represents the maximum recommended exposure dose, while the red line represents the minimum recommended exposure dose. (b) Absorption of UV light as a function of the lights wavelength, for different SU-8 film thicknesses [81].

SU-8 shows a high absorption for UV light with wavelengths below 350 nm. Exposing the resist with these wavelengths leads to a significant drop in the light's intensity across the films thickness, thereby causing an overexposure of the resists upper layer and an underexposure of the resists bottom layer. As a result, the fabricated microstructures will obtain a "T" shaped profile. This effect is also known as T-topping [25]. Figure 25 (b) shows the absorption of UV light as a function of the light's wavelength.

T-topping can also occur due to gaps between the photomask and the photoresist. These can either be introduced intentionally, by exposing the resist in proximity mode, or can occur due to planarization defects, such as edge beads or a curved substrate. During exposure, the gaps between the photomask and the resist cause the diffraction of light from the edges of the photomask patterns, resulting in the exposure of a broader area at the top of the resist [26]. Figure 26 shows the T-topping of SU-8 microstructures due to the diffraction of light.

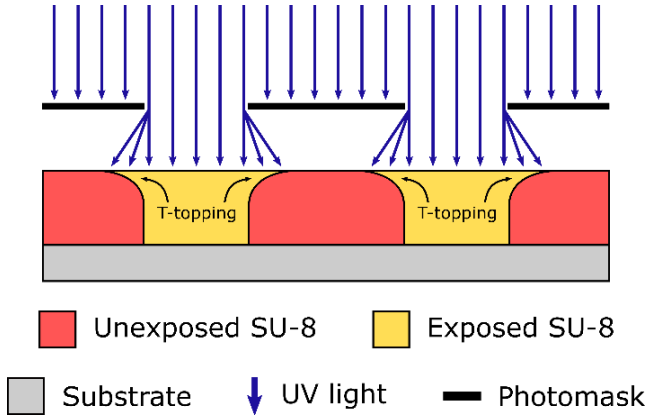

Figure 26: Schematic presentation on the T-topping of SU-8 microstructures due to the diffraction of light from the edges of the photomask patterns.

4.2.5 Post-exposure baking

Once the photoresist has been exposed, a post-exposure bake is required in order to finalize the polymerization process. The application of heat greatly increases the cross-linking rate, resulting in a fully polymerized matrix of the resist. Post-exposure baking is performed at temperatures between 60 and 100 °C (typically at 95 °C), and can be conducted either on a hotplate or in a convection oven [25].

In order to ensure a good stability of the fabricated microstructures, a precise control of the baking process is required. Excessive baking temperatures have shown to induce a significant amount of intrinsic stress in the resist, due to the mismatch in the coefficient of thermal expansion between the substrate and SU-8. High levels of stress can cause the formation of cracks, bending of the microstructures and can even cause delamination of the resist from the substrate. On the other hand, inadequate baking temperatures can lead to an insufficient polymerization of the exposed resist, resulting in its subsequent dissolution in the developer. Rapid heating and cooling rates should also be avoided as they can also induce significant amounts of stress in the resist. In order to minimize the formation of stress, longer baking times at lower temperatures and lower heating rates are recommended [25].

4.2.6 Development

Development of SU-8 is typically performed by immersing the resist in PGMEA, although other developers, such as ethyl lactate and diacetone alcohol, can also be used [81]. The development times mainly depend on the topography of the patterned microstructures. For example, features with narrow gaps, deep trenches or long channels can take many hours to develop due to the significantly reduced diffusion rate of the unpolymerized resist into the developer [25]. Prolonged development times should be avoided as they can induce swelling of the polymerized resist and even delamination of the microstructures from the substrate. The development times can be reduced by either increasing the temperature of the developer or by agitation (e. g. stirring). Stirring of the developer increases the diffusion rate of the unexposed resist which, in turn, lowers the development times. However, excessive stirring can also cause the SU-8 microstructures to deflect in the pressure gradients of the developer, leading to pattern deformations, cracking of the resist and delamination of the structures from the substrate [26].

After development, the photoresist is dried with a stream of nitrogen or air [81]. Proper drying of the resist is especially important in the development of densely packed HAR arrays as the strong capillary forces of PGMEA, which act upon the structure's sidewalls, can bend and pull the structures together [3]. After drying, the collapsed structures will remain joint together due to stiction forces, as seen in figure 27 (b) [26]. The collapse of microstructures can be prevented by thoroughly rinsing the substrate with isopropanol prior to drying. Isopropanol has a lower surface tension than PGMEA, which greatly reduces the capillary forces that act upon the sidewalls of the microstructures [25]. Figure 27 (a) shows a schematic presentation on the forces acting upon HAR microstructures during drying.

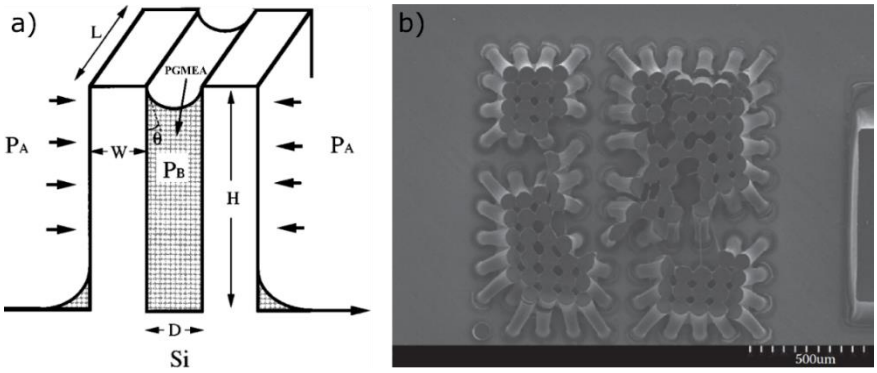

Figure 27: (a) Schematic presentation on the forces acting upon the sidewalls of HAR microstructures during drying. The surface tension of the developer pulls against any structure that the developer is attached to [83]. *(b) SEM image of collapsed SU-8 pillars. The structures remain joined together due to stiction forces* [25].

4.2.7 Hard baking

Whenever the SU-8 microstructures are to remain on the substrate as part of the final device, a hard bake of the photoresist is recommended. Hard baking of SU-8 is typically performed at temperatures between 150 and 200 °C, and can be conducted either on a hotplate or in a convection oven [81]. Hard baking removes any residual solvent left in the resist and anneals the structures, thereby further improving the stability and adhesion of SU-8 to the substrate, as well as increasing the hardness of the resist [25], [26].

4.3 Suspended SU-8 microstructures

The fabrication of substrate-bound SU-8 microstructures is a relatively straightforward process, typically involving a single deposition, exposure and development step. On the other hand, the fabrication of suspended SU-8 microstructures is much more complicated, requiring the use of multilevel photolithography, sacrificial layers, release techniques or special exposure methods. Today, there are several different methods that can be used for the fabrication of such structures [84].

4.3.1 Sacrificial layers

One of the most common technique for the fabrication of suspended SU-8 microstructures is with the use of sacrificial layers. This method utilizes a patterned material, other than SU-8, to elevate and support the suspended microstructures during the fabrication process. Once the SU-8 has been fully polymerized and developed, the sacrificial layer is removed from the substrate, leaving behind a suspended structures [84], [85].

The fabrication process works by first depositing and patterning the sacrificial material on the substrate. The specific deposition and patterning technique depends on the type of material used as well as the thickness of the layer. Next, a layer of SU-8 is deposited on the substrate surface, covering both the substrate and the sacrificial layer. In order to obtain suspended structures, the thickness of the SU-8 film must be greater than that of the sacrificial layer. After soft baking, the SU-8 layer is exposed. Areas where the exposed SU-8 is in direct contact with the substrate will act as the anchor points, while areas where the exposed resist is deposited on top of the sacrificial layer will turn into suspended structures. The last steps involve the development of the SU-8, followed by the removal of the sacrificial layer by means of wet etching [84], [85]. Figure 28 shows the process flow for the fabrication of SU-8 bridges and mushrooms with the use of a positive photoresist as the sacrificial layer.

In the past, several different materials have been used as sacrificial layers, including Ti, Cu [86], [87], SiO_2 [88] as well as other photoresists [30], [31], [89], [90]. When selecting the sacrificial material, an important property is a good wetting of the material by SU-8 [26]. Another important factor is the thickness of the sacrificial layer. Thin inorganic films (up to 1 µm) can be deposited through PVD or CVD methods, while thicker layers require the use of electroplating [84]. On the other hand, polymers can be easily deposited by means of spin coating, with thicknesses ranging anywhere up to hundreds of microns.

The use of photoresists as a sacrificial material offers several advantages over inorganic materials; (i) Spin coating allows for a much simpler and less expensive deposition of the sacrificial layer, while simultaneously offering a greater range of film thicknesses. (ii) Patterning of inorganic materials requires the use of an additional photolithography step which increases both the fabrication times and costs. (iii) The etching rates of inorganic materials are very low and require the use of strong acids which can potentially damage the SU-8 [85], [86]. Positive photoresists are more commonly used as sacrificial layers as they are easier to remove from the substrate without damaging the SU-8 in the process.

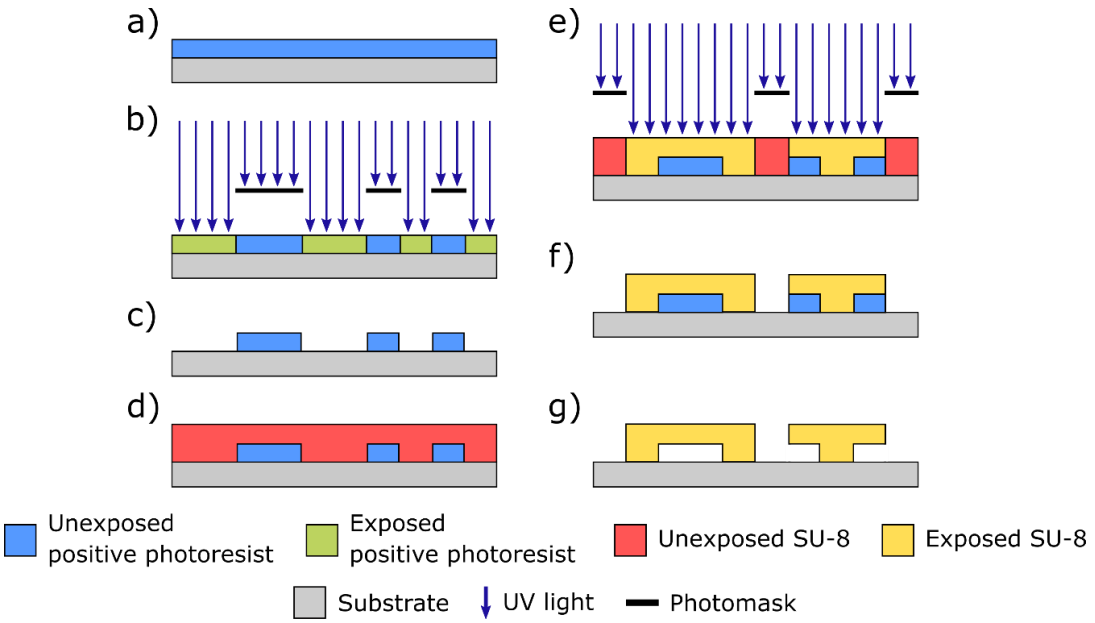

Figure 28: Process flow for the fabrication of suspended SU-8 microstructures with the use of a positive photoresist as a sacrificial layer. (a) First, the positive photoresist is deposited on the substrate and (b) patterned with the use of UV photolithography. (c) After developing the sacrificial layer, (d) a layer of SU-8 is deposited on top of the substrate and (e) exposed with UV light. The final steps involve (f) the development of the SU-8 and (g) removal of the sacrificial layer.

Positive photoresists as a sacrificial material

Positive photoresists are typically comprised of a Novolak phenol-formaldehyde resin, an organic solvent (typically PGMEA), and a diazonaphthoquinone (DNQ) photoinitiator [91]. The fabrication steps and parameters used in the processing of positive photoresists are similar to those of SU-8 and include; deposition, soft baking, exposure, development and hard baking.

Spin coating of positive resists allows for the deposition of films with thicknesses ranging anywhere up to tens of microns [92]. Exposure is most commonly performed with 365 nm (i-line), 405 nm (h-line) or 435 nm (g-line) wavelengths [93]. Upon exposure, the DNQ is converted into a carboxylic acid which increases the solubility of the resin in the developer by up to three times to that of the unexposed resist [91]. Development is performed by submerging the resist in a solution containing either sodium hydroxide, potassium hydroxide or tetramethylammonium hydroxide (TMAH) [94]. The patterned resist can then be easily removed from the substrate with the use of organic solvents including acetone, N-methyl-2-pyrrolidone (NMP) or dimethyl sulfoxide (DMSO) [95].

Although the use of positive photoresists as a sacrificial material offers several advantages over inorganic layers, there are two important issues with these materials that must be addressed. The first issue is that SU-8 can readily attack the positive resist, causing a partial or complete dissolution of the sacrificial layer [86], [90], [96]. For thicker sacrificial layers, a partial disolution can lead to a significant loss in the resolution of the fabricated microstructures and a substantial increase in the surface roughness of SU-8. For thinner sacrificial layers, this can even result in the complete dissolution of the positive resist by SU-8, meaning that a suspended structure can no longer be fabricated. Dissolution of the

sacrificial layer can be prevented by coating the positive resist with a thin inorganic film (e. g. Cr, Ti, SiO_2) before the deposition of SU-8, thereby effectively separating the two resists. These films are typically deposited by means of sputtering, with thicknesses ranging in the tens of nanometers [86], [90].

Another common issue with positive photoresist is the thermal reflow of the resist during hard baking. Hard baking of positive photoresists is typically performed at temperatures close to their glass transition temperature (T_g). At this point, the photoresist softens and starts rounding in an attempt to minimize the energy of the system [97]. The thermal reflow of the resist can thus cause lower resolution, reduced dimensional accuracies as well as rounding of suspended structures. Figure 29 shows SEM images of positive photoresist arrays before and after a thermal reflow.

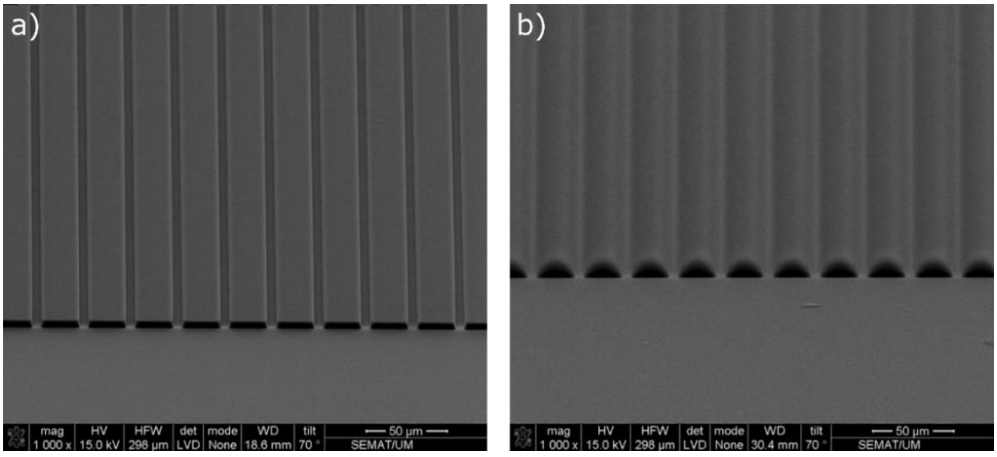

Figure 29: SEM images of AZ 4562 arrays (a) before and (b) after a thermal reflow [97].

Both the thermal reflow and the dissolution of positive photoresists can be prevented through various resist hardening treatments, such as UV curing. UV curing involves exposing the patterned resist with wavelengths between 200 and 300 nm. The short wavelengths create a highly polymerized layer on the surface of the resist which allows the material to withstand attacks from SU-8 and temperatures of up to 280 °C without undergoing a thermal reflow [98].

4.3.2 Other fabrication methods

Greyscale photolithography

Greyscale photolithography is a technique in which suspended SU-8 microstructures are fabricated through a partial exposure of the resist. The method relies on the absorption of UV light as it travels through the SU-8, leading to lower exposure energies in the bottom layers of the resist than at the top [7]. As a result, only the upper layers of the resist receive a sufficient exposure dose to initiate the cross-linking process, while the bottom layers remain unexposed. Compared to the normal exposure of SU-8, greyscale photolithography can be conducted by either significantly decreasing the initial exposure dose [9], [44], exposing the resist with wavelengths below 350 nm [99] or by utilizing special greyscale photomasks [7].

The fabrication process works by first depositing a layer of SU-8 on the substrate. Next, the resist is fully exposed in areas where the anchor points are to be fabricated. After exposing the resist for the first time, the photomask is changed and the resist is exposed again in areas where the suspended structures are to be fabricated. However, this time the exposure is altered so that only the upper portion the resist receives a sufficient exposure dose to initiate the cross-linking process, thereby leaving the bottom portion unexposed. After the second exposure, the photoresist is developed [44], [99]. Figure 30 shows the process flow for the fabrication of SU-8 bridges and mushrooms by means of greyscale photolithography.

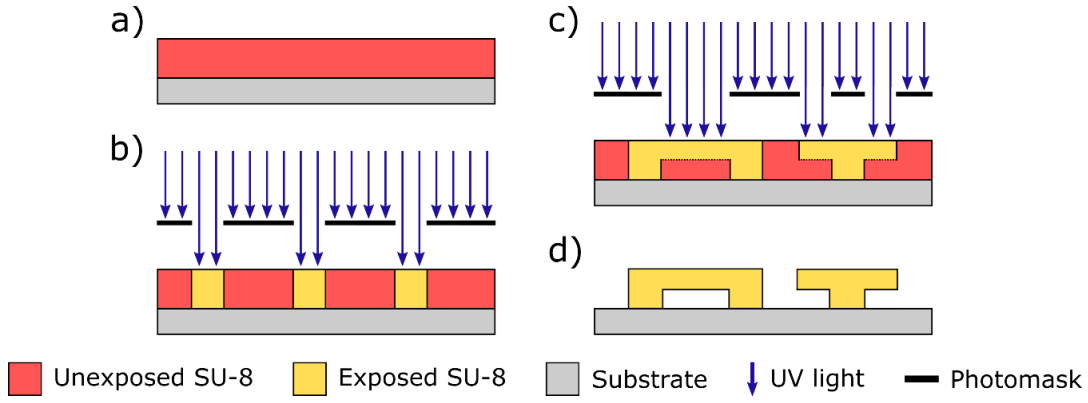

Figure 30: Process flow for the fabrication of suspended SU-8 microstructures with the use of grayscale photolithography. (a) First, a layer of SU-8 is deposited on a substrate. (b) Next, the anchor points are fully exposed. (c) After exposure, the photomask is changed and the resist is exposed again. However, this time the exposure is altered so that the resist is only partially exposed. (d) This results in the removal of the lower parts of the partially exposed resist during development, thereby creating a suspended structure.

One of the major drawbacks of greyscale photolithography is the poor control over the exposure depths, as even minor variations in the exposure dose can have a significant influence on the final depth in which cross-linking takes place. Another issue with greyscale photolithography is that the uneven exposure of SU-8 at varying depths can lead to the formation of intrinsic stress, which can subsequently cause bending of the suspended microstructures [99].

Buried mask method

The buried mask method involves the use of a UV blocking mask "buried" between two layers of SU-8. The UV blocking mask impedes the passage of light, thereby allowing for a full exposure of the upper SU-8 layer while leaving the bottom layer unexposed [99].

The fabrication process works by first depositing a layer of SU-8 on the substrate. Next, the resist is exposed in areas where the anchor points are to be fabricated. After the post-exposure bake, a thin UV blocking film is deposited on top of the SU-8 layer which can then be patterned or be left unpatterned. The specific deposition and patterning technique depends on the type of material used. Afterwards, a second SU-8 layer is deposited on top of the UV blocking layer and exposed in areas where the suspended structures are to be fabricated. Due to the presence of the UV blocking mask, only the upper SU-8 layer is exposed while leaving the bottom layer unexposed. The final steps involve the development of the SU-8 and removal of the buried mask by means of wet etching [99]. Figure 31 shows the process flow

for the fabrication of suspended SU-8 microstructures with the use of the buried mask method.

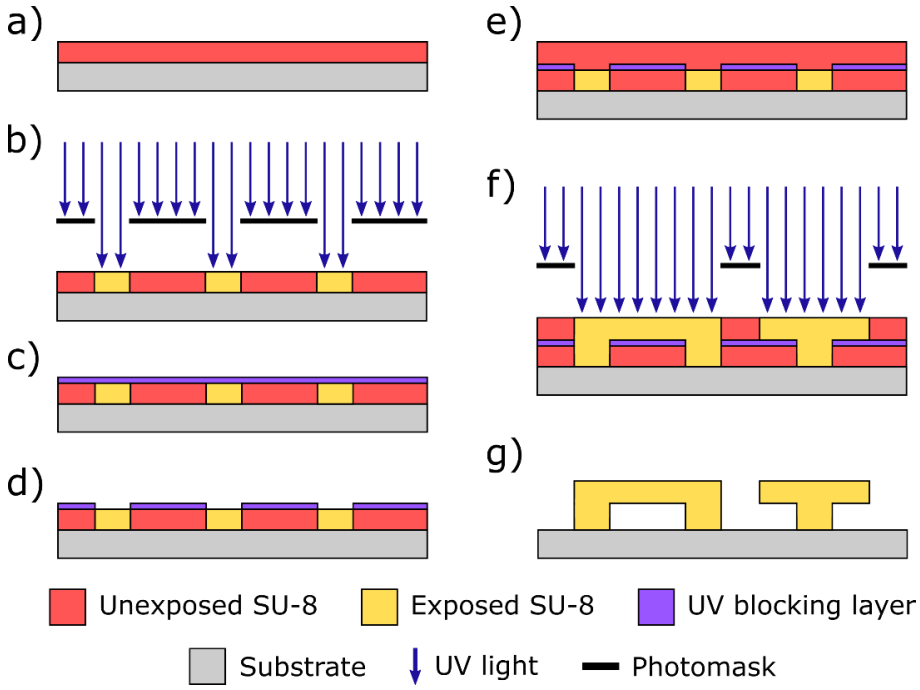

Figure 31: Process flow for the fabrication of suspended SU-8 microstructures with the use of the buried mask method. (a) First, a layer of SU-8 is deposited on the substrate and (b) exposed in areas where the anchor points are to be fabricated. (c) Next, a thin UV blocking layer is deposited on top of the SU-8 layer. (d) This layer can then be patterned, thus allowing for the suspended structures to be directly attached to their anchor points. (e) The next step involves the deposition of a second SU-8 layer (f) and exposing the resist in areas where the suspended structures are to be fabricated. Due to the presence of the UV blocking layer, only the upper SU-8 layer is exposed. (g) After the second exposure, the SU-8 is developed and the mask is removed by means of wet etching, thereby creating a suspended structure.

The UV blocking material can either be a metal [99] or polymer (photoresist) [96]. Metal UV blocking layers typically require a thickness in the range of tens of nanometers. Their deposition technique is limited to thermal evaporation as sputtering, electron-beam PVD and CVD methods produce too much heat and radiation which can initiate the cross-linking of the unexposed SU-8. Furthermore, there are also significant limitations as to the specific metals that can be used. First, the deposited metal should allow for a reasonable evaporation rate at sufficiently low temperatures, so as not to heat-up the unexposed resist and initialize the cross-linking process. Second, the metal should emit a minimum amount of radiation during heating. Third, the metal can only be patterned by means of wet etching, as dry etching produces too much heat and radiation. Some metals that can be used as UV blocking layers include Al, Cr, Zn and Mg [99].

Compared to metal UV blocking layers, photoresists do not completely block the passage of light but rather delay it long enough for the upper SU-8 layer to be completely exposed, while leaving the bottom layer unexposed. The main concern with these masks is that the SU-8 can easily attack and dissolve the positive resist. Thus, the UV blocking mask must be sufficiently thick, typically in the order of a few microns [96].

The UV blocking layer can be patterned or be left unpatterned. By patterning the mask, the suspended structures can be directly attached to the anchor points. On the other hand, if the UV blocking layer is left unpatterned, the mask will remain trapped between the anchor point and suspended structure after development [99]. This can potentially prevent further processing of the SU-8, such as pyrolysis, so a patterned mask is more desirable. Unpatterned photoresist masks also run the risk that the SU-8 developer can dissolve the UV blocking layer, thereby separating the suspended structure from its anchor point [96].

SU-8 foil techniques

The main principle behind SU-8 foil techniques is the lamination of an unpolymerized SU-8 foil on top of patterned SU-8 microstructures [100], [101]. The fabrication process works by first depositing a layer of SU-8 on the substrate and exposing the resist in areas where the anchor points are to be fabricated. After developing the SU-8, an unpolymerized SU-8 foil is laminated on top of the patterned SU-8 structures with the use of a hot roller laminator at temperatures between 60 and 80 °C. The final steps involve exposing the SU-8 foil in areas where the suspended structures are to be fabricated and its subsequent development [100]. Figure 32 shows the process flow for the fabrication of SU-8 bridges and mushrooms with the use of SU-8 foils.

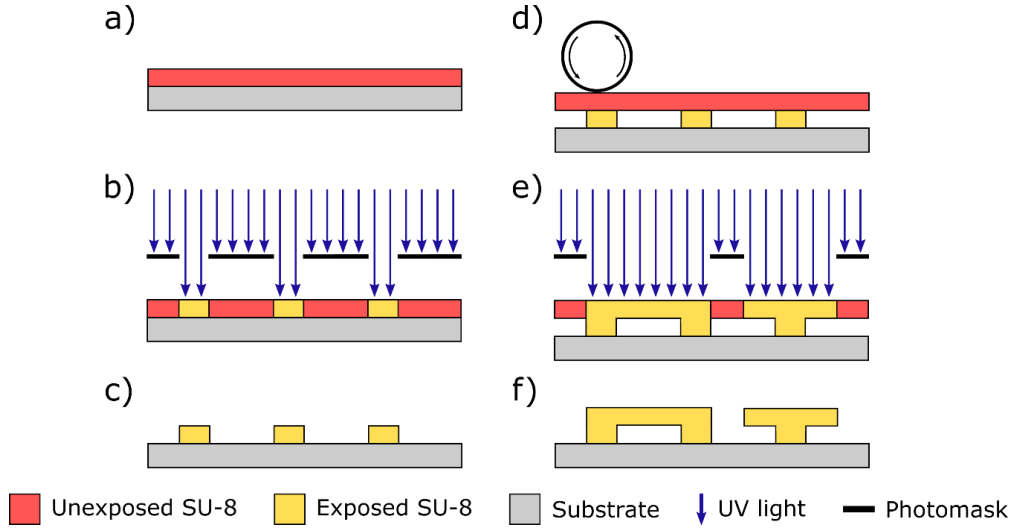

Figure 32: Process flow for the fabrication of suspended SU-8 microstructures with the use of SU-8 foils. (a) First, a layer of SU-8 is deposited on the substrate. (b) Next, the resist is exposed in areas where the anchor points are to be fabricated and (c) developed. (d) After development, an unpolymerized SU-8 foil is laminated on top of the anchor points with a hot roller laminator. (e) The final steps involve the exposure and (f) development of the SU-8 foil.

One of the main advantages of the SU-8 foil technique is that there is no material located directly underneath the suspended structures, thus allowing for a much simpler deposition, exposure and development of the resist. However, in order for the suspended structures to possess a high structural stability, a good adhesion between the SU-8 foil and anchor points is crucial [100]. SU-8 foils can either be bought commercially [100] or fabricated by depositing and soft baking a layer of SU-8 on a flexible polymeric substrate [101]. Flexible substrates allow for the fabrication of SU-8 foils with thicknesses of over 100 µm [101].

Substrate bonding techniques

Suspended SU-8 microstructures can also be fabricated by patterning the anchor points and suspended structures on sperate wafers and then bonding the two substrates together. This technique typically requires that at least one of the substrates be transparent, such as a glass wafer, so that a proper alignment of the structures can be done. The substrates are aligned and bonded in a vacuum atmosphere, using a dedicated wafer bonding system. Since the SU-8 structures are fully polymerized, high pressures (~3 bars) and high temperatures (100 - 120 °C) are required in order for the two layers to successfully bond to one another. Once the microstructures are successfully bonded the are released from one of the substrates [102]. Figure 33 shows the process flow for the fabrication of suspended SU-8 microstructures with the use of the substrate bonding technique.

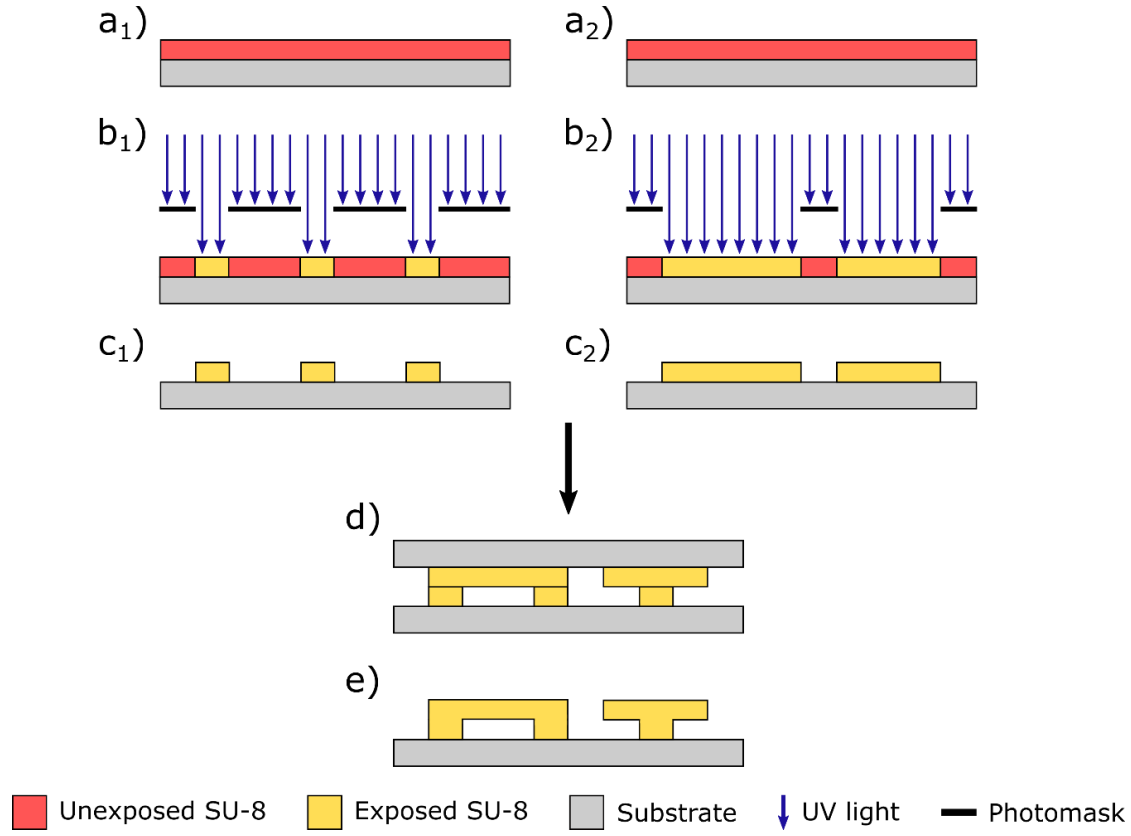

Figure 33: Process flow for the fabrication of suspended SU-8 microstructures with the use of substrate bonding techniques. (a) First, two SU-8 layers are deposited on separate substrates. (b) Next, the SU-8 layers are exposed so that one substrate contains the anchor points while the other substrate contains the suspended structures. (c) After exposure, the SU-8 layers are developed. (d) Once the microstructures have been developed, the two SU-8 layers are aligned and bonded together under the application of high pressures and heat. (e) The final step involves releasing the suspended structures from the substrate.

The main challenge of substrate bonding techniques is the separation of the fabricated structures from the wafer, as fully polymerized SU-8 is very difficult to remove from rigid substrates. One solution to this problem was proposed by Tuomikoski and Franssila [103], who dissolved an entire glass wafer in hydrofluoric acid, thereby releasing the device.

Suspended SU-8 microstructures through T-topping

Although T-topping of microstructures is generally undesirable, this phenomenon can be used as a tool for the fabrication of suspended SU-8 wires and bridges. As discussed in section 4.2.4, T-topping can occur either due to an overexposure of the SU-8 film or due to the diffraction of light from the edges of the photomask patterns. The T-topping of densely packed pillars can lead to the connection between the tops of two or more structures, thereby creating suspended structures. However, the main disadvantage of this technique is the poor control and limitations over the shape and size of the structures that can be fabricated [3].

4.4 Pyrolysis of SU-8

Pyrolysis of SU-8 at temperatures above 800 °C results in the formation of pyrolytic carbon. The pyrolysis process of SU-8 can be divided into three stages; (i) pre-carbonization, (ii) carbonization and (iii) annealing [7];

(i) Pre-carbonization takes place at temperatures up to 300 °C. During this stage, the remainder of the SU-8 solvent is removed from the resist along with any unreacted monomers. This increases the hardness of the SU-8 and enhances its adhesion to the substrate.

(ii) Carbonization takes place at temperatures ranging from 300 to 1200 °C and can be further divided into two sub-stages; (a) the first sub-stage occurs at temperatures between 300 and 500 °C. During this stage the oxygen atoms are removed from the SU-8, resulting in a significant loss of mass and high levels of shrinking. At the same time, a network of conjugated carbon systems begins to form. (b) The second sub-stage occurs at temperatures between 500 and 1200 °C. During this stage, hydrogen and the remainder of oxygen atoms are removed from the precursor, resulting in the formation of an interconnected aromatic carbon network. At this point, the density, hardness, Young's modulus and the electrical conductivity of the material significantly increase.

(iii) The final step involves the annealing of pyrolytic carbon at temperatures above 1200 °C. During this step, structural defects and impurities are gradually eliminated from the material while the crystal structure of pyrolytic carbon increases both in size and ordering. At temperatures between 2500 and 3300 °C all defects are eliminated from the material [67].

4.4.1 Pyrolysis parameters

Since the structure and properties of pyrolytic carbon is strongly related to the specific pyrolysis conditions, each parameter must be carefully optimized in order to obtain the desired mechanical, electrical and electrochemical properties of the material. The most significant pyrolysis parameters include; the pyrolysis temperature [15]–[17], [44], [53],

dwell time [19], [20], [53], heating rate [16], [18], [20], [21], [104], number of heating steps [3], [105] and the pyrolysis atmosphere [3], [15], [19].

Pyrolysis of C-MEMS is typically carried out in a quartz or alumina tube furnace, under the presence of an inert gas, such as nitrogen or forming gas (95 % N_2, 5 % H_2), with a flow rate of approximately 2000 ml/min. The standard pyrolysis procedure involves a two-step process. First, the SU-8 is heated up with a heating rate of 10 °C/min to a temperature between 200 and 300 °C, where it is kept for a period of one hour. Next, the resist is heated up to its final pyrolysis temperature at 900 °C with a heating rate of 10 °C/min, followed by a minimum dwell time of one hour. The final step involves a natural cooling of the pyrolytic carbon in the furnace [7].

Pyrolysis temperature

The pyrolysis temperature is maximum temperature at which the precursor is pyrolyzed and is the single most important pyrolysis parameter that determines the properties and microstructure of pyrolytic carbons. Higher pyrolysis temperatures allow for a greater thermal decomposition of the precursor and increased outgassing rates of volatile atoms, resulting in higher levels of carbonization [15]. The carbon content of pyrolyzed SU-8 is expected to exceed 90 wt. % when pyrolyzed at 900 °C and more than 99 wt. % when pyrolyzed at 1300 °C [7]. Higher temperatures also lead to a higher sp^2 content and bigger graphitic crystallites, due to a greater mobility of carbon atoms [53], [54].

The electrical and electrochemical properties of pyrolytic carbons are primarily attributed to the degree to which the precursor is graphitized, meaning that higher pyrolysis temperatures will result in lower electrical resistivities [16], [53]. Studies have shown that the greatest drop in the electrical resistivity of SU-8 occurs at temperatures between 700 and 800 °C [15], [16] and is attributed to the outgassing of hydrogen atoms [13], [17]. By increasing the pyrolysis temperature further, the electrical resistivity continues to decrease. However, the changes become more gradual as the level of carbonization gets closer to its maximum. From that point on, any further changes in the electrical properties of the material can be attributed to an increase in the sp^2 content and crystallinity of the microstructure.

Dwell time

Dwell times have a similar effect to that of pyrolysis temperatures, whereby longer dwell times lead to a higher degree of carbonization and greater crystallinity of the material. This is because longer dwell times provide more time during which the thermal decomposition of the precursor and reorganization of carbon atoms can take place [20]. However, longer dwell times have a less significant impact on the materials structure and properties than higher pyrolysis temperatures [53]. Table 3 shows a comparison between the electrical properties of SU-8 derived pyrolytic carbons pyrolyzed at different temperatures and dwell times.

It should also be noted that both the pyrolysis temperature and the dwell time have no significant impact on the surface roughness of pyrolytic carbons, which remains below 1 nm when standard heating rates are applied [17], [44].

Table 3: Electrical resistivity of SU-8 derived pyrolytic carbons pyrolyzed at different temperatures and dwell times. The results show that higher pyrolysis temperatures have a greater effect on the properties of pyrolytic carbons than longer dwell times.

Temperature [°C]	Dwell time [h]	Resistivity [Ωm]	Reference
800	1	$4.76 \cdot 10^{-4}$	[53]
	4	$1.73 \cdot 10^{-4}$	
	8	$1.73 \cdot 10^{-4}$	
900	1	$1.22 \cdot 10^{-4}$	
	4	$9.6 \cdot 10^{-5}$	
	8	$9.0 \cdot 10^{-5}$	
1000	1	$6.8 \cdot 10^{-5}$	
1100	1	$4.2 \cdot 10^{-5}$	[20]
	3	$3.4 \cdot 10^{-5}$	
	5	$3.2 \cdot 10^{-5}$	

Heating rate

As discussed earlier, pyrolysis involves the thermal decomposition of a hydrocarbon precursor, followed by the outgassing of volatile atoms and rearrangement of carbon atoms. When low heating rates are applied (< 15 °C/min), the decomposition of the precursor occurs very gradually, resulting in low outgassing rates. This, in turn, allows the volatile atoms to remove themselves from the precursor without distorting the materials structure [104].

As the heating rates are increased, the thermal decomposition and outgassing rates become greater. When the heating rate is increased above 15 °C/min, the decomposition rate of SU-8 becomes so high that the outgassing rates can no longer keep up. As a result, oxygen and hydrogen atoms become trapped within the carbon matrix and start to form micron-sized gaseous pores, as seen in figure 34 [18], [104]. By etching the surface of pyrolytic carbon, the pores can be uncovered, leading to a significant increase in the materials surface area.

This effect may not be entirely undesirable as an increase in the effective surface area of pyrolytic carbon improves its performance in devices such as electrochemical sensors and energy storage systems. For example, Sharma *et al.* [104] reported that by pyrolyzing SU-8 films at a heating rate of 50 °C/min they were able to increase the surface area of pyrolytic carbon electrodes by ~3 times. As a result, this led to an increase in the electrode capacitance by 15 times and the specific capacitance by 5 times.

While rapid pyrolysis of SU-8 can provide some significant advantages to C-MEMS, it can also cause various adversary effects. For example, the formation of gaseous pores significantly increases the intrinsic stress which can lead to cracking and delamination of pyrolytic carbon from the substrate. Higher heating rates can also cause stress due to the formation of thermal gradients throughout the material, as well as due to the difference in the coefficient of thermal expansion between the substrate and pyrolytic carbon [16]. Stress can also occur during cooling, which is why the cooling rates must also be sufficiently controlled. Furthermore, Sharma *et al.* [104] also reported that higher heating rates would lead to a lower sp^2 content, thus suggesting a trade-off between a higher surface area and better electrical properties of pyrolytic carbon.

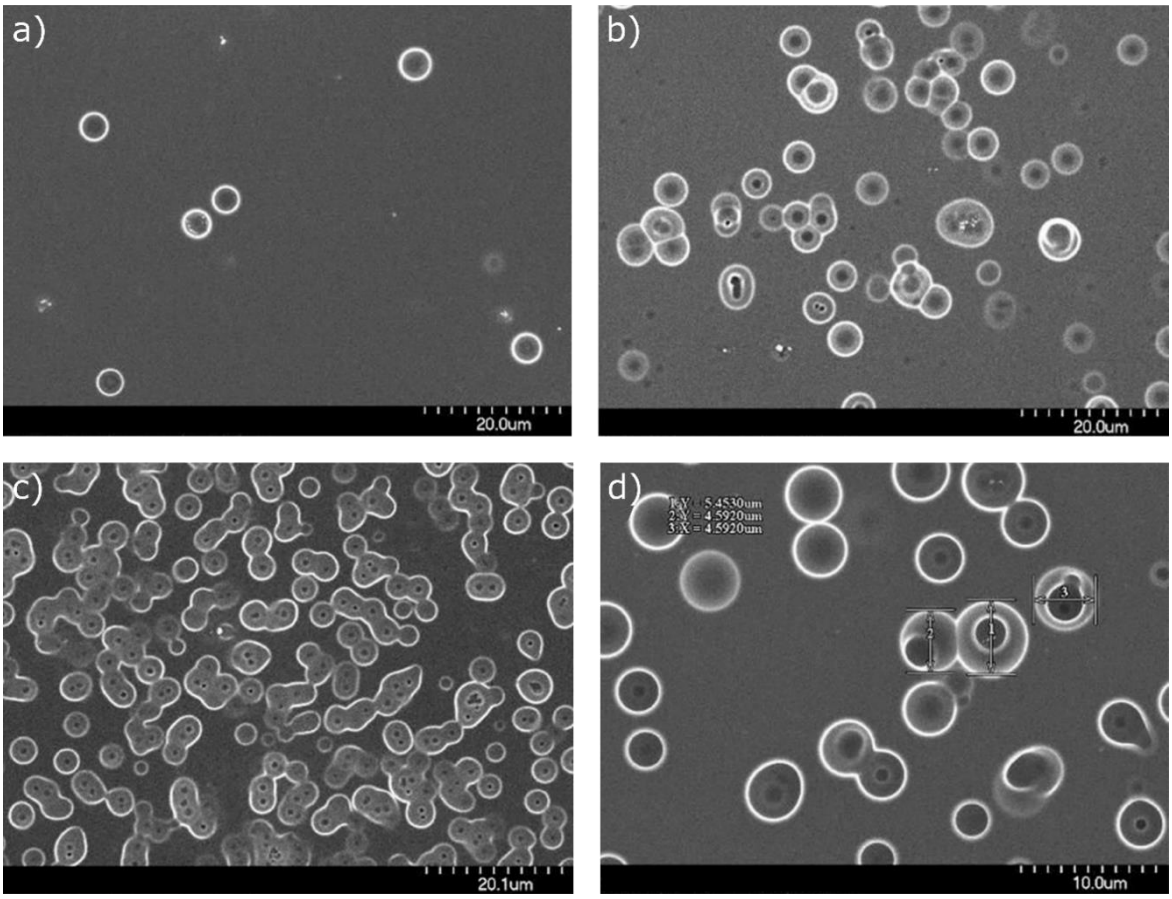

Figure 34: SEM images of pyrolytic carbon films derived through rapid pyrolysis of SU-8 at heating rates of (a) 25 °C/min, (b) 50 °C/min and (c) 75 °C/min. The images show that the number of pores significantly increases with higher heating rates while their relative size remains the same. (d) The diameter of the gaseous pores is approximately 5 µm [104].

Heating rates have also shown to have an effect on the shrinking of the precursor. Higher heating rates reduce the time during which the carbon atoms can rearrange themselves and form new carbon-carbon bonds. As a result, the carbon atoms are much more likely to react with volatile atoms during outgassing and form organic compounds, which are then eliminated from the precursor. This, in turn, leads to an increase in mass loss and greater shrinking of the precursor [20].

Heating steps

The number of heating steps refers to the number of intermediate dwell times as the precursor is heated towards the final pyrolysis temperature. A single step process involves heating up the precursor directly to its final pyrolysis temperature, without any intermediate dwell times in between. On the other hand, multi-step processes involve the implementation of several intermediate dwell times at varying temperatures, as the precursor is heated towards its final pyrolysis temperature.

Pyrolysis of SU-8 is accompanied by a significant amount of intrinsic stress induced by the outgassing of volatile atoms as well as difference in the coefficient of thermal expansion between the substrate and SU-8. This stress can cause distortion of the patterned structures, the formation of cracks and even delamination of pyrolytic carbon from the substrate.

Previous studies have shown that the use of a single step process for SU-8 would result in poorly fabricated structures due to a significant buildup of intrinsic stress [3]. By introducing a two-step pyrolysis process, the resist is able to relieve some of its stress and increase its adhesion to the substrate, thereby allowing the precursor to be heated to higher temperatures without the risk of cracking or delamination. To reduce the intrinsic stress even further, more steps can be added to the pyrolysis process.

Pyrolysis atmosphere

Pyrolysis of hydrocarbons must be conducted in an inert atmosphere in order to prevent the precursors from combusting [7]. This can be done either in a vacuum or in the presence of an inert gas, such as nitrogen, argon or forming gas (95 % N_2, 5 % H_2). Pyrolysis in a vacuum atmosphere tends to result in a slightly higher degree of carbonization due to faster outgassing rates [15]. However, the faster outgassing rates also lead to the formation of intrinsic stress which can cause the formation of cracks and delamination of the material from the substrate [3].

The pyrolysis atmosphere also has an effect on the level of shrinking of the precursor. For example, Ranganathan *et al.* [15] reported that by using a nitrogen atmosphere they were able to achieve a ~20 % higher reduction in the thickness of pyrolytic carbon sheets, as opposed to pyrolysis in a high vacuum atmosphere. Similarly, Lyons *et al.* [106] reported a ~10 % greater shrinkage of pyrolytic carbon when using a pure H_2 atmosphere, as opposed to a N_2 atmosphere. The difference in shrinking was attributed to the reaction between the hydrogen atmosphere and the pyrolytic carbon, resulting in the formation of hydrocarbon byproducts (e. g. methane) which were eliminated from the material.

4.4.2 Shrinking of SU-8

Pyrolysis of hydrocarbons is accompanied by a significant loss of mass and shrinking of the precursor. The shrinking of SU-8 is greatest during the initial stages of pyrolysis (between 300 and 500 °C) and is primarily attributed to the outgassing of oxygen atoms [9], [16]. The degree to which the SU-8 shrinks depends on several factors, including the pyrolysis conditions [7], [23], the shape and size of the precursor [107] as well as the level of cross-linking within the polymer matrix [108].

Studies have shown that the precursor's initial geometry has a significant influence on the level of shrinking, whereby smaller structures will experience a greater contraction than bigger structures. For example, Martinez-Duarte *et al.* [23] reported a 86 % vertical shrinkage for 10 µm tall SU-8 pillars but only a 37 % shrinkage for 300 µm tall pillars, while using the same pyrolysis conditions. The difference in the level of shrinking is a consequence of varying surface-to-volume ratios between the two structures. The small surface-to-volume ratio of larger structures impedes the efficient outgassing of volatile atoms as the atoms have to travel larger distances to reach the surface of the precursor. This not only leads to a smaller reduction in size but also to a lower degree of carbonization [17]. Figure 35 shows the relationship between the degree of vertical shrinking and the initial height of SU-8 pillars.

The influence of the precursor's geometry even goes as far as to have a separate effect on the degree of vertical and lateral contraction. Studies have shown that the vertical shrinking depends upon the outgassing of atoms through the top of the precursor structure, while the lateral shrinking depends upon the outgassing of atoms through the sidewalls of the precursor structure [109]. As a result, this creates a difference in the level of vertical and lateral contraction between two structures with the same surface-to-volume ratio but different dimensions. For example, a HAR structure will experience a smaller vertical contraction but a larger lateral contraction than a low-aspect ratio structure.

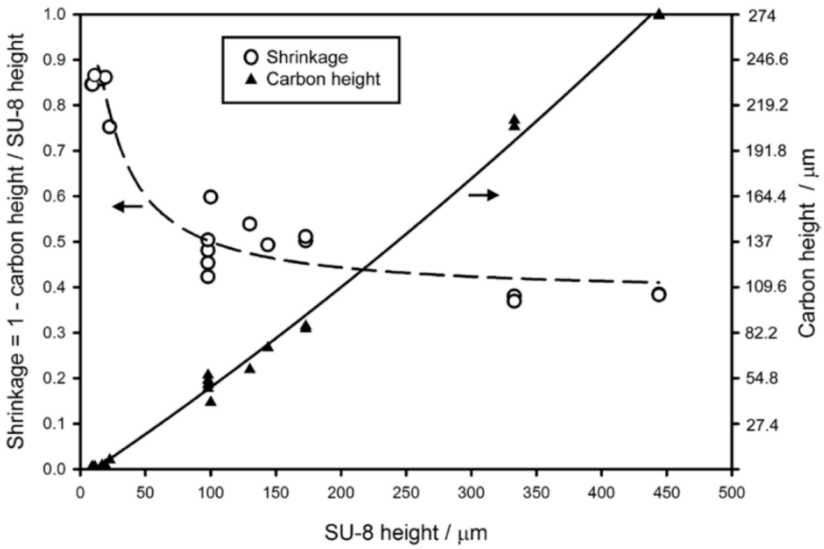

Figure 35:Vertial shrinking of SU-8 pillars as a function of their initial height. The level of shrinking becomes greater as the structures get smaller, due to a much more efficient outgassing of volatile atoms. The pyrolysis was conducted at 900 °C, with a dwell time of 1 hour and a heating rate of 10 °C/min [23].

Substrate-bound structures also tend to experience a non-isometric lateral contraction due to the strong adhesion of SU-8 to the substrate, which restricts the shrinking of the precursor near its base [23]. As we move further away from the substrate the lateral contraction becomes less restricted, allowing for the precursor to freely shrink inwards. As a result of this non-uniform contraction, the sidewalls of pyrolytic carbon microstructures tend to be slanted near the base of the structure, as seen in figure 36 (b) [9].

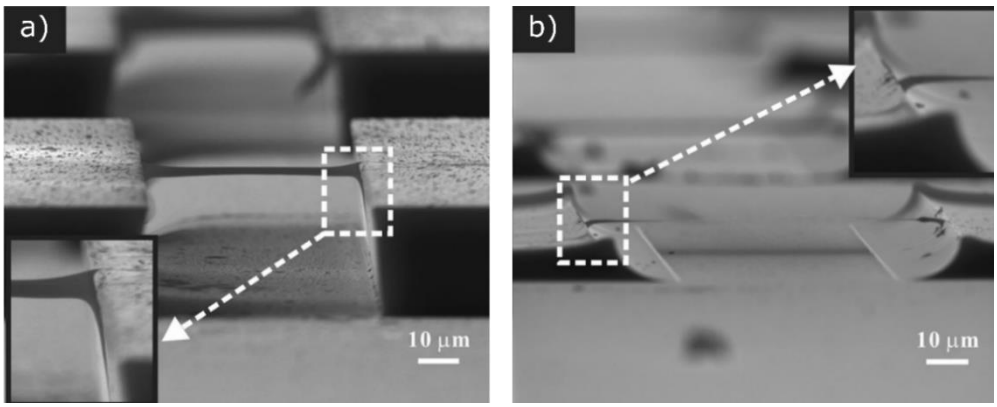

Figure 36: SEM images of a suspended SU-8 wire (a) before and (b) after pyrolysis. Pyrolysis causes a significant elongation of the wire due to the lateral contraction of the anchor points. The sidewalls of the anchor points also become distinctively slanted due to the restricted lateral contraction of SU-8 near the base of the structure [9].

The shrinking of suspended microstructures differs between the different structural types. For example, structures that are attached to a single anchor point (e. g. mushrooms and cantilevers) are able to shrink freely in all directions [12], [44]. On the other hand, structures that are suspended between two or more anchor points (e. g. wires, bridges and membranes/meshes) experience a lateral contraction perpendicular to the anchor points but a lateral extension towards the anchor points. The extension of these structures is caused by the lateral contraction of the anchor points to which the suspended structures are attached to and result in the buildup of a significant amount of tensional stress within the structure [9], [30]. Figure 36 and 37 show the difference in the length of a suspended nanowire before and after pyrolysis.

Suspended C-MEMS also tend to exhibit a distinctive upwards deflection, as seen in figure 7 (b). This is caused by the non-uniform lateral contraction of the anchor points, which pull the suspended structures further back at the top of the structure than at the bottom [9], [12]. As a result, the suspended structures experience higher levels of stress at the top than at the bottom, thereby causing the formation of a transverse stress gradient throughout the height of the structure which bends the structure upwards [9], [30].

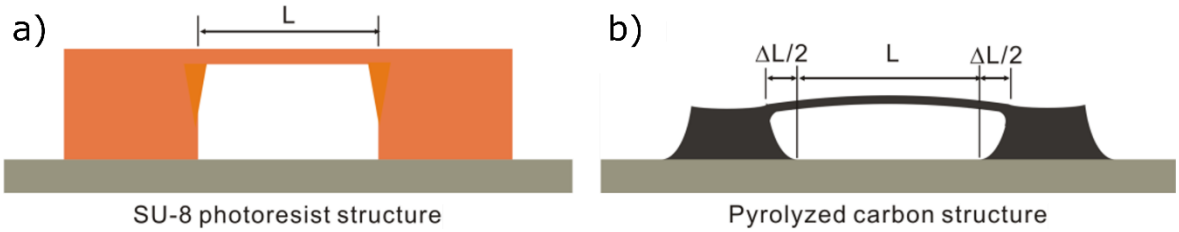

Figure 37: Schematic presentation of an SU-8 bridge (a) before and (b) after pyrolysis. The uneven lateral contraction of the anchor points causes the bridge to extend and deflect upwards [9].

Often times, the performance of a C-MEMS device depends on the surface area or distances between the various pyrolytic carbon structures, as is the case in redox based electrochemical sensors. Therefore, the initial design of the system must always account for the shrinking of the precursor during pyrolysis. For example, Martinez-Duarte *et al.* [23] reported that the pyrolysis of SU-8 pillars with a 50 µm diameter, an aspect ratio of 4 and a 15 µm gap size resulted in the fabrication of pyrolytic carbon pillars with a 25 µm diameter, an aspect ratio of 3.6 and a 40 µm gap size.

Shrinking of precursor can also be used to our advantage. For example, Lim *et al.* [30] demonstrated that in the case of stacked carbon electrode sets, presented in chapter 2, the vertical contraction of the anchor points would pull the suspended electrode closer to the substrate-bound electrode, thereby reducing the gap between the electrodes from 3 to ~2.1 µm. As a result, this would lead to an increased redox cycling of the analyte and a significant signal amplification.

5. Experimental

The experimental part of this thesis is divided into two sections;

- In the first section, we investigate the crystallinity, electrical resistivity and surface roughness of pyrolytic carbon films in relation to the pyrolysis temperature.
- In the second section, we investigate the structural stability and shrinking of suspended pyrolytic carbon microstructures with varying shapes and sizes.

In both parts, the pyrolytic carbon is derived through pyrolysis of SU-8 50, a negative photoresist provided by MicroChem Corp. The suspended microstructures are fabricated with the use of sacrificial layers, with AZ 4562, a positive photoresist provided by Microchemicals GmbH, as the sacrificial material.

Two different types of samples are to be prepared using standard photolithographic methods;

1) The first type of samples are unpatterned SU-8 films deposited on either a SiO_2 or Si_3N_4 substrate. Eight samples are prepared in total, four on a SiO_2 substrate and four on a Si_3N_4 substrate. The samples are divided into four groups, each group containing one sample deposited on the SiO_2 substrate and one sample on the Si_3N_4 substrate. Each group is then pyrolyzed at a different pyrolysis temperature.
2) The second type of samples are suspended SU-8 microstructures fabricated on a Si substrate. Sixteen samples are prepared in total, each containing four different types of suspended structures; bridges, membranes, cantilevers and mushrooms. Twelve samples are divided into groups of three, each of which is pyrolyzed at a different temperature. The remaining four samples are used as a reference. In addition, four samples containing only the patterned sacrificial layer are also prepared.

The pyrolysis temperatures for individual sample groups range from 800 to 1100 °C, in 100 °C increments. The fabrication process is optimized so that four samples can be obtained from a single silicon wafer with a 100 mm diameter.

5.1 Sample fabrication

The fabrication process for pyrolytic carbon films can be divided into three parts;

(i) Substrate preparation
(ii) SU-8 deposition, baking and exposure
(iii) High temperature pyrolysis of SU-8

On the other hand, the fabrication process for suspended SU-8 microstructures requires additional steps and can be divided into five parts;

(i) Substrate preparation
(ii) AZ 4562 deposition, baking, exposure and development
(iii) SU-8 deposition, baking, exposure and development
(iv) AZ 4562 removal
(v) High temperature pyrolysis of SU-8

Figure 38 and 39 shows the process flow used for the fabrication of pyrolytic carbon films and suspended pyrolytic carbon microstructures, respectively.

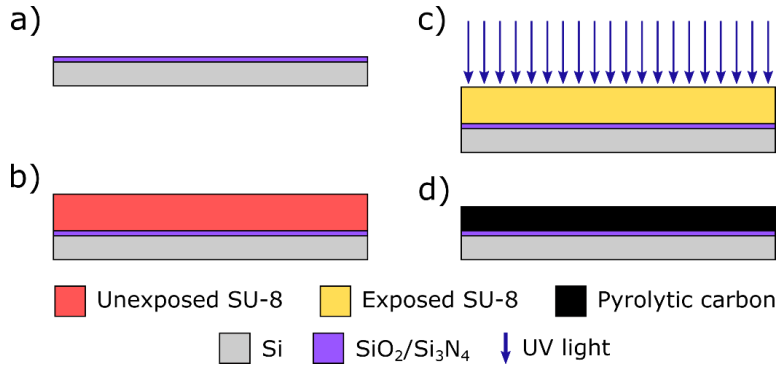

Figure 38: Process flow for the fabrication of pyrolytic carbon films. (a) First, a layer of SiO_2 or Si_3N_4 is deposited on a Si wafer by means of PECVD. (b) Next, a layer of SU-8 is deposited on top of the SiO_2/Si_3N_4 film and soft baked. (c) After soft baking, a flood exposure of the resist is performed with UV light, followed by a post-exposure bake. (d) The final step involves pyrolyzing the resist.

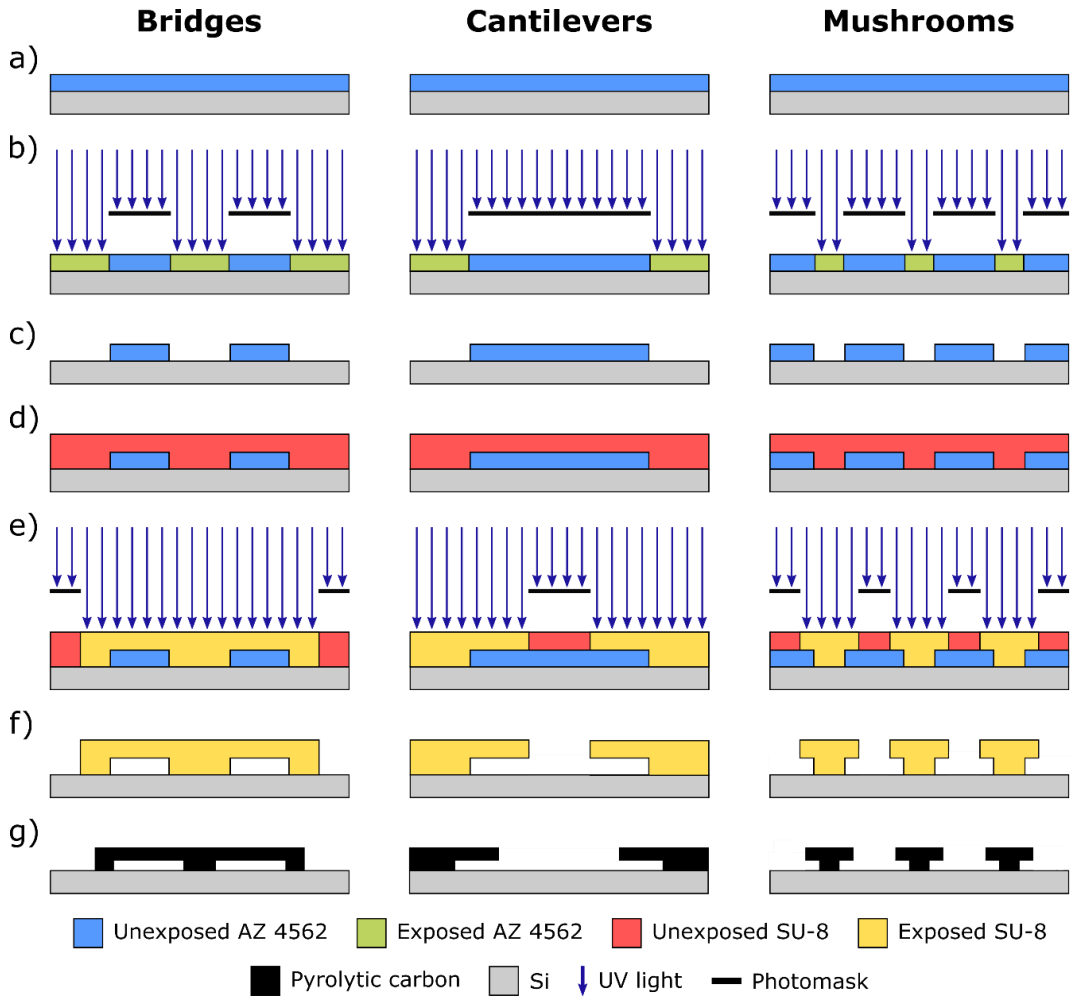

Figure 39: Process flow for the fabrication of pyrolytic carbon bridges, cantilevers and mushrooms. (a) First, the sacrificial layer is deposited on a Si substrate. (b) This is flowed by soft baking and exposure of the resist through a photomask with UV light. (c) Next, the sacrificial layer is developed and hard baked. (d) After hard baking, a layer of SU-8 is deposited on top of the substrate and soft baked. (e) Soft baking is followed by an exposure of the SU-8 through a photomask with UV light and a post-exposure baking step. (f) Afterwards, the SU-8 is developed and the sacrificial layer is removed. (g) The final step involves the pyrolysis of the SU-8 microstructures.

5.1.1 Photomask design

The fabrication of suspended SU-8 microstructures is performed by exposing the resists through plastic photomasks with an ink printed pattern and a protective emulsion layer, to prevent the contamination of the samples. The photomasks were designed by Joonas Heikkinen, Aalto University, and provided by Micro Lithography Services Limited. Four different types of suspended microstructures are designed; bridges, membranes, cantilevers and mushrooms.

Bridges

The SU-8 bridges are designed as a grid of overlapping SU-8 and AZ 4562 lines with varying widths. This allows for the fabrication of SU-8 bridges with lengths and widths ranging from 10 to 50 µm, in 10 µm increments, and from 100 to 500 µm, in 100 µm increments. The distance between individual lines of the same size is 50 µm for SU-8 and 80 µm for AZ 4562. Figure 40 shows the photomask designs used for the fabrication of SU-8 bridges.

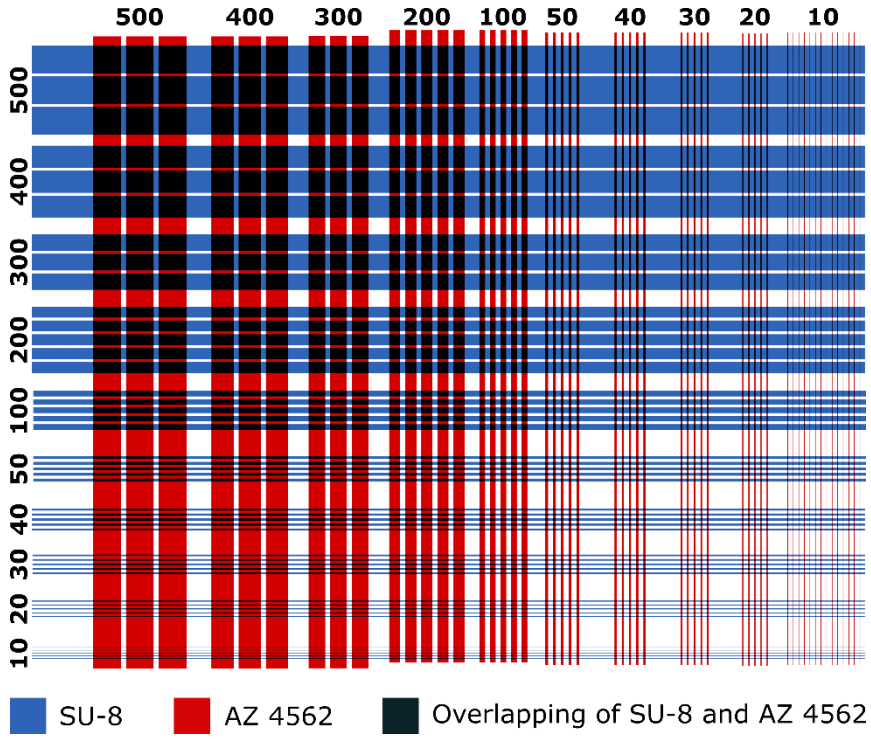

Figure 40: Photomask designs for the fabrication of SU-8 bridges. The numbers represent the width of individual lines within the group (in µm).

Membranes

The membranes are designed as patterned square SU-8 sheets suspended between four anchor points (one on each side), which run along the whole length of the sheet. The sheets contain holes with varying shapes and sizes. Two different types of membranes are to be fabricated based on the shapes of the holes. The first type of membranes have round holes arranged in a 10 x 10 grid. The diameter of the holes ranges from 12.5 to 112.5 µm, in 12.5 µm increments, while the distance between the edges of the holes is equal to their diameter, giving a total membrane length ranging from 237.5 to 2137.5 µm, in 237.5 µm increments.

The second type of membranes contain square holes arranged in a 9 x 9 grid. The length of the holes ranges from 12.5 to 112.5 µm, in 12.5 µm increments, while the distance between the edges of the holes is equal to their length. This gives for a total membrane length ranging from 212.5 µm to 1912.5 µm, in 212.5 µm increments. All holes on individual membranes are of the same size. Figure 41 shows the photomask designs for the fabrication of SU-8 membranes.

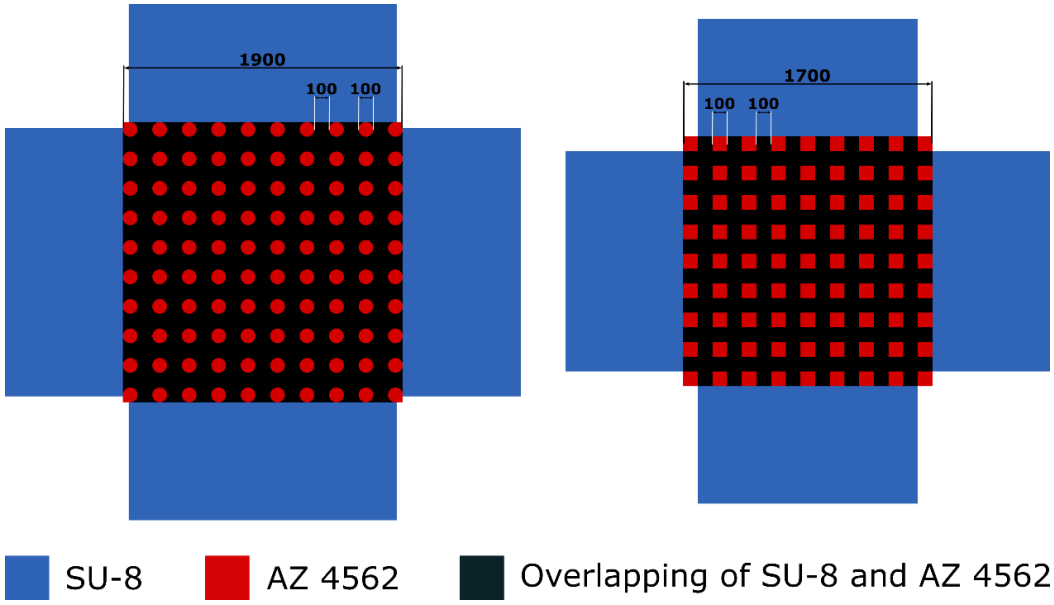

Figure 41: Photomask design for the fabrication of SU-8 membranes with round (left) and square holes (right). The numbers represent the dimensions for membranes with 100 µm wide holes.

Cantilevers

The design of the cantilevers can be divided into three groups. The first group of cantilevers has a length of 100, 250, 500 and 1500 µm, with widths ranging from 10 to 50 µm, in 10 µm increments, and from 100 to 500 µm in 100 µm increments. The second group of cantilevers has an equal length and width, ranging from 10 to 50 µm, in 10 µm increments, and from 100 to 500 µm in 100 µm increments. The third group of cantilevers are randomly sized, with their specific dimensions listed in table 4. The distance between individual cantilevers is 200 µm. Figure 41 shows the photomask designs for the fabrication of SU-8 cantilevers.

Table 4: Dimensions of randomly sized cantilevers in group 3.

No.	Length [µm]	Width [µm]
1	490	10
2	480	20
3	470	30
4	460	40
5	450	50
6	400	100
7	300	200
8	200	300
9	100	400
10	10	500

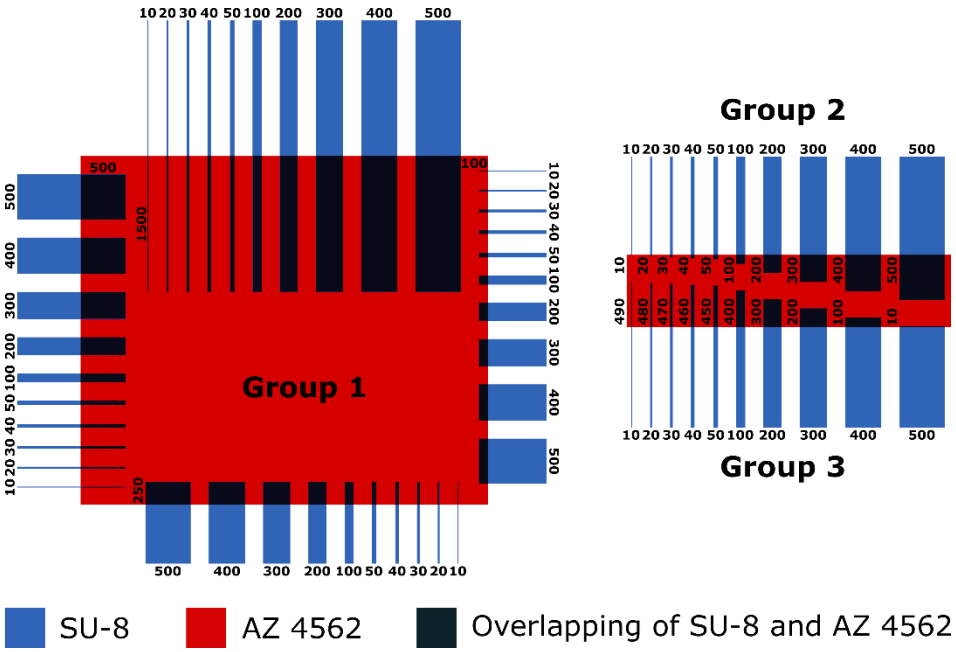

Figure 42: Photomask designs for the fabrication of SU-8 cantilevers. The numbers represent the width and length of individual cantilevers (in µm).

Mushrooms

The design of the mushrooms resembles that of posts with large overhanging tops. Two different types of mushroom are to be fabricated based on their shape; round and square mushrooms. The diameter/length of the mushrooms anchor points range from 12.5 to 112.5 µm, in 12.5 µm increments, while the total diameter/length of the overhangs is 50 % bigger than the size of the anchor points. The round mushrooms are arranged in 10 x 10 grids while the square mushrooms are arranged in 9 x 9 grids. The distance between the overhangs of individual mushrooms within the grid is 50 % smaller than the diameter/length of the anchor points. All mushrooms within an individual grid are of the same size. Figure 43 shows the photomask designs for the fabrication of SU-8 mushrooms.

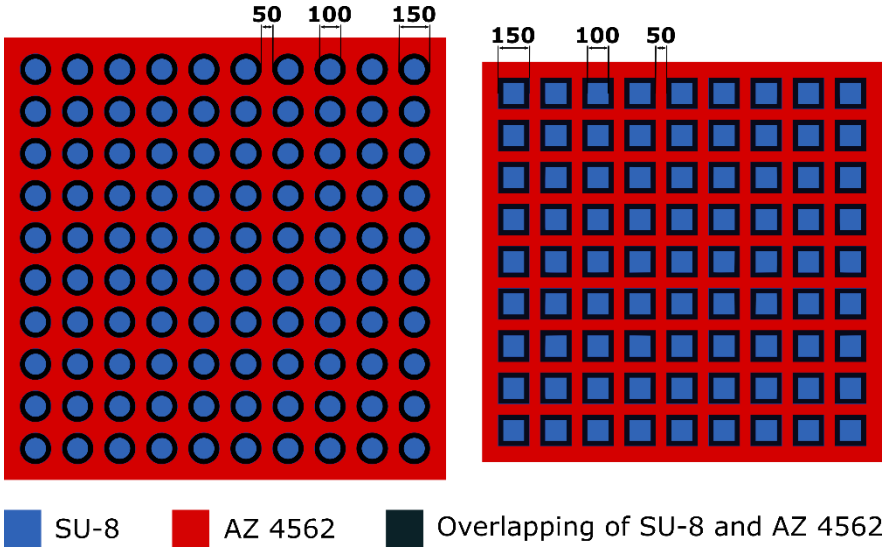

Figure 43: Photomask design for the fabrication of round (left) and square mushrooms (right). The numbers represent the dimensions for mushrooms with 100 µm wide anchor points.

5.1.2 Substrate preparation

Prior to the deposition and processing of the photoresists, the substrates need to be appropriately prepared. For unpatterned SU-8 films, an approximately 300 nm thick layer of either SiO_2 or Si_3N_4 is to be deposited on the surface of a silicon wafer. SiO_2 and Si_3N_4 are electrical insulators and thus allow for the analysis of the electrical resistivity of pyrolytic carbon without interference from the substrate. For suspended SU-8 microstructures, chromium markings are to be fabricated on silicon wafers. These markings serve as alignment markings, for the alignment of the photomasks with the substrate, as well as labels for the suspended microstructures.

The substrates used are standard silicon wafers with a 100 mm diameter and a <100> orientation. First, the wafers are cleaned by dipping them in a buffered oxide etch (BHF) solution for 1 min. The BHF solution contains a 9:1 ratio of ammonium fluoride (NH_4F) and hydrofluoric acid, which removes any native oxides that may have formed on the wafers surface. After dipping the wafers in the BHF solution, the wafers are rinsed with deionized water (DIW) and dried in an 870S Spin Rinse wafer dryer from Semitool. At this point, two wafers are used for the deposition of unpatterned SU-8 films, four for the fabrication of suspended SU-8 microstructures and one for the fabrication of the patterned sacrificial layer.

SiO_2 and Si_3N_4 films

The deposition of the SiO_2 and Si_3N_4 films is performed by means of PECVD with the Plasmalab 80 Plus from Oxford Instruments. The deposition of SiO_2 involves the reaction between SiH_4 and N_2O at 300 °C and 1000 mTorr, with a deposition rate of 63 nm/min. On the other hand, the deposition of Si_3N_4 involves the reaction between SiH_4 and NH_3 at 300 °C and 1000 mTorr, with a deposition rate of 22 nm/min. The deposition of both films was performed by Joonas Heikkinen, Aalto University. After deposition, the wafers are placed in a convection oven for 1 hour at 150 °C, in order to dehydrate the substrate surface.

Chromium markings

The chromium markings are fabricated by first depositing an approximately 200 nm thick layer of chromium on the silicon wafers by means of sputtering with the Plasmalab 400 from Oxford Instruments. Next, the wafers are primed with HMDS in a YES-3 vacuum/vapor priming oven from Yield Engineering Systems. The priming is performed by heating the wafers up to 150 °C and exposing them to HMDS gas for approximately 15 min, after which the wafers are taken out of the oven and left to cool down naturally.

After priming, a thin layer of AZ 5214 E, a positive photoresist provided by Microchemicals GmbH, is deposited on top of the chromium film. This resist is later used as an etching mask for the patterning of the underlying chromium layer. The deposition of the resist is performed by means of spin coating at 4000 rpm for 30 seconds, with an acceleration of 1000 rpm/s. Spin coating is followed by a soft bake on a hotplate at 90 °C for 2 min, after which the wafers are removed from the hotplate and left to cool down naturally. Once the wafers have cooled down to room temperature, the photoresist is ready to be exposed.

Exposure of the resists throughout the fabrication process is carried out with the MA-6 mask aligner from Süss MicroTech SE. The resist is exposed for 3 seconds with 365 nm UV light through a photomask in soft contact (SC) mode. After exposure, the photoresist is developed for 2 to 3 min in a 5:1 solution of DIW and AZ 351B, a photoresist developer provided by Microchemicals GmbH. Next, the wafers are rinsed with DIW, dried with a nitrogen gun and hard baked on a hotplate for 5 min at 120 °C. Once the wafers have cooled down, the chromium layer can be etched.

Etching of the chromium film is carried out by wet etching in a 10:5:85 solution of perchloric acid ($HClO_4$), ammonium cerium(IV) nitrate ($Ce(NH_4)_2(NO_3)_6$) and DIW, for approximately 4 min. Once the chromium layer is fully patterned, the wafers are rinsed with DIW and dried with a nitrogen gun. The final step involves stripping of the remaining photoresist from the patterned chromium film. This is performed by submerging the wafers in an ultrasonic acetone bath for 10 min, followed by rinsing with DIW and drying with a nitrogen gun.

5.1.3 Sacrificial layer

For suspended SU-8 microstructures, the sacrificial layer is fabricated by first priming the wafers containing chromium markings, with HMDS in a vacuum/vapor priming oven at 150 °C for approximately 15 min. After priming, the sacrificial layer can be deposited. The deposition is performed by spin coating the AZ 4562 photoresist on the silicon wafer at 2000 rpm for 30 seconds, with an acceleration of 300 rpm/s. At the end of the spin coating cycle, the wafers are left to sit on the vacuum chuck for 15 min in order to allow the solvent to evaporate from the resist before further processing, as recommended by the photoresist processing data sheet.

Next, the wafers are soft baked on a hotplate. Soft baking is performed by placing the wafers on the hotplate at room temperature, after which the hotplate is ramped up to 90 °C where the wafers are kept for 5 min. Afterwards, the wafers are removed from the hotplate and left to cool down naturally. Once the wafers have cooled down, they are left to sit at room temperature for another 15 min to allow the resist to rehydrate before exposure.

Exposure is performed by first carefully aligning the appropriate photomask with the chromium alignment markings on the wafer. Next, the photoresist is exposed for 30 seconds with 365 nm UV light through the photomask in SC mode. After exposure, the resist is developed in a 5:1 solution of DIW and AZ 351B for 10 to 15 min, rinsed with DIW and dried with a nitrogen gun. The final step involves hard baking of the resist on a hotplate at 120 °C for 10 min, after which the wafers are removed from the hotplate and left to cool down naturally.

The four additional samples that contain only the patterned sacrificial layer are also prepared in the same way as the sacrificial layer used for the fabrication of suspended SU-8 microstructures. However, after development the wafer is cut into quarters with a diamond pen, in order to obtain individual samples. Next, two sample are hard baked with the same parameters as the other sacrificial layers, while the remaining two samples are not. This allows us to analyze the effect of hard baking on the thermal reflow of AZ 4562.

5.1.4 SU-8 processing

Unpatterned SU-8 films

Fabrication of the unpatterned SU-8 films is carried out by first depositing the SU-8 resist on the SiO_2/Si_3N_4 substrate in a two-step spin coating process. First, a spared cycle is performed by accelerating the wafer at 300 rpm/s to 500 rpm, where the wafer is kept for 5 seconds. This is immediately followed by a spin cycle in which the wafer is accelerated with 300 rpm/s to 9000 rpm, where it is kept for 45 seconds. If any air bubbles were to become trapped in the SU-8 during spin coating, the wafer would rest on the vacuum chuck for a couple of minutes, thereby allowing the bubbles to remove themselves from the resist.

Deposition is followed by a two-step soft baking cycle on a hotplate. First, the wafers are heated from room temperature to 65 °C with a heating rate of 21.67 °C/min, where they are kept for 3 min. Next, the wafers are heated to 95 °C with a heating rate of 15 °C/min, where they are kept for 5 min. At the end of the soft bake, the wafers are left on the hotplate and cooled down naturally. The temperature profile of the soft baking cycle can be seen in figure 44 (a). Once the wafers have cooled down to room temperature, the resist can be exposed.

The unpatterned SU-8 films are polymerized by performing a flood exposure of the resist for 8 seconds with 365 nm UV light. After exposure, the wafers are placed on a hotplate for a post-exposure bake. The post-exposure bake is carried out by heating the wafers from room temperature to 95 °C with a heating rate of 19 °C/min, where the wafers are kept for 4 min. This is followed by a controlled cool-down on the hotplate, with a cooling rate of 3.75 °C/min. The temperature profile of the post-exposure baking cycle can be seen in figure 44 (b). Once the wafers have cooled down they are cut into quarters with a diamond pen, in order to obtain individual samples.

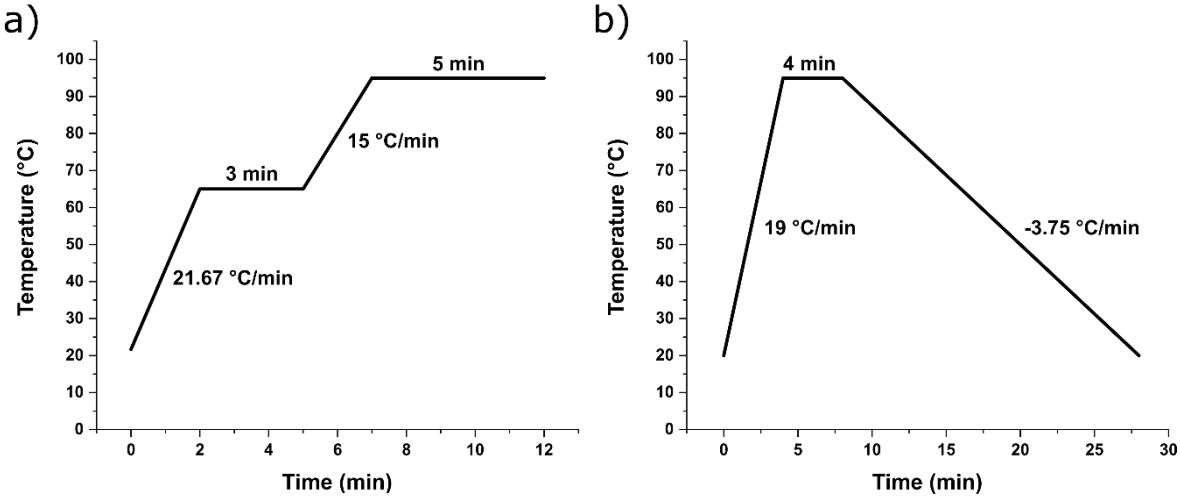

Figure 44: Temperature profiles for (a) the soft baking cycle and (b) the post-exposure baking cycle of SU-8.

Suspended SU-8 microstructures

The suspended SU-8 microstructures are fabricated by first dipping the silicon wafers with the patterned sacrificial layers in a 10:1 solution of DIW and HF for 1 min, in order to remove any newly formed native oxides from the substrate surface. Afterwards, the wafers are rinsed

with DIW and dried with a nitrogen gun. Next, the SU-8 is deposited on the substrate by means of spin coating, followed by a soft baking cycle on a hotplate. The parameters used for the spin coating and soft baking of SU-8 are the same as with the unpatterned SU-8 films.

Exposure of the SU-8 is performed by first carefully aligning the appropriate photomask with the chromium alignment markings on the wafer. Next, the resist is exposed for 8 seconds with 365 nm UV light through the photomask in SC mode. After exposure, the wafers are placed on a hotplate for a post-exposure bake. The parameters used for the post-exposure bake are the same as with the unpatterned SU-8 films. Once the wafers have cooled down to room temperature, the resist is ready to be developed.

The development of SU-8 is carried out by submerging the wafers in PGMEA for a minimum period of 6 hours. PGMEA does not only dissolve the unexposed SU-8 but also removes the sacrificial layer in the process. While the unexposed SU-8 is removed within the matter of minutes, the removal of the sacrificial layer takes several hours. Fortunately, this does not damage the polymerized SU-8, thereby allowing for the samples to be left immersed in the developer overnight.

Once the sacrificial layer is completely removed from the substrate, the wafers are carefully taken out of the developer. Next, the wafers are gently rinsed with isopropanol and dried with a nitrogen gun. Both of these steps must be performed very cautiously so as to not bend, break or remove any of the suspended SU-8 microstructures from the substrate. After drying, the wafers are cut into quarters with a diamond pen, to obtain individual samples, and left to sit at room temperature for 24 hours, in order to completely dry-off before further processing.

5.1.5 Pyrolysis

Pyrolysis of the samples is carried out at four different pyrolysis temperatures; 800, 900, 1000 and 1100 °C. Three samples with suspended SU-8 microstructures and chromium markings, as well as two samples with unpatterned SU-8 films, one deposited on a SiO_2 substrate and one deposited on a Si_3N_4 substrate, are pyrolyzed at the same temperature.

The pyrolysis is carried out in a RS 80/500/11 tube furnace from Nabertherm GmbH, under a nitrogen atmosphere. First, the samples are loaded into alumina boats and pushed to the center of the furnace. Next, both ends of the tube are closed off and the air is pumped out of the furnace with a vacuum pump. Once the pressure inside the tube falls below 10^{-4} mbar, the vacuum pump is turned off and a flow on nitrogen is slowly introduced into the furnace from one end of the tube. When the pressure inside the tube reaches 2 bar, the nitrogen flow is turned off and the furnace is vacuumed out again. This process is then repeated two more times in order to completely remove any traces of oxygen from the furnace. After the nitrogen is reintroduced into the furnace for the third time, the nitrogen flow is left open while the opposite end of the tube is opened up, thus establishing a steady flow of nitrogen between the two ends of the tube. The nitrogen flow is estimated to be approximately 2000 ml/min, which is determined based on the size and rate of nitrogen bubbles that are released from the furnace into a glass beaker filled with water. Figure 45 (a) shows a schematic presentation of the tube furnace.

Pyrolysis of SU-8 is performed in a two-step process. First, the samples are heated from room temperature up to 300 °C with a heating rate of 200 °C/h, were they were kept for a period of 40 min. Next, the samples are heated to their final pyrolysis temperature with a heating rate of 200 °C/h, where they were kept for a period of 1 hour. After pyrolysis, the samples are left in the furnace and cooled down naturally, which takes approximately 8 hours. Figure 45 (b) shows the temperature profile for samples pyrolyzed at 900 °C.

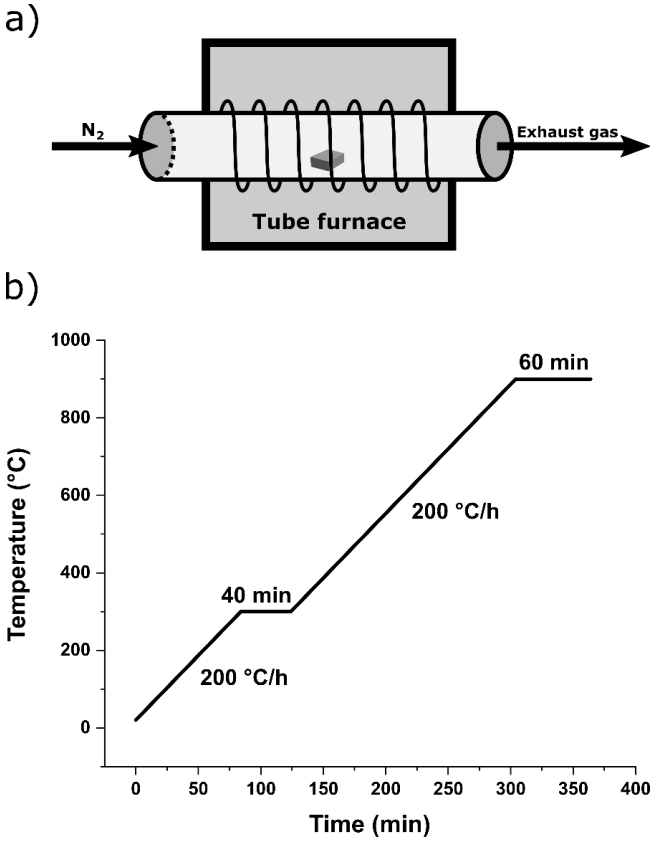

Figure 45: (a) Schematic presentation of the pyrolysis furnace. (b) Temperature profile for samples pyrolyzed at 900 °C.

5.2 Sample characterization

The suspended SU-8 and pyrolytic carbon microstructures are characterized in terms of their structural stability and reproducibility, as well as their level of shrinkage during pyrolysis. The analysis is performed with an optical microscope, SEM and profilometer. On the other hand, the unpatterned pyrolytic carbon films are characterized in terms of their electrical resistivity, crystallinity and surface roughness. The analysis is performed with a four-point probe, Raman spectrometer and atomic force microscope (AFM), respectively.

Optical microscopy and scanning electron microscopy

An optical microscope with a camera is used to analyze the stability and reproducibility of the suspended SU-8 and pyrolytic carbon microstructures. All structures on the 16 samples are analyzed, during which notes are taken on any fabrication issues and inconsistencies that are observed between the samples. The obtained data is then used to corelate the specific

fabrication issues to the shape, size and pyrolysis temperature of the microstructures, as well as to identify a potential reason as to why certain fabrication issues occur and how they can be avoided in the future.

The SUPRA 40 SEM from Zeiss is used to obtain detailed images of the suspended microstructures. Images are taken of one sample pyrolyzed at 900 °C and one reference sample. The reference sample is coated with an approximately 20 nm layer of chromium beforehand, by means of sputtering, in order to increase its conductivity.

Additionally, the SEM is also used to obtain detailed images of the patterned sacrificial layer. Images are taken of two samples, one sample that has undergone hard baking and one sample that has not. Both samples are coated with a 20 nm layer of chromium beforehand, by means of sputtering, in order to increase their conductivity.

Profilometer

The vertical and lateral contraction of SU-8 is analyzed by measuring the topographical profiles of selected microstructures with the Dektak/XT profilometer from Bruker. The analysis is carried out on eight pyrolyzed samples, two for each pyrolysis temperature, and two reference samples. Measurements are performed on the anchor points of 500 µm wide bridges, membranes with 100 µm wide round holes and 500 µm wide cantilevers, at least 0.5 mm away from the suspended structure. The measurements obtained for each pyrolysis temperature are then averaged out. The lateral contraction is measured from the top of the structures.

The profilometer is also used to analyze the size of the sacrificial layer. The analysis is carried out on two samples that contain the patterned sacrificial layer, one sample that has undergone hard baking and one sample that has not. Measurements are performed on the patterns used for the fabrication of 500 µm long bridges, membranes with 100 µm wide round holes and mushrooms with 75 µm wide round anchor points.

Four-point probe

The electrical resistivity of the unpatterned pyrolytic carbon films is analyzed by first measuring the electrical resistance (R) of the films with the MCP-T400 four-point probe from Loresta AP. Five measurements are performed at random locations on each of the eight sample, at least 2 cm away from the samples edge. The resistivity (ρ) is then calculated according to equations 8 and 9;

$$R_s = R \cdot \frac{W}{L} \tag{8}$$

$$\rho = R_s \cdot h \tag{9}$$

First, the sheet resistance (R_s) of pyrolytic carbon is calculated by combining the measured resistance with the width (W) and (L) length of the sample (for a round wafer; W/L = 4.532). From here, the resistivity is calculated by combining the sheet resistance with the thickness (h) of pyrolytic carbon obtained from the profilometer measurements.

Raman spectroscopy

The crystallinity of the unpatterned pyrolytic carbon films is analyzed by means of Raman spectroscopy with the Alpha300 RA micro-Raman spectrometer from WITec. The Raman spectra are obtained by conducting three line scans at random locations on each of the eight sample, at least 2 cm away from the samples edge. The parameters used in the measurements are summarized in table 5.

Table 5: Parameters used in the Raman spectroscopy measurements.

Parameter	**Value**
Laser excitation wavelength (λ)	532 nm
Laser power	~1 mW
Line scan length	200 µm
Points per line	50
Accumulations per point	10
Integration time of accumulation	0.5 s

Analysis of the Raman spectra is carried out with Origin Pro. First, the spectra obtained from each individual line scan are averaged out. Next, the G, D and 2D peaks are fitted with Lorentzian curves, upon which the intensities, position and FWHM of the peaks are analyzed. Based on these parameters, a determination can be made on the crystallinity and amorphization trajectory of pyrolytic carbon in relation to the pyrolysis temperature. The size of the crystallites is also calculated in accordance with equation 6.

Atomic force microscopy

The surface roughness of SU-8 and pyrolytic carbon films is analyzed with the Dimension 3100 AFM from DI. Three measurements are performed at random locations on each of the eight sample, at least 2 cm away from the samples edge, before and after pyrolysis. The surface roughness is analyzed for a 5 x 5 µm area, with the AFM operating in tapping mode.

6. Results and discussion

6.1 Visual inspection of pyrolytic carbon

After pyrolysis, the pyrolytic carbon appears very brittle with a black, highly glossy and very smooth surface finish. Upon initial inspection, the pyrolytic carbon fabricated on the Si and SiO_2 substrates show no issues. On the other hand, the pyrolytic carbon fabricated on the Si_3N_4 substrate experiences severe cracking and delamination in an approximately 5 mm wide area around the wafers edge.

Cracking of the pyrolytic carbon can be attributed to the hydrophilic nature of Si_3N_4, which pulls the SU-8 together immediately after deposition, starting from the edge of the wafer. As a result, the resist forms an edge bead which is very poorly adhered to the substrate. The formation of intrinsic stress during pyrolysis causes the edge bead to crack and delaminate from the substrate. This effect occurred for all pyrolytic carbon samples fabricated on the Si_3N_4 substrate, regardless of the pyrolysis temperature. Figure 46 shows the difference between unpatterned pyrolytic carbon films fabricated on the SiO_2 and Si_3N_4 substrate.

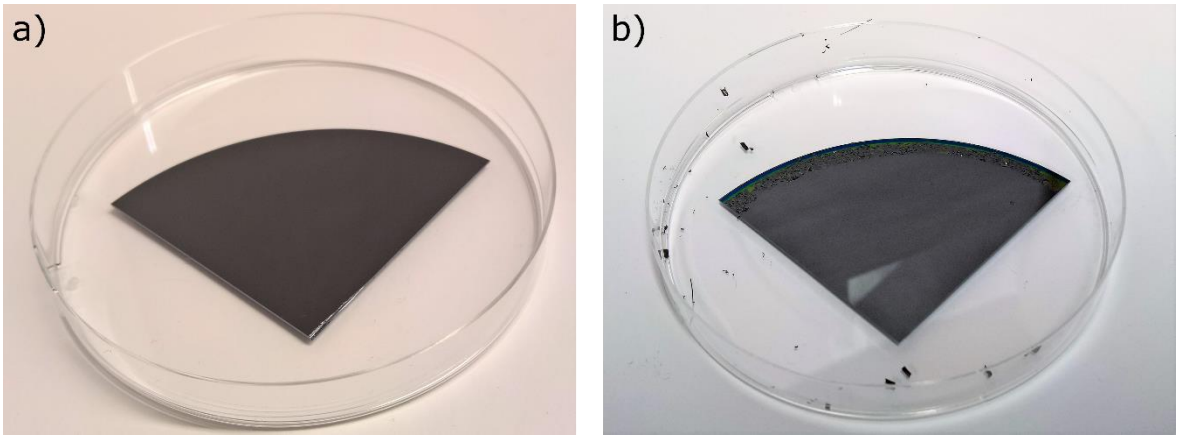

Figure 46: Unpatterned pyrolytic carbon films fabricated on the (a) SiO_2 and (b) Si_3N_4 substrate. The pyrolytic carbon fabricated on the Si_3N_4 substrate shows significant cracking and delamination around the wafers edge due to a poorly adhered edge bead.

6.2 Suspended pyrolytic carbon microstructures

6.2.1 Sacrificial layer

Often times, C-MEMS devices require the fabrication of microstructures with very high dimensional accuracies. For suspended microstructures, high dimensional accuracies are not only dependent on the processing parameters of SU-8 but also on the fabrication process related to the sacrificial layer. In our study, three effects related to the sacrificial layer were observed to have a direct influence on the shape and dimensions of the suspended microstructures. These include; the thermal reflow of AZ 4562, the formation of gaps between SU-8 and the substrate, as well as the dissolution of the sacrificial layer.

Thermal reflow of the sacrificial layer

Prior to hard baking, the sacrificial layer structures possess a rectangular shape with slightly positively sloped sidewalls, as seen in figure 47 (a and c). Hard baking at 120 °C causes the AZ 4562 resist to undergo a thermal reflow which leads to the rounding of the sacrificial layer, as seen in figure 47 (b and d). As a result, the average width of the measured structures was reduced by approximately 12 µm, from the base of the structure, while the average height was increased from approximately 10 µm to 11 µm.

The rounding of the sacrificial layer causes the suspended SU-8 microstructures to obtain an arch shaped profile. The arched profiles would later be leveled out during pyrolysis due to the shrinking of the material. The initial dimensions of the sacrificial layer could potentially be preserved by lowering the hard baking temperature below the glass transition temperature of AZ 4562 at 110 °C [97]. Another method of preserving the shape of the sacrificial layer is through UV curing which hardens the resist and renders it stable at temperatures of up to 280 °C [98].

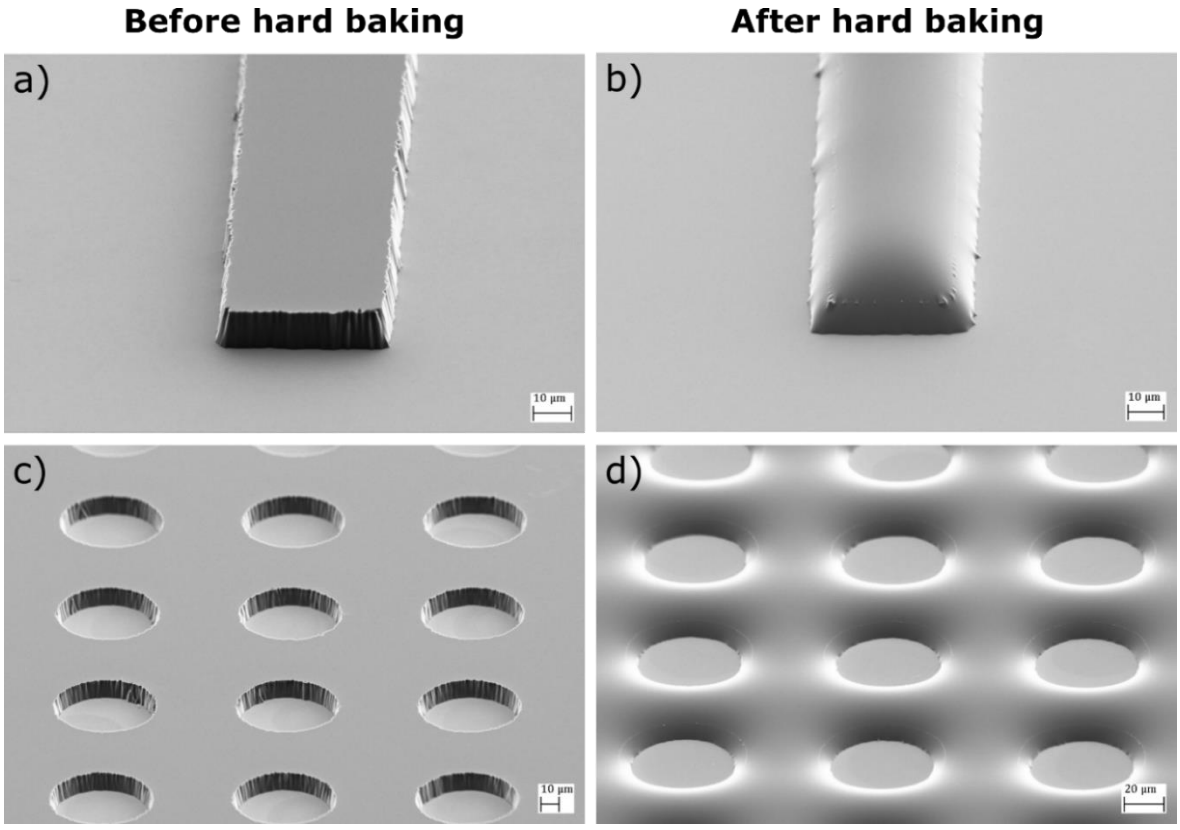

Figure 47: SEM images of the sacrificial layer used for the fabrication of (a, b) 50 µm long SU-8 bridges and (c, d) SU-8 mushrooms with 50 µm wide round anchor point, before and after hard baking. Hard baking causes the rounding of the AZ 4562 resist which leads to a change in the shape and dimension of the sacrificial layer.

Gap formation between SU-8 and the substrate

Another effect that was noted is the formation of gaps between SU-8 and substrate, as seen in figure 48. These gaps were observed next to the base of the sacrificial layer, only on the side that is facing away from the direction in which SU-8 spreads during spin coating. This prevents the anchor points from fully attaching themselves to the substrate, thus increasing

the size of the suspended structures. The effect is amplified by pyrolysis where the suspended structures are able to pull themselves further back due to the shrinking of the resist.

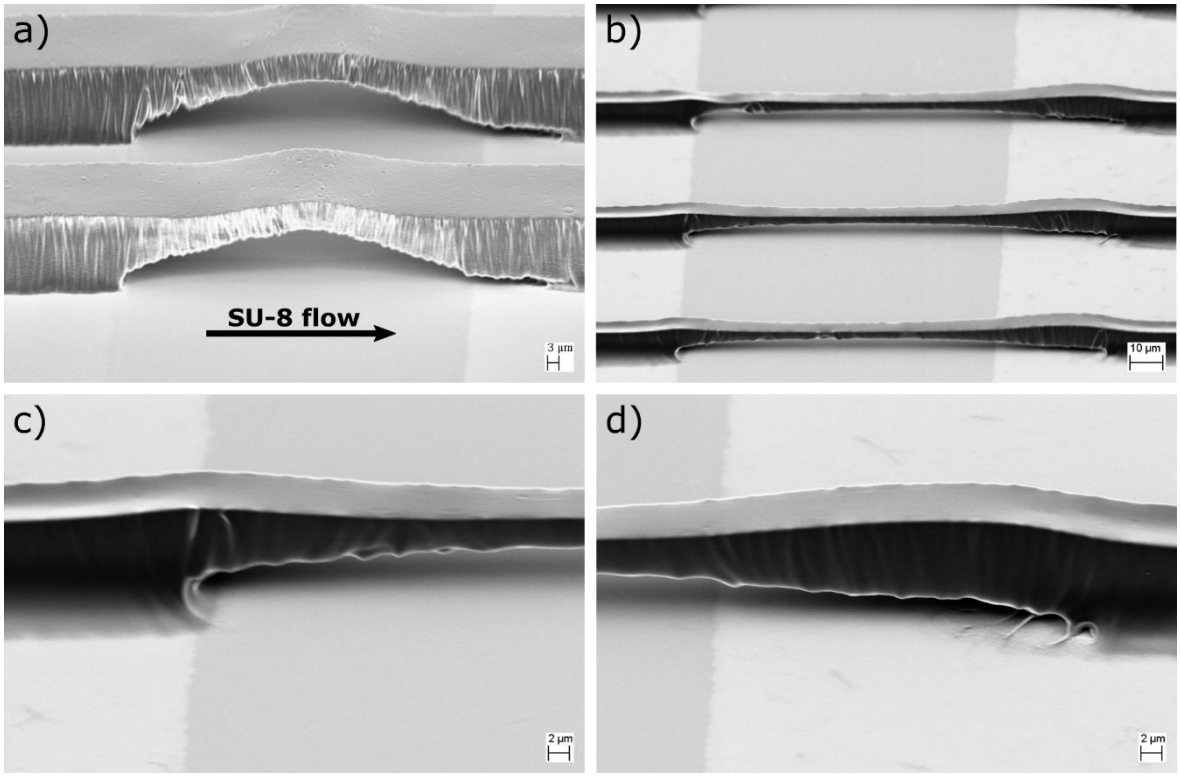

Figure 48: SEM images of gaps formed between the SU-8 and the substrate. (a) and (b) show SU-8 bridges before and after pyrolysis, respectively, with the darker shade on the substrate indicating the former location of the sacrificial layer. The gaps are significantly increased during pyrolysis, due to the shrinking of SU-8. (c) and (d) show close-up images of the pyrolytic carbon bridge, indicating that the side of the sacrificial layer that is facing towards the direction of the SU-8 flow will be fully enveloped by the SU-8, while the side facing away from the direction of the SU-8 flow will form a significant gap with the substrate.

A possible explanation for this effect is that the high flow rate of SU-8, during spin coating, causes the resist to form an arch shaped flow over the side of the sacrificial layer that faces away from the direction in which the SU-8 spreads. This, in turn, leads to air getting trapped between the substrate and SU-8, around the base of the sacrificial layer. Due to the high viscosity of SU-8 the air cannot escape, thus resulting in gaps between the anchor points and substrate. Figure 49 shows a schematic presentation on the formation of such gaps.

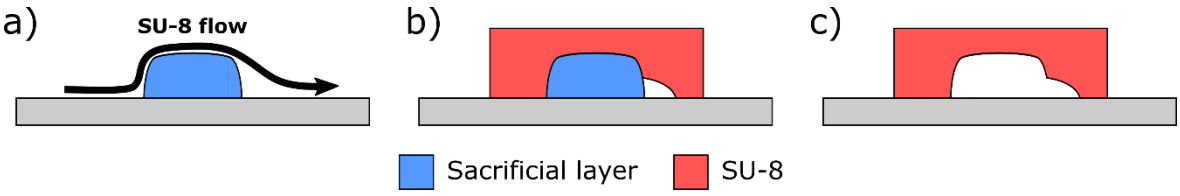

Figure 49: Schematic presentation on the formation of gaps between the substrate and SU-8. (a) The high flow rate of SU-8 during spin coating causes the resist to form an arch shaped flow over the side of the sacrificial layer. (b) As a result, this leads to air getting trapped between the substrate and SU-8, which (c) increases the size of the suspended structure.

After pyrolysis, the width of the gaps ranged between approximately 3 and 30 µm. The size of the sacrificial layer appeared to have no direct effect on the gap size, as large gaps were observed with both smaller and bigger sacrificial layers. However, the gaps do appear to be

bigger when the sacrificial layers are positioned at a higher angle to the direction of the SU-8 flow. This leads us to believe that the gaps could potentially be eliminated by positioning the sacrificial layers, for structures such as bridges and cantilevers, parallel the direction of the SU-8 flow. Another way of reducing these gaps would be to lower the spinning speed and use SU-8 resists with lower viscosities. That way, the SU-8 would form a smaller arch over the side of the sacrificial layer, while the trapped air would be able to escape the resist.

Dissolution of the sacrificial layer

SEM images of the suspended microstructures indicate that the SU-8 would readily attack the AZ 4562 resist immediately upon deposition. As a result, this leads to either a partial or a complete dissolution of the sacrificial layer in SU-8.

In a partial dissolution, the SU-8 dissolves only the upper portion of the sacrificial layer. As a result, this would cause the formation of undulations and protrusions on the underside of the suspended SU-8 microstructures which, in turn, significantly increases the structures surface roughness. The suspended SU-8 structures would then retain this surface even after pyrolysis. This effect may not be entirely undesirable as a higher surface roughness increases the effective surface area of the material, improving its performance in devices such as electrochemical sensors, cell-based sensors and energy storage systems. A partial dissolution of the sacrificial layer was observed for all AZ 4562 patterns. Figure 50 shows the surface on the underside of a suspended pyrolytic carbon microstructure.

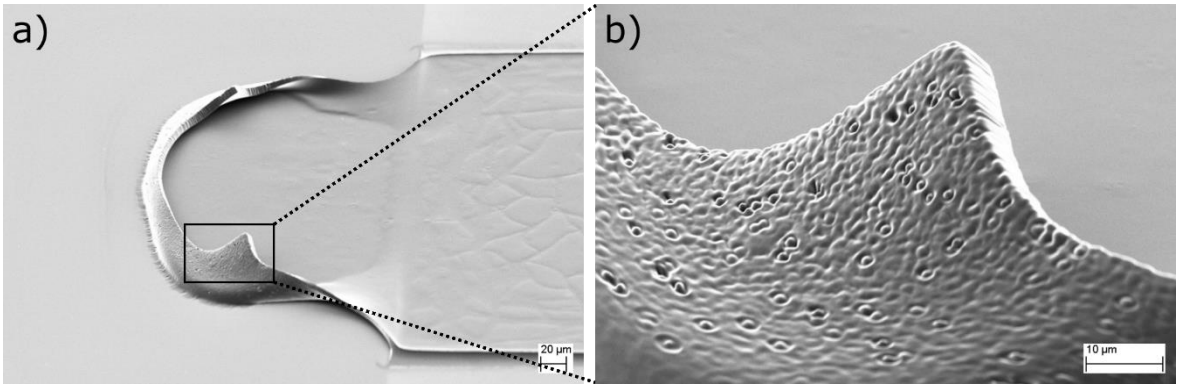

Figure 50: SEM images of the surface on the underside of a suspended pyrolytic carbon structure. The images show undulations and protrusions which are not present on the top of the structure.

In a complete dissolution, the SU-8 attacks the sacrificial layer to the point where the two resists completely diffuse into one other. As a result, the sacrificial layer can no longer be removed and the suspended structure cannot be fabricated. This effect was observed only for sacrificial layers used for the fabrication of 10 µm long SU-8 bridges, as their small size would allow for SU-8 to completely dissolve the AZ 4562 resist. Furthermore, the issue was present only when the wafer was left to sit on the spinner for several minutes after deposition, as the SU-8 would have more time to dissolve the sacrificial layer before soft baking. The dissolution of the AZ 4562 can potentially be prevented by either sputtering a thin inorganic film (e. g. Cu, Ti, SiO_2) on top of the sacrificial layer prior to the deposition of SU-8, thereby effectively separating the two resists [90], or by hardening the resist through UV curing.

6.2.2 Bridges

Figure 51 shows SEM images of successfully fabricated SU-8 bridges before and after pyrolysis. Before pyrolysis, longer bridges possess a relatively straight profile, while shorter bridges show a distinctive arch due to a more notable rounding of the sacrificial layer.

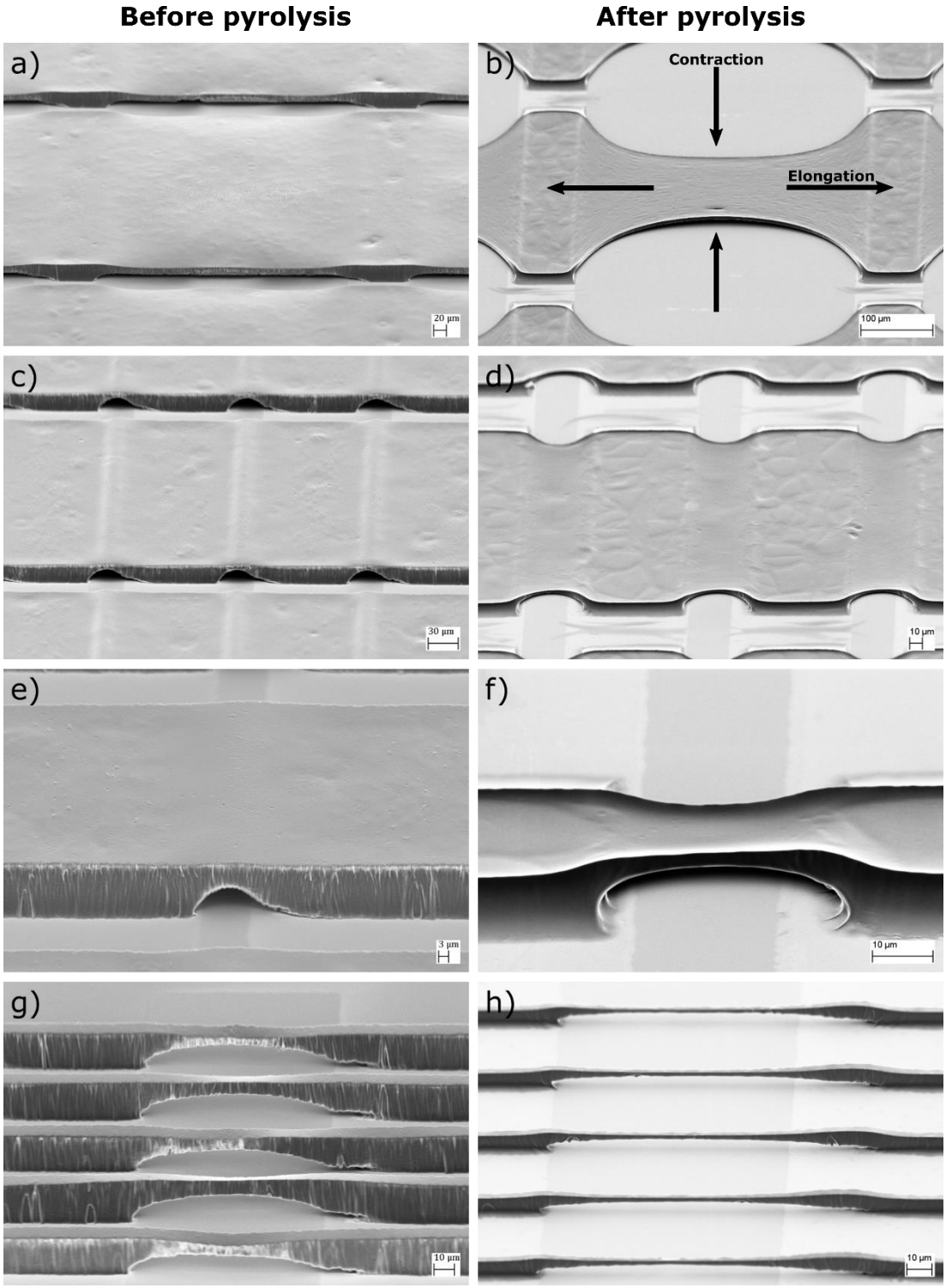

Figure 51: SEM images of successfully fabricated SU-8 bridges with varying sizes, before and after pyrolysis (length x width before pyrolysis); (a, b) 400 x 500 µm, (c, d) 40 x 300 µm, (e, f) 30 x 50 µm and (g, h) 100 x 10 µm. The level of lateral shrinking during pyrolysis depends on the initial width of the bridge, with wider bridges experiencing a more significant contraction. Because the lateral contraction is much more restricted at the anchor points than in the center of the bridge, this causes the bridges to obtain curved sides.

During pyrolysis, the bridges experience a lateral contraction perpendicular to the anchor points and a lateral elongation towards the anchor points. The lateral contraction is more significant with wider bridges, due to their larger surface area. On the other hand, stretching of the bridges is caused by the lateral contraction of the anchor points and leads to the formation of tensile stress in the structure.

While the majority of pyrolytic carbon bridges were successfully fabricated on all samples, a number of bridges would experience consistent fabrication issues, as presented in figure 52. These issues can be categorized based on the size of the bridges and include; the collapse of the bridges, buckling of bridges, complete dissolution of the sacrificial layer and cracking of the bridges.

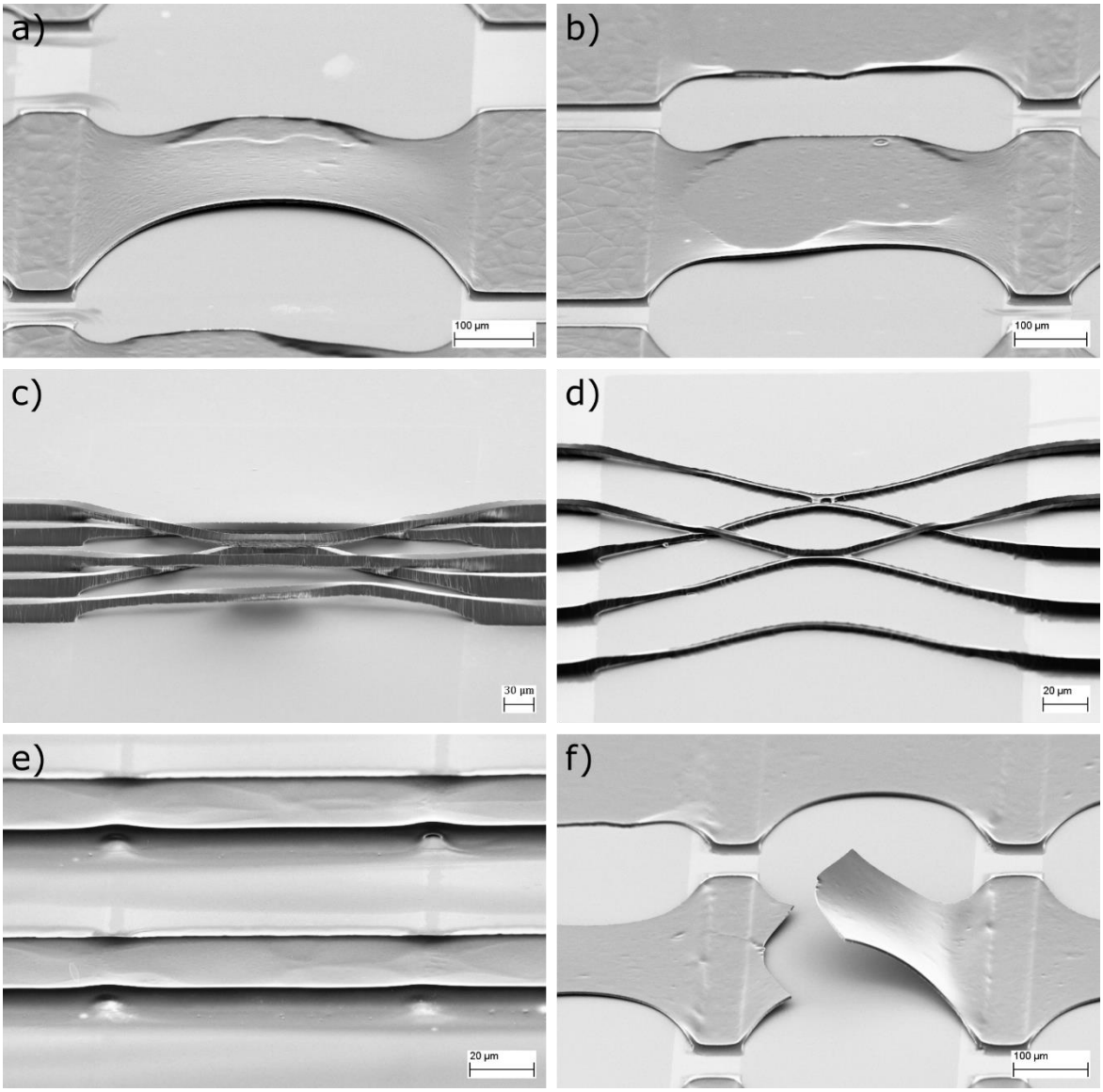

Figure 52: SEM images of unsuccessfully fabricated pyrolytic carbon bridges. Long wide bridges would often collapse and either (a) partially or (b) fully attach themselves to the substrate. Long narrow bridges would often buckle. This was caused by either (c) improper processing of the sample after the development of SU-8 or (d) due to the uneven distribution of stress during pyrolysis. (e) For 10 µm long bridges, the SU-8 would often completely dissolve the sacrificial. (f) The random cracking of bridges was also observed. The size of bridges represented in the images are (length x width, before pyrolysis); (a, b) 500 x 500 µm, (c) 200 x 10 µm, (e) 10 x 50 µm and (f) 300 x 500 µm.

Collapse of bridges

The first fabrication issue that was observed is the partial or complete collapse of long and wide pyrolytic carbon bridges, as seen in figure 52 (a and b). This effect can be attributed to the relaxation of residual stress and the thermal expansion of SU-8 during the initial stages of pyrolysis, as well as the bridges own weight. All of these factors would cause the bridge to bend and deflect towards the substrate. If the deflection was severe enough for the bridge to come into contact with the substrates surface, the suspended structure would remain attached to the substrate throughout the pyrolysis process due to stiction forces. The issue was commonly observed for bridges with lengths of over 300 µm and widths of over 50 µm.

The relaxation of stress and thermal expansion of SU-8 would cause the bridges to either twist or uniformly deflect downwards. Twisting would cause the bridge to partially collapse and attach itself to the substrate from one side, as seen in figure 52 (a). This phenomenon is most likely the result of an uneven distribution of stress across the width of the bridge, which causes one side of the bridge to bend further down than the other. On the other hand, a more even distribution of stress would cause the bridge to deflect uniformly and fully attach itself to the substrate, as seen in figure 52 (b).

Whether or not the bridges would deflect significantly enough to come into contact with the substrate appeared to be completely random, as bridges of the same size showed different degrees of deflection. However, the issue was more common with larger bridges as the greater length and increased weight would allow for a higher degree of bending. The issue was observed with approximately 50 % of bridges with a length and width of 500 µm and was reduced to less than 20 % for bridges with a length of 300 µm and a width of 200 µm. Bridges shorter than 200 µm did not experience this issue as their good structural stability would restrict them from deflecting significantly enough to reach the substrate.

The fact that the bridges are able to bend without cracking indicates that this issue occurs in the initial stages of pyrolysis where the SU-8 still has a significant amount of flexibility [9], [30]. A potential solution to this problem would be to fabricate taller anchor points so that bridges come into contact with the substrate. The pyrolysis temperature had no effect on the issue.

Buckling of bridges

The second fabrication issue is the buckling of long narrow bridges. This effect was observed for bridges with lengths of over 100 µm and widths below 50 µm, as the poor structural stability of narrow bridges would allow them to bend laterally. The wider the bridge the longer it had to be to exhibit this effect, as a greater width increases the structural stability of the bridge while a greater length reduces it.

Buckling of the bridges can be attributed to two factors. The first factor is the improper processing of the wafer after the development of SU-8, where a combination of aggressive or inadequate rinsing, as well as aggressive drying would lead to the twisting and buckling of bridges, as seen in figure 52 (c). Inadequate rinsing of the samples with isopropanol would typically result in larger amounts of PGMEA to remain on the sample after development.

The strong capillary forces of PGMEA would than act upon the sidewalls of the SU-8 microstructures during drying, which would cause the narrow bridges to twist, buckle and pull together. The issue could then be further amplified by aggressive rinsing and drying of the samples with nitrogen, which would cause the bridges to bend even further. After drying, the bridges would remain stuck together due to the stiction forces. A similar issue was also reported by Wang *et al*. [3] who noted the collapse of HAR SU-8 pillars due to the capillary forces of PGMEA acting upon the sidewalls of the microstructures.

The second factor can be attributed to the uneven distribution of stress in the bridge during the initial stages of pyrolysis, as noted also with wider pyrolytic carbon bridges. However, the weaker structural stability of narrow bridges would result in a combination of twisting and buckling of the bridges, as opposed to wider bridges which would only twist. This would lead to the bridges either attaching themselves to one another (while still remaining suspended above the substrate), attaching themselves to the substrate, or a combination of both, as seen in figure 52 (d). The effect appeared to be completely random, although narrower and longer bridges were more prone to buckling due to their weaker structural stability.

Similar results were also reported by Kurek *et al.* [12] who noted the buckling of SU-8 bridges before and after pyrolysis. In our study, the buckling of bridges with a length of 500 µm and a width of 10 µm was observed in more than 70 % of cases. The issue was reduced below 25 % for 100 µm long and 10 µm wide bridges due to a better structural stability.

Complete dissolution of the sacrificial layer

The third fabrication issue is the complete dissolution of the sacrificial layer by SU-8, as seen in figure 52 (e). This issue was noted with 10 µm long bridges and is further discussed in section 6.2.1. In our study, a complete dissolution of the sacrificial layer was observed in approximately 30 % of 10 µm long bridges.

Cracking of bridges

Another fabrication issue that was observed is the cracking of pyrolytic carbon bridges. This issue can be attributed to the buildup of tensile stress in the structure during the later stages of pyrolysis, which would on rare occasions cause the bridges to crack and detach from their anchor points. If a bridge were to completely break off from one of its anchor points, this would cause the bridge to deflect upwards, as seen in figure 52 (f).

Similar results were also noted by Lim *et al.* [9] who attributed the upward deflection of pyrolytic carbon wires to the non-uniform lateral contraction of the anchor points during pyrolysis. The non-uniform contraction of the anchor points is caused by the strong adhesion of SU-8 to the substrate, which restricts the lateral shrinking of the anchor points around its base while allowing the resist to shrink freely further away from the substrate. The differences in the lateral shrinking of the anchor points at different heights leads to greater stretching of the bridges at the top than at the bottom, thus forming a transverse stress gradient throughout the height of the structure which causes the bridge to deflect upwards.

Compared to other fabrication issues, the cracking of bridges was not related to their size and would occur completely randomly, regardless of the bridge's length and width. On the other hand, the pyrolysis temperature did appear to have an effect on the issue. Higher temperatures would typically lead to a slightly higher number of cracked bridges, as the greater contraction of the resist would cause higher levels of stress in the structure. Overall, less than 1 % of all bridges would experience cracking. The fabrication issues of pyrolytic carbon bridges are schematically depicted in figure 53 and summarized in table 6.

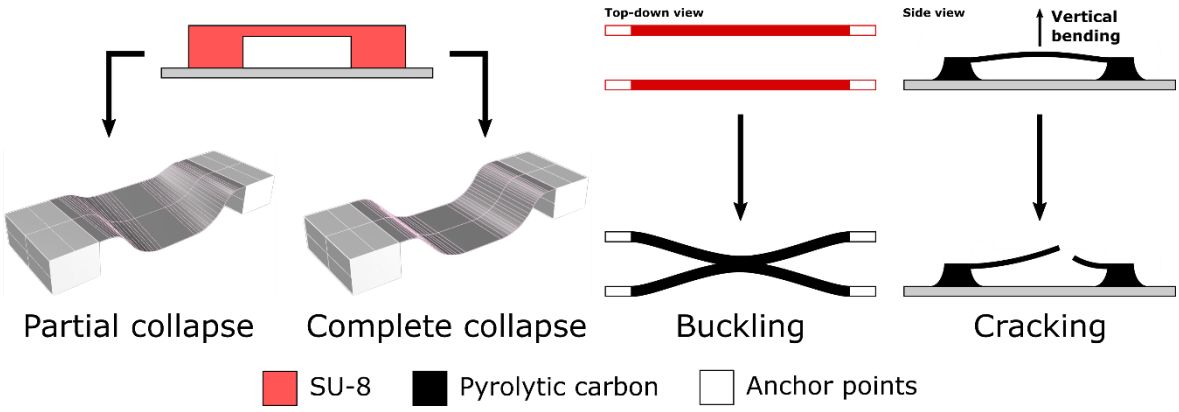

Figure 53: Schematic presentation of the fabrication issues for pyrolytic carbon bridges.

Table 6: Fabrication issues of pyrolytic carbon bridges in relation to their size.

Width [µm] \ Length [µm]	500	400	300	200	100	50	40	30	20	10
500	▼	▼	▼							●
400	▼	▼	▼							●
300	▼	▼	▼							●
200	▼	▼	▼							●
100	▼	▼								●
50	◇ ▼									●
40	◇	◇								●
30	◇	◇	◇							●
20	◇	◇	◇	◇						●
10	◇	◇	◇	◇	◇					●

▼ Collapse ◇ Buckling ● Complete dissolution of the sacrificial layer

Before pyrolysis | Before and during pyrolysis | During pyrolysis | No issues

6.2.3 Membranes

Figure 54 shows SEM images of successfully fabricated SU-8 membranes before and after pyrolysis. Before pyrolysis, the membranes possess a relatively flat profile, with bigger membranes showing a slight negative deflection due to the weight of the structure. During pyrolysis, the lateral contraction of the anchor points causes the membranes to stretch in all directions and increase their overall size. At the same time, the membranes holes increase in size due to the internal contraction of the membranes.

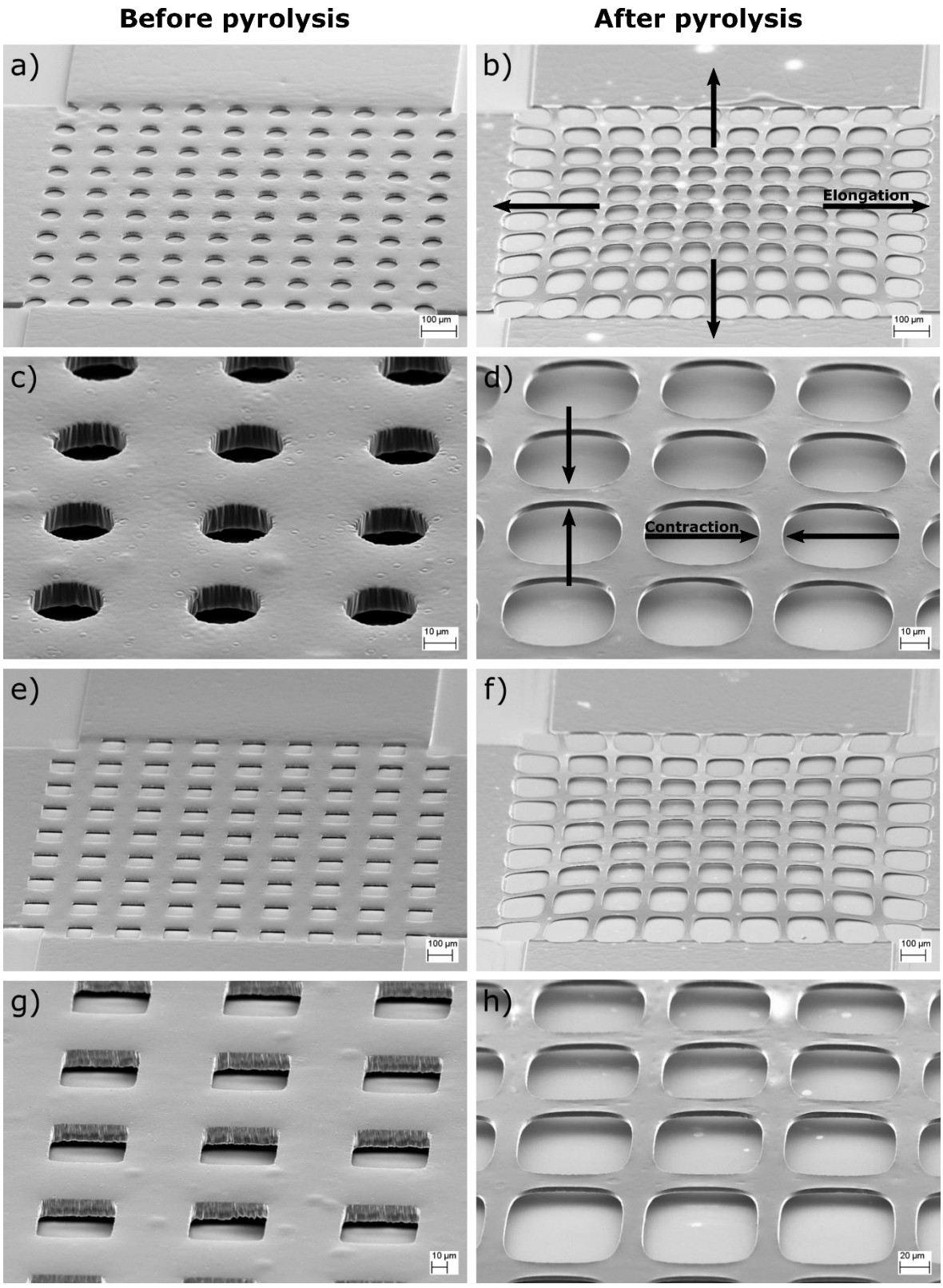

Figure 54: SEM images of successfully fabricated SU-8 membranes with varying shapes and sizes of the membrane holes, before and after pyrolysis (diameter/length of holes before pyrolysis); (a, b) 62.5 µm round holes, (c, d) 25 µm round holes, (e, f) 100 µm square holes and (g, h) 50 µm square holes. After pyrolysis, the membranes exhibit a slight positive deflection due to the uneven lateral contraction of the anchor points, which causes stress gradients throughout the height of the structure. The lateral elongation of the membranes also appears to be more extensive around the edges of the membrane than in the center, as indicated by the deformed shape of the holes.

Prior to pyrolysis, all SU-8 membranes were successfully fabricated on all samples. During pyrolysis, a number of membranes would experience various fabrication issues, as presented in figure 55. These issues include the collapse and cracking of the membranes.

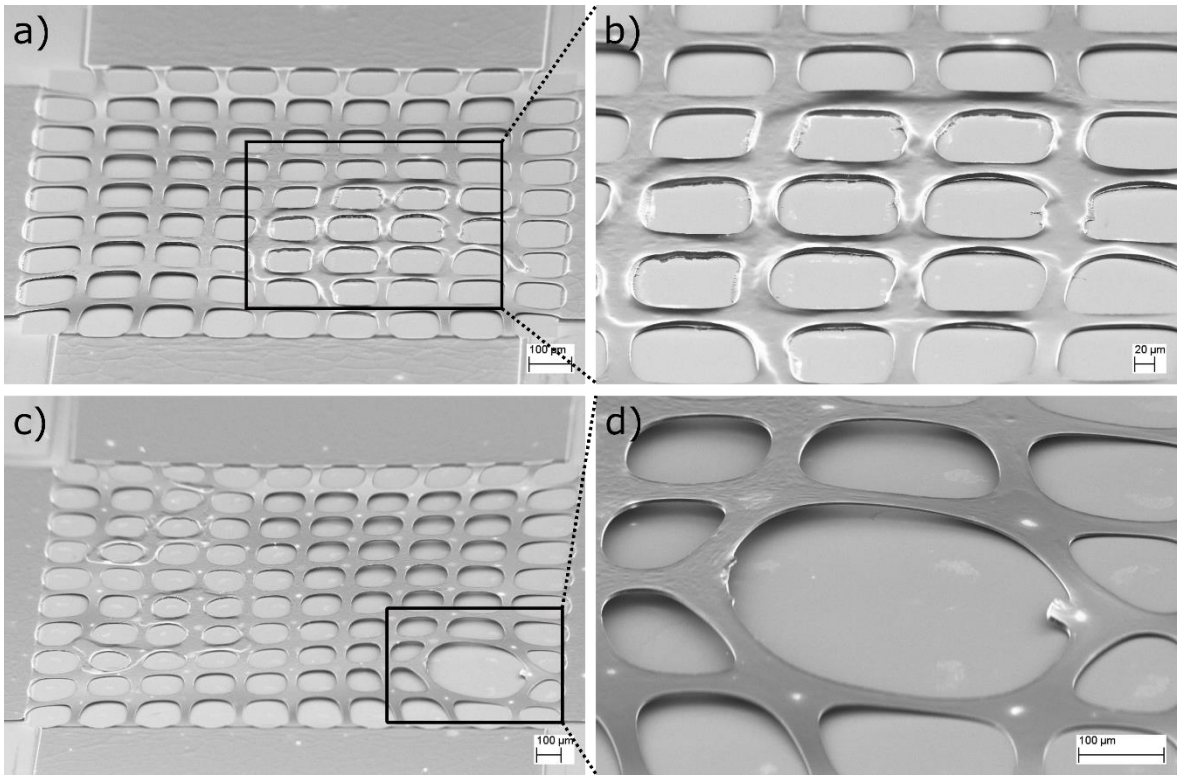

Figure 55: SEM images of unsuccessfully fabricated pyrolytic carbon membranes. (a, b) Larger membranes would often collapse and partially attach themselves to the substrate. (c, d) Random cracking of individual segments within the membranes was also observed. The size of the membranes represented in the images are (diameter/length, before pyrolysis); (a, b) 75 µm square membranes and (c, d) 112.5 µm round membranes.

Collapse of membranes

The first fabrication issue is the collapse of larger pyrolytic carbon membranes, as seen in figure 55 (a, b and c). This issue was observed for membranes with a hole diameter/length above 62.5 µm and stems from the same origin as the collapsed pyrolytic carbon bridges, discussed in section 6.2.2. However, because the membranes are suspended between four anchor points they possess a better structural stability over pyrolytic carbon bridges, allowing for the fabrication of larger membranes with a higher success rate. The structural stability is further improved by the presence of holes, which reduce the weight of the membranes and allow for a better distribution of stress within the structure.

For all collapsed membranes, the relaxation of residual stress and thermal expansion of SU-8 would result in a partial attachment of the membrane to the substrate. This means that only one side the membrane would come into contact with the substrate, while the remainder of the structure would remain suspended above the substrate, as seen in figure 55 (a and c). This is most likely caused by a non-uniform distribution of stress within the membranes during pyrolysis, which leads to an uneven bending of the structure. As a result, the collapsed pyrolytic carbon membranes bend in a wave-like manner, where parts of the structure that are attached to the substrate bend downwards while the remaining structure bends upwards.

Whether or not the membranes would deflect significantly enough to come into contact with the substrate appeared to be completely random. However, the issue was more common with larger membranes as the bigger size and increased weight would allow for a greater degree of deflection. The issue was observed with 75 % of membranes with a hole diameter/length of 112.5 µm and was reduced to less than 25 % of membranes with a hole diameter/length of 62.5 µm. Smaller membranes did not experience this issue as their good structural stability would restrict them from deflecting significantly enough to reach the substrate.

Cracking of membranes

The second fabrication issue that was observed is the cracking of pyrolytic carbon membranes, as seen in figure 55 (c and d). This issue also stems from the same origin as the cracking of pyrolytic carbon bridges, discussed in section 6.2.2. Cracking of the membranes was noted especially around the structure's edges, as the extensive stretching of the membranes close their anchor points would lead to a greater buildup of tensile stress.

As with the cracking of pyrolytic carbon bridges, the cracking of membranes was not related to their size and would occur completely randomly. On the other hand, the pyrolysis temperature did appear to have an effect on the issue. Higher temperatures would typically lead to a slightly higher number of cracked membranes, as the greater contraction of the resist would cause higher levels of stress in the structure. Overall, approximately 5 % of all membranes would experience cracking. All fabrication issues of pyrolytic carbon membranes are summarized in table 7.

Table 7: Fabrication issues of pyrolytic carbon membranes in relation to their size.

Hole Length/ Diameter [µm] \ Shape	Round	Square
112.5	▼	▼
100	▼	▼
87.5	▼	▼
75	▼	▼
62.5	▼	▼
50		
37.5		
25		
12.5		

▼ Collapse

During pyrolysis No issues

6.2.4 Cantilevers

Figure 56 shows SEM images of successfully fabricated SU-8 cantilevers before and after pyrolysis. Before pyrolysis, cantilevers with a length of up to 50 µm possess a relatively straight profile with no distinct signs of bending, as seen in figure 56 (a). On the other hand,

cantilevers with a length of over 100 µm exhibit a positive deflection at an angle between approximately 5 and 10°, as seen in figure 56 (b, c and d).

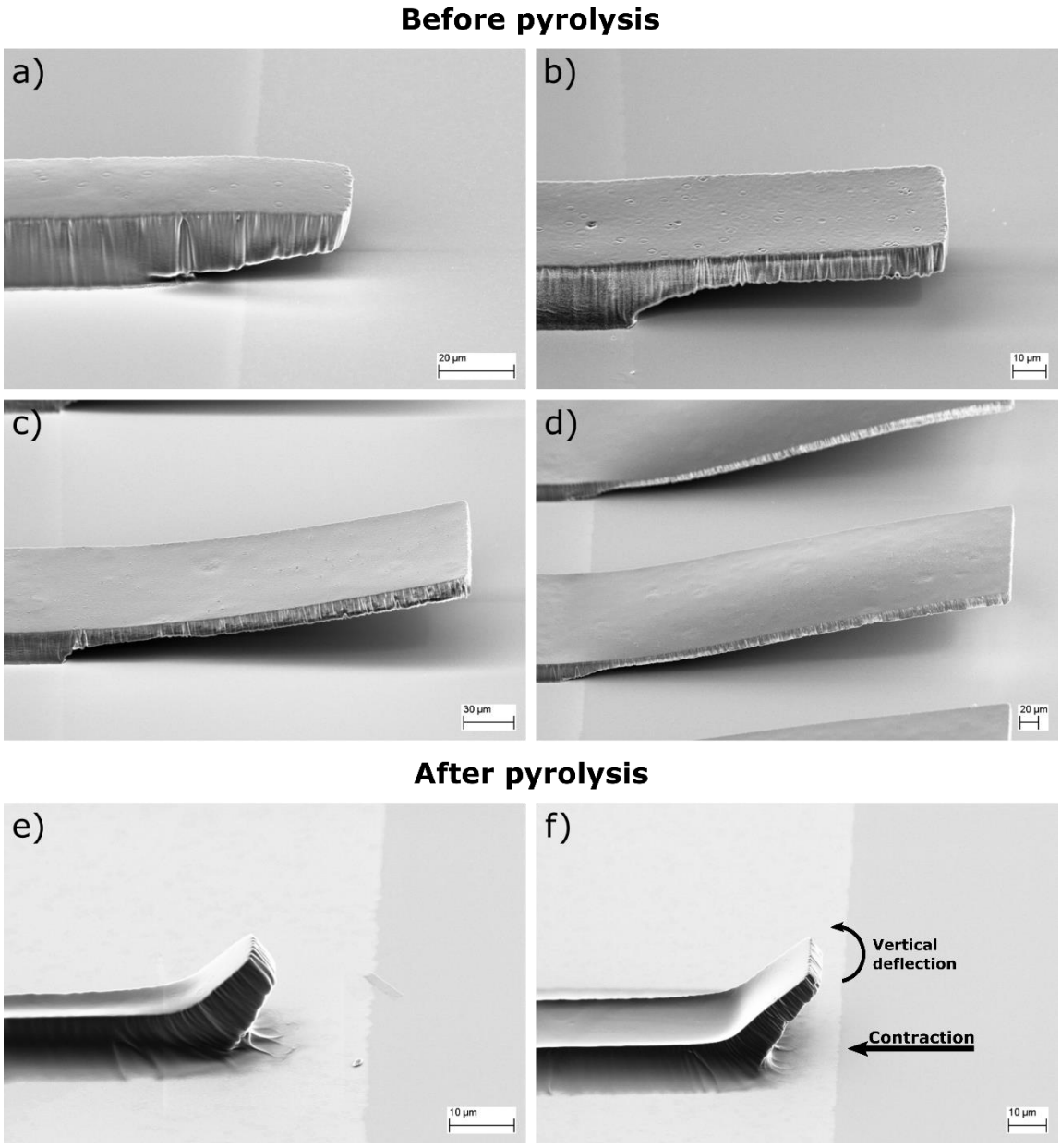

Figure 56: SEM images of successfully fabricated SU-8 cantilevers with varying sizes, before and after pyrolysis (length x width before pyrolysis); (a) 30 x 30 µm, (b) 100 x 50 µm, (c) 250 x 100 µm, (d) 500 x 200 µm, (e) 20 x 20 µm and (f) 50 x 50 µm. Before pyrolysis, the residual stress gradients in the resist cause a positive deflection of the SU-8 cantilevers, which becomes more distinctive as the length of the cantilevers increases. During pyrolysis, the cantilevers bend even further due to the uneven lateral contraction of the anchor points.

The deflection of the SU-8 cantilevers is primarily attributed to residual stress gradients in the resist. These stress gradients can develop due to numerous factors including, the mismatch in the coefficients of thermal expansion between the substrate, SU-8 and the sacrificial layer, temperature gradients formed during soft baking and post-exposure baking, as well as gradients of residual solvent concentrations in the polymer matrix [110]. Because the cantilevers are attached to a single anchor point, the residual stress is able to cause a noticeable deflection of the structure.

The results obtained in this study indicate that the residual stress is most likely eliminated from the SU-8 during the initial stages of pyrolysis. This would cause a negative deflection of the suspended microstructures, which can consequently lead to the collapse of a suspended structure. These observations are further supported by Keller *et al.* [110] who noted a reduction of residual stress in SU-8 cantilevers at higher hard baking temperatures, and a subsequent negative deflection of the suspended structures. The residual stress can be reduced by optimizing the baking steps for SU-8 [110].

During pyrolysis, the successfully fabricated pyrolytic carbon cantilevers contract in all directions and deflect upwards at an approximately 45° angle, as seen in figure 56 (e and f). The deflection of the pyrolytic carbon cantilevers is caused by the uneven lateral contraction of the anchor points, which pull the cantilevers further back at the top of the structure than at the bottom. As a result, the cantilevers develop a transverse stress gradient which causes them to deflect upwards [9], [12].

In order to prevent the deflection of SU-8 cantilevers during pyrolysis, Kurek *et al.* [12] suggested pyrolyzing the resist before removing the sacrificial layer. This way, the cantilevers not only retain a straight profile but also preserve their initial lateral dimensions. However, if the pyrolysis is to be done before removing the sacrificial layer, the sacrificial material must not be polymer based. Instead, inorganic materials with a good SU-8 adhesion and high melting points must be used (e. g. Ti or SiO_2) [25]. Alternatively, pyrolytic carbon cantilevers can be fabricated without the use of a dedicated sacrificial layer but are instead released from the substrate by etching the wafer itself [12]. These techniques can also be applied to other suspended microstructures, in order to preserve their shape and dimensions during pyrolysis.

Like other suspended pyrolytic carbon microstructures in our study, the pyrolytic carbon cantilevers would also experience various fabrication issues, as presented in figure 57. However, because the cantilevers are attached to a single anchor point, they possess a very weak structural stability, making them far less stable than bridges or membranes. In fact, the structural stability of the cantilevers was so poor that not a single pyrolytic carbon cantilever with a length of over 100 µm was successfully fabricated. The encountered fabrication issues include the extensive bending and the collapse of the cantilevers.

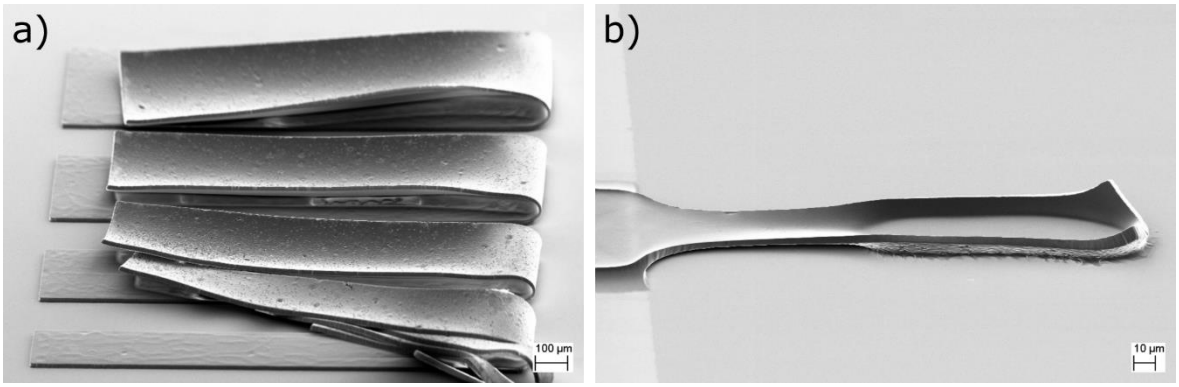

Figure 57: SEM images of unsuccessfully fabricated pyrolytic carbon cantilevers. (a) Before pyrolysis, longer cantilevers would often bend far beyond the deflection angles caused by residual stress. (b) During pyrolysis, the majority of cantilevers would collapse and attach themselves to the substrate. The size of the cantilevers in the images are (length x width, before pyrolysis); (a) 1500 µm long cantilevers and (b) 250 x 100 µm.

Extensive bending of cantilevers

Before pyrolysis, SU-8 cantilevers with a length of 1500 µm, as well as cantilevers with lengths of over 450 µm and widths of up to 50 µm were often observed bending far beyond the standard deflection angles caused by residual stress. These cantilevers would bend both vertically and laterally up to 180°, as seen in figure 57 (a). If a cantilever were to bend 180°, it would attach itself to their own anchor points or even break off from its anchor point entirely. This issue can be attributed to the significantly poor structural stability of the SU-8 cantilevers, which would cause them to bend in the various pressure gradients experienced during the development of SU-8 and subsequent drying of the samples.

Collapse of cantilevers

Another fabrication issue is the collapse of pyrolytic carbon cantilevers, as seen in figure 57 (b). This issue was observed for all cantilevers with lengths of over 100 µm and was so common that not a single cantilever beyond this length was successfully fabricated on any of the samples. The collapse of pyrolytic carbon cantilevers stems from the same origin as the collapse of pyrolytic carbon bridges and membranes, discussed in section 6.2.2. However, because cantilevers are attached to a single anchor point, they are able to deflect much further than bridges or membranes, resulting in the collapse of much smaller structures. Cantilevers shorter than 50 µm did not experience this issue as their structural stability would restrict them from deflecting significantly enough to reach the substrate. All fabrication issues of pyrolytic carbon cantilevers are summarized in table 8.

Table 8: Fabrication issues of pyrolytic carbon cantilevers in relation to their size.

Group 1

Width [µm] \ Length [µm]	1500	500	250	100
500	◇ ▼	▼	▼	▼
400	◇ ▼	▼	▼	▼
300	◇ ▼	▼	▼	▼
200	◇ ▼	▼	▼	▼
100	◇ ▼	▼	▼	▼
50	◇ ▼	◇ ▼	▼	▼
40	◇ ▼	◇ ▼	▼	▼
30	◇ ▼	◇ ▼	▼	▼
20	◇ ▼	◇ ▼	▼	▼
10	◇ ▼	◇ ▼	◇ ▼	▼

Group 2

Length/ Width [µm]	
500	▼
400	▼
300	▼
200	▼
100	▼
50	
40	
30	
20	
10	

Group 3

Length [µm]	Width [µm]	
490	10	◇ ▼
480	20	◇ ▼
470	30	◇ ▼
460	40	◇ ▼
450	50	◇ ▼
400	100	▼
300	200	▼
200	300	▼
100	400	▼
10	500	

◇ Extensive bending ▼ Collapse

Before pyrolysis | During pyrolysis | No issues

6.2.5 Mushrooms

Figure 58 shows SEM images of successfully fabricated SU-8 mushrooms before and after pyrolysis. Before pyrolysis, the mushrooms possess a relatively flat profile with no distinct signs of bending.

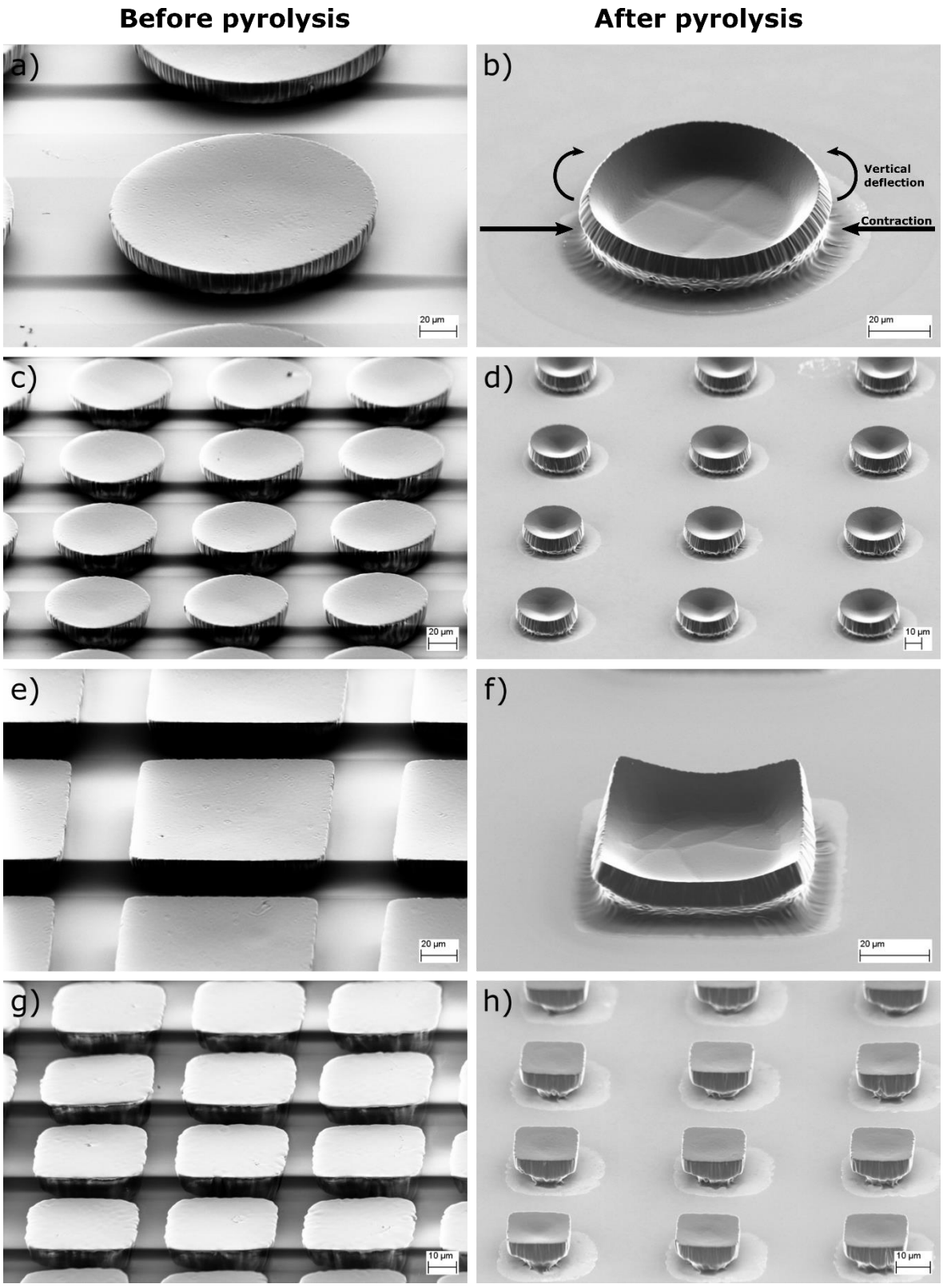

Figure 58: SEM images of successfully fabricated SU-8 mushrooms with varying shapes and sizes, before and after pyrolysis (diameter/length of the anchor points before pyrolysis); (a, b) 100 µm round mushrooms, (c, d) 50 µm round mushrooms, (e, f) 75 µm square mushrooms and (g, h) 25 µm square mushrooms. During pyrolysis, the mushrooms contract in all directions and experience a positive deflection. The deflection is isometric for round mushrooms, while square mushrooms tend to deflect more around the corners. As the mushrooms get smaller, the deflection becomes less prominent.

During pyrolysis, the mushrooms contract in all directions and deflect their suspended edges upwards, thus forming a structure that bears a resemblance to that of a cup rather than a mushroom. The deflection is caused by the uneven lateral contraction of the anchor points, which pulls the suspended edges further back at the top of the structure than at the bottom, thus deflecting them upwards in the same was as with pyrolytic carbon cantilevers. Round mushrooms deflect isometrically, while square mushrooms tend to exhibit a more significant deflection around the corners, as seen in figure 58 (f). The deflection is also more prominent with larger structures and becomes less significant as the size of the mushrooms decreases. For 25 µm pyrolytic carbon mushrooms, the structure retains a flat top without any noticeable deflection of the suspended sides, as seen in figure 58 (h).

Pyrolytic carbon mushrooms with a diameters/length of over 50 µm were successfully fabricated on all samples. On the other hand, smaller mushrooms would experience significant fabrication issues before pyrolysis, as presented in figure 59. These issues include the clustering of mushrooms and the complete removal of the mushrooms from the substrate.

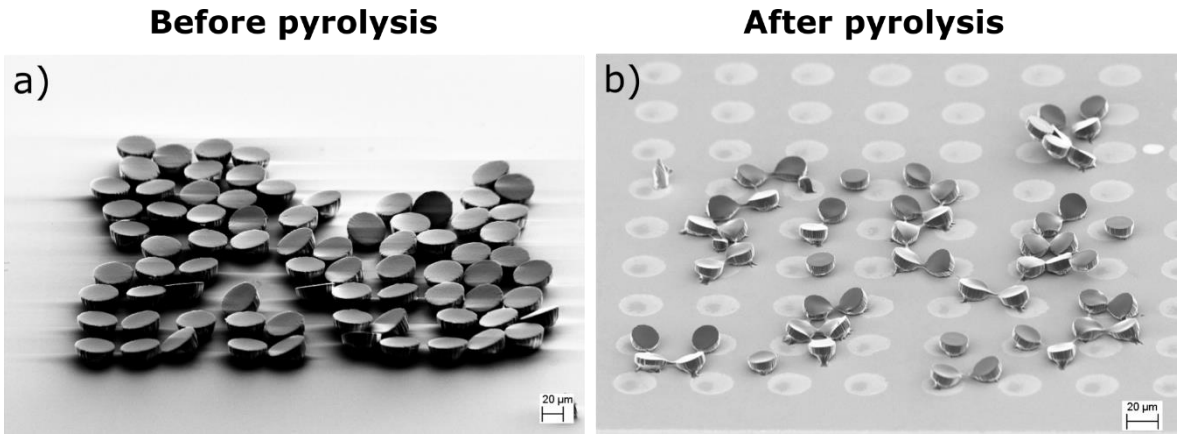

Figure 59: SEM images of unsuccessfully fabricated 25 µm round SU-8 mushrooms. (a) Smaller mushrooms would often shift from their original position before pyrolysis and form clusters. (b) After pyrolysis, the clustered mushrooms would remain attached to one another, despite the fact that the structures shrink.

Clustering of mushrooms

Round SU-8 mushrooms with a 25 µm and 37.5 µm diameter, as well as square SU-8 mushrooms with a 25 µm length, were often observed moving from their original position and forming clusters, as seen in figure 59. Movement of the mushrooms can be attributed to their small anchor points, which causes a poor attachment of the mushrooms to the substrate. As a result, the mushrooms can be easily moved from their original position by the various forces experienced during the development of SU-8 and drying of the samples. However, while the small anchor points do not provide enough support for the mushrooms to remain in their original position, the strong stiction forces of SU-8 keep the mushrooms attached to the substrate. If the mushrooms were to come into contact with one another, they would start to form clusters.

Clustering of the mushrooms was noted with all 25 µm round mushrooms, as well as approximately 30 % of 37.5 µm round mushrooms and 25 µm square mushrooms. The greater stability of square mushrooms comes as a result of a 21.5 % higher theoretical surface

area over round mushrooms whose diameter is equal the square mushrooms length. This allows the square mushrooms to better attach themselves to the substrate, thus providing them with a better structural stability.

Complete removal of mushrooms

Another observed fabrication issue is the complete removal of mushrooms from the substrate, which was noted for all mushrooms with a 12.5 µm diameter/length. One of the most likely explanations for this issue is that the combination of the mushrooms small anchor points and the gap formations between the sacrificial layer and SU-8, as discussed in section 6.2.1, prevents the mushrooms from developing the anchor points and coming into contact with the substrate entirely. As a result, the various forces experienced during the development of SU-8 can easily pick up the mushrooms and remove them from the substrate. The issue could potentially be avoided by minimizing the gap between the SU-8 and the sacrificial layer, or by using an entirely different fabrication method for the suspended microstructures. All fabrication issues of pyrolytic carbon mushrooms are summarized in table 9.

Table 9: Fabrication issues for pyrolytic carbon mushrooms in relation to their size.

Length/Diameter [µm] \ Shape	Round	Square
112.5		
100		
87.5		
75		
62.5		
50		
37.5	O	
25	O	O
12.5	X	X

O Clustering X Completely removed from the substrate

Before pyrolysis No issues

During the analysis of the pyrolytic carbon mushrooms, an interesting observation was made where random particles were found attach to the mushrooms, as seen in figure 60. This phenomenon is most likely the result of the electrostatic forces of pyrolytic carbon and the cup-shaped profile of the mushrooms, which would cause the mushrooms to attract and trap random particles from its surroundings. The origin and chemistry of these particles is unknown, although they most likely originate from the air or from the pyrolysis furnace.

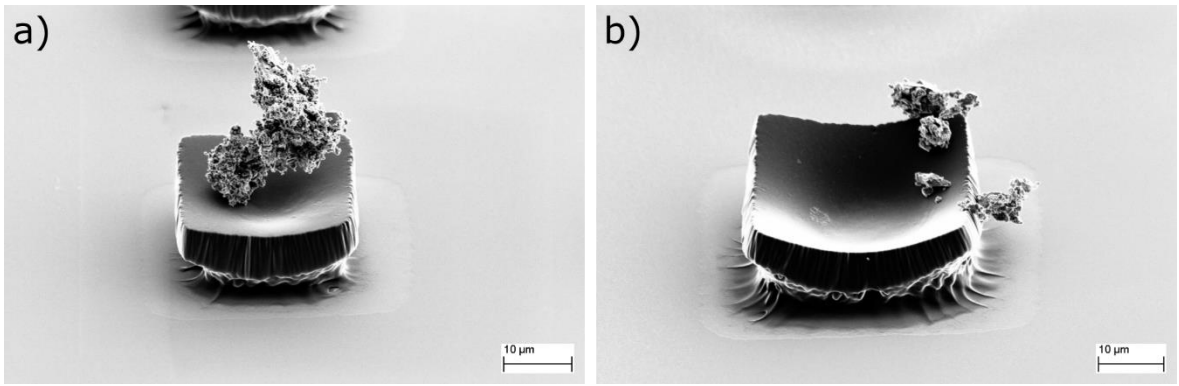

Figure 60: Particles attached to pyrolytic carbon mushrooms. The combination of electrostatic forces of pyrolytic carbon and the cup-shaped profile of the mushrooms would lead to the mushrooms attracting and trapping random particles from its surroundings. The chemistry and origin of these particles is unknown although, they most likely originate from the air of from the pyrolysis furnace. The length of the mushrooms in the images are (a) 37.5 µm and (b) 50 µm.

6.3 Shrinking of SU-8

Figure 61 shows the average height and relative thickness of pyrolytic carbon, as a function of the pyrolysis temperature. Before pyrolysis, the average height of the SU-8 microstructures (h_0) is approximately 16.91 µm. During pyrolysis, the SU-8 microstructures shrink to a relative thickness between 16.2 and 15.0 % of its initial value, which corresponds to a height (h) between 2.73 and 2.53 µm.

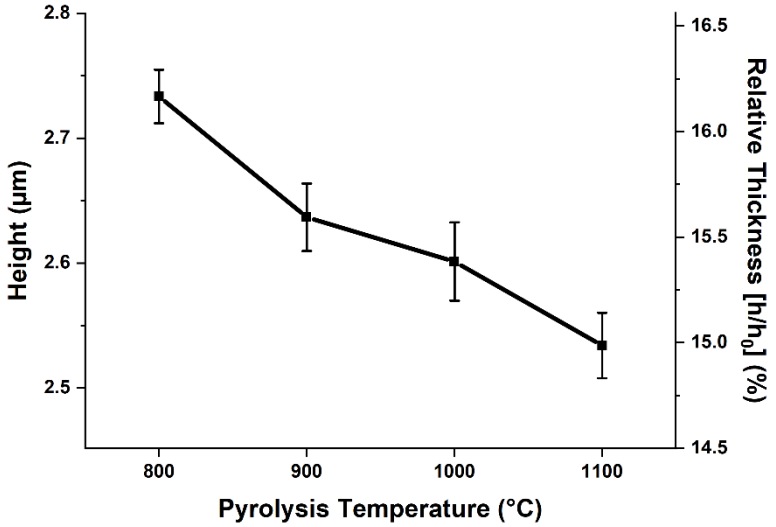

Figure 61: Average height and relative thickness (h/h_0) of pyrolytic carbon as a function of the pyrolysis temperature.

The high level of vertical shrinking occurs due to a relatively small initial thickness of the SU-8 structures. The small thickness allows for a more efficient outgassing of volatile elements from SU-8, thereby leading to a greater vertical contraction. The differences in the vertical contraction between the various pyrolysis temperatures are very minute as most of the contraction occurs at temperatures below 600 °C, where the outgassing of oxygen atoms is greatest [17]. However, the small differences can still be attributed to a slightly more efficient thermal degradation of SU-8 at higher pyrolysis temperatures.

Compared to the vertical shrinking, the lateral contraction of SU-8 is severely restricted by the resist's strong adhesion to the substrate. Due to the restricted lateral contraction of the resist and the varying sizes of the measured microstructures, the relative lateral contraction of SU-8 cannot be determined unambiguously. Instead, the lateral contraction can only be analyzed in terms of absolute changes in the size of the SU-8 microstructures ($_{\Delta}L$).

Figure 62 shows the average absolute lateral contraction of SU-8 microstructures as a function of the pyrolysis temperature. The results show that during pyrolysis the SU-8 experiences a lateral contraction between approximately 17.1 and 18.0 µm. The contraction is greater at lower pyrolysis temperatures as the increased height of the microstructures allow the resist to shrink more freely inwards. These results can also be applied to suspended microstructures in order to determine the lateral stretching of bridges and membranes.

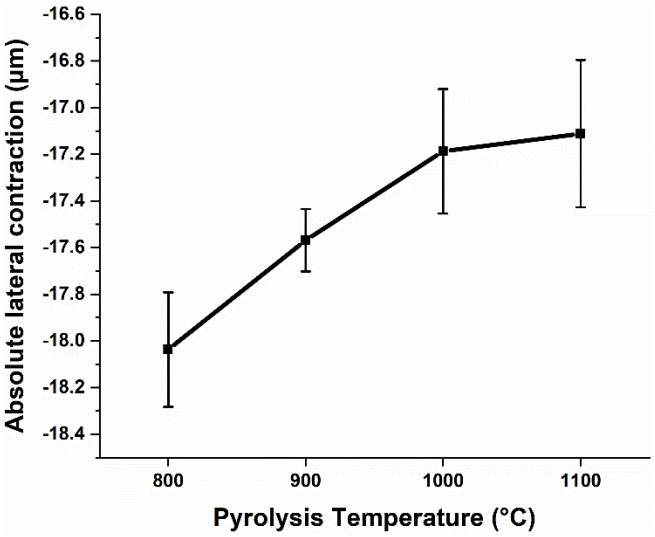

Figure 62: Absolute lateral contraction of SU-8 microstructures as a function of the pyrolysis temperature. The initial lateral dimensions of the measured SU-8 microstructures are; 496.56 µm, 496.98 µm and 1803.63 µm.

Whether a higher degree of shrinking would prove an advantage or drawback to a C-MEMS device, depends on the design of the system. For example, Lim *et al.* [30] demonstrated that by suspending a pyrolytic carbon mesh above a substrate-bound electrode, a higher degree of vertical shrinking would cause the anchor points to bring the suspended electrode closer to the substrate-bound electrode. In turn, this would lead to faster redox cycling of the analyte and subsequent amplification of the redox current in a C-MEMS redox-based electrochemical sensor. On the other hand, systems that are based solely on substrate-bound structures have shown that a greater degree of shrinking not only reduces the overall size of the microstructures but also pulls them further apart from one another. In turn, this would lead a reduced quality of the C-MEMS device [27].

6.4 Electrical resistivity of pyrolytic carbon

Figure 63 shows the electrical resistivity of the unpatterned pyrolytic carbon films as a function of the pyrolysis temperature. The resistivity of pyrolytic carbon ranges from $1.29 \cdot 10^{-4}$ Ωm, for films pyrolyzed at 800 °C, to $2.92 \cdot 10^{-5}$ Ωm, for films pyrolyzed at 1100 °C. The biggest drop in the electrical resistivity occurs at temperatures between 800 to 900 °C, which coincides with the temperature range in which the outgassing of hydrogen atoms from the precursor occurs [13], [17]. These results confirm that the degree to which the precursor is carbonized is by far the greatest factor contributing to the electrical properties of pyrolytic carbons.

As the pyrolysis temperature is further increased and the level of carbonization begins to reaches its maximum value, electrical resistivity begins to decrease at a more gradual pace. At this point, drops in electrical resistivity can be attributed to the increased ordering of the crystal structure, growth of the graphitic crystallites and the elimination of the sp^3 phase [53], [54]. If the temperature were to be increased further, the electrical resistivity would most likely reach a final value beyond which it could not be reduced. The limiting value of the electrical resistivity is a consequence of the grain boundary effect, which limits the transport of electrons through the material [111]. Since the electrical resistivity of pyrolytic carbon changes with varying pyrolysis temperatures, this allows us to easily modify the electrical properties of the material based on the desired application.

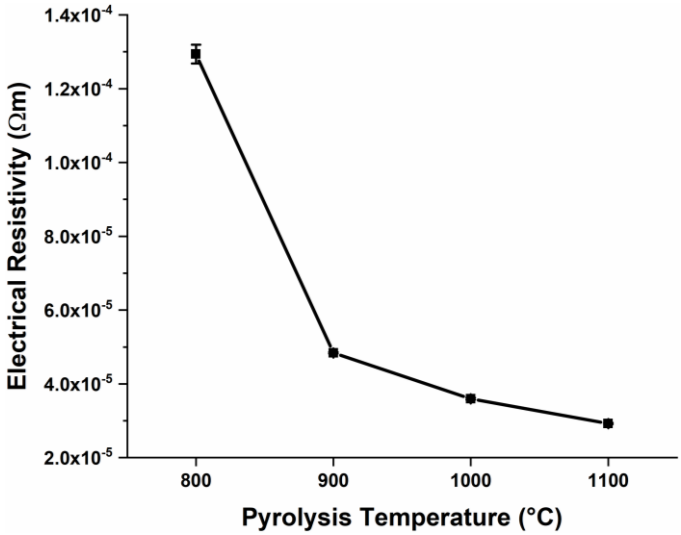

Figure 63: Electrical resistivity of pyrolytic carbon as a function of the pyrolysis temperature.

The electrical properties of pyrolytic carbons are a particularly important when utilizing C-MEMS as microelectrodes in electrochemical sensors. A lower electrical resistivity of the electrode material allows for a greater heterogeneous electron transfer between the electrode and electroactive species which, in turn, amplifies the redox current and improves the quality of the sensor [2]. Table 10 compares the electrical resistivity of pyrolytic carbons with other common carbon allotropes, as well as some common electrode materials used in electrochemical bioMEMS sensors.

Table 10: Electrical resistivity of pyrolytic carbons in comparison with other common carbon allotropes and electrode materials used in electrochemical bioMEMS sensors. Other pyrolytic carbons represented in this table were derived through pyrolysis of SU-8 at temperatures above 800 °C.

Material	Electrical resistivity [Ωm]	Reference
Pyrolytic carbon	**$2.92 \cdot 10^{-5} – 1.29 \cdot 10^{-4}$**	**This work**
	$5.5 \cdot 10^{-5} – 1.3 \cdot 10^{-4}$	[16]
	$6.8 \cdot 10^{-5} – 6.0 \cdot 10^{-3}$	[17]
	$3.2 \cdot 10^{-5} – 9.3 \cdot 10^{-5}$	[20]
	$6.8 \cdot 10^{-5} – 4.76 \cdot 10^{-4}$	[53]
Graphite	$4.0 \cdot 10^{-7} – 1.7 \cdot 10^{-3}$	[2]
a-C	$5.0 \cdot 10^{-4} – 8.0 \cdot 10^{-4}$	[112]
Diamond	10^{18}	
Gold	$2.44 \cdot 10^{-8}$	
Platinum	$1.1 \cdot 10^{-7}$	
ITO	$\sim 10^{-6}$	[113]

Table 10 shows that the electrical resistivity of pyrolytic carbon, obtained in this study, is comparable to that of other pyrolytic carbons. In comparison to other common carbon materials, its electrical resistivity falls between that of a-C and graphite, indicating that the crystal structure of pyrolytic carbon closely resembles that of nanocrystalline graphite. Although the electrical resistivity of pyrolytic carbon is not as low as that of gold, platinum or indium tin oxide (ITO), it is sufficient enough for the material to be used as an electrode material in electrochemical sensors.

6.5 Crystallinity of pyrolytic carbon

Figure 64 shows the Raman spectrum of a pyrolytic carbon film pyrolyzed at 900 °C. Three characteristic peaks can be observed in the spectrum, as presented in chapter 3; a D peak at ~1350 cm^{-1}, a G peak at ~1590 cm^{-1} and a 2D peak at ~2800 cm^{-1}. The high intensity of the D peak, as well as the partial overlapping of the D and G peaks indicates a high level of disorder within the crystal structure of the material.

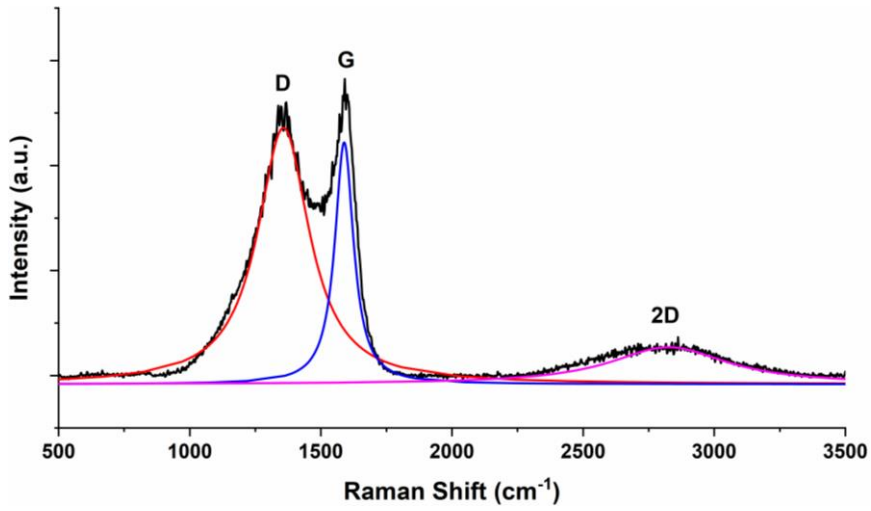

Figure 64: Raman spectrum of a pyrolytic carbon film pyrolyzed at 900 °C. The underlying curves show the fitting of the D, G and 2D peaks with Lorentzian functions.

Analysis of the D and G peak intensities show that the peaks intensity ratio ($I_{(D)}/I_{(G)}$) decreases from 2.98 to 2.10 as the pyrolysis temperature is increased from 800 to 1100 °C. According to the three-stage model proposed by Ferrari and Robertson [60], a high $I_{(D)}/I_{(G)}$ ratio signifies a highly disordered nanocrystalline structure of the material. At the same time, a decrease in the $I_{(D)}/I_{(G)}$ ratio indicates that the crystallinity of pyrolytic carbon increases as the pyrolysis temperature is increased. In fact, the in-plane crystallite size (L_a) was calculated to increase from 6.45 to 9.15 nm. Figure 65 shows the $I_{(D)}/I_{(G)}$ ratio, as well as the crystallite size of pyrolytic carbon, as a function of the pyrolysis temperature.

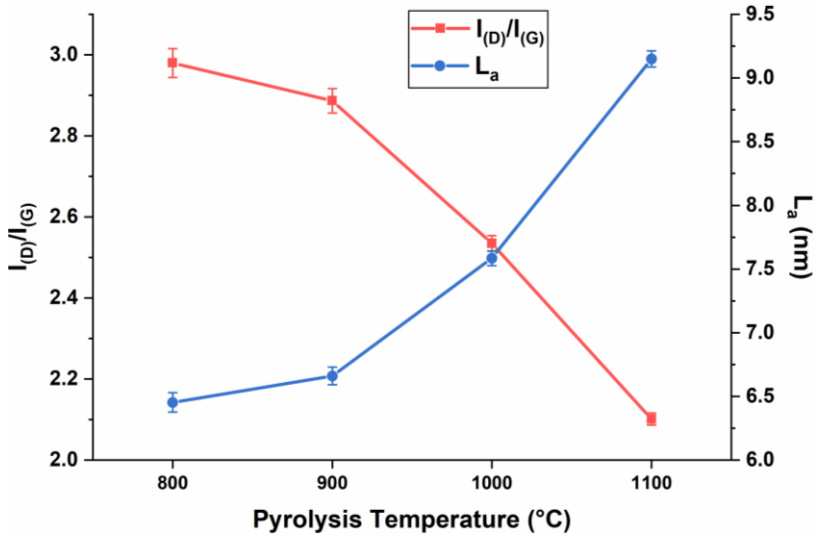

Figure 65: $I_{(D)}/I_{(G)}$ ratio and L_a of pyrolytic carbon as a function of the pyrolysis temperature.

Next, the D and G peaks were analyzed in terms of their position. The results are presented in figure 66 and show notable shifts in the peaks positions towards higher frequencies with increasing pyrolysis temperatures. These result are quite surprising as, according to the three-stage model [60], the position of the G peak should be moving towards lower frequencies with a more ordered graphitic structure. One of the most likely explanations for this phenomenon is that the shifts towards higher frequencies are caused by increasing levels of local stress and strain within the material [74].

Previous studies [73], [74] have shown that strains imposed on graphitic sheets can cause shifts in the position of both the D and G peaks. Because the D peak is more sensitive to low energy defects, this results in greater shift in the peaks position in comparison to the G peak. This is also evident from our results, where the position of the D peak shifts by 15 cm^{-1} as the pyrolysis temperature is increased from 800 to 1000 °C, while the position of the G peak shifts only by 8 cm^{-1}. The downshift of the D peak at 1100 °C can be attributed to the partial annealing of the crystal structure. Annealing reduces the stress within the material, thus leading to shift in the peaks position towards lower frequencies.

While the shifts in the peaks position towards higher or lower frequencies can be specifically attributed to isotropic compressive or tensile strains, the application of anisotropic stress has a much more complex effect on the peak's positions. This means that due to the random orientation of the graphitic sheets in pyrolytic carbon, the shifts in the peaks position cannot be unambiguously attributed to a specific type of strain [72].

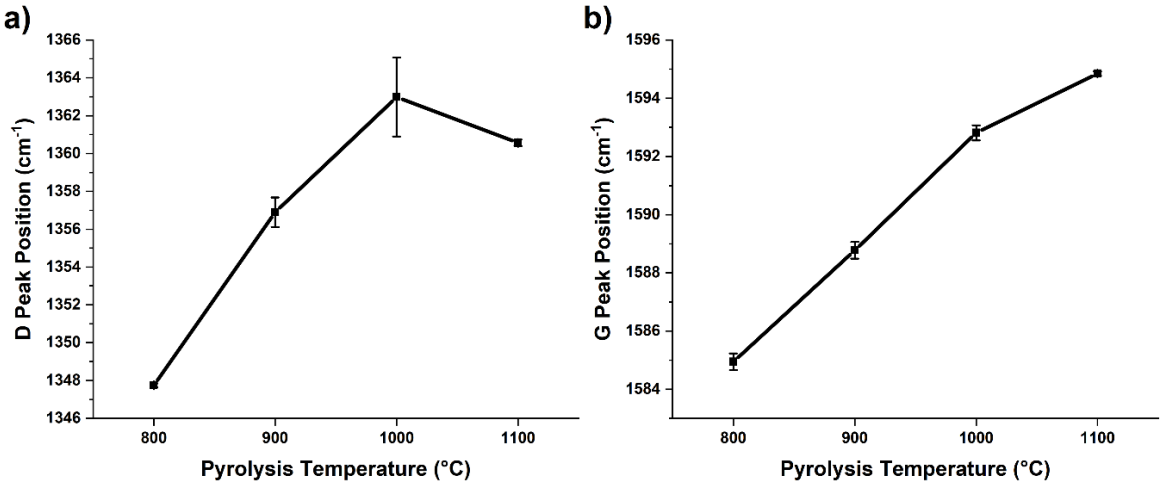

Figure 66: Position of the (a) D and (b) G peaks as a function of the pyrolysis temperature.

Another point of interest is the width (FWHM) of the D and G peaks. Both the $FWHM_D$ and $FWHM_G$ corelate with the structural state of the material and increase with a higher degree of structural disorder. The $FWHM_D$ is particularly relevant in the characterization of pyrolytic carbons as it is very sensitive to low energy in-plane structural defects (e. g. disorientation of the graphitic layers) and can thus be used as an indicator on the presence of small localized structural disorders. Furthermore, the $FWHM_D$ can also provide information on the bending of graphitic sheets, where a greater curvature give rise to higher $FWHM_D$ values [72], [114].

Figure 67 shows the FWHM of the D and G peaks a function of the pyrolysis temperature. Overall, the $FWHM_G$ does not show any significant changes between the different pyrolysis temperatures. On the other hand, the $FWHM_D$ shows a much clearer trend and decreases from 240 to 191 cm^{-1} as the pyrolysis temperature is increased from 800 to 1100 °C. This indicates that higher pyrolysis temperatures lead to a lower number of structural defects and less curved graphitic sheets of the pyrolytic carbon structure. The significant drop in the $FWHM_D$ at 1100 °C can be attributed to the partial annealing of the material, which results in the gradual removal of local low-energy defects and straightening of the graphitic sheets. This result also coincides with the shift in the position of the D peak towards lower frequencies at 1100 °C, confirming a partial annealing of the crystal structure.

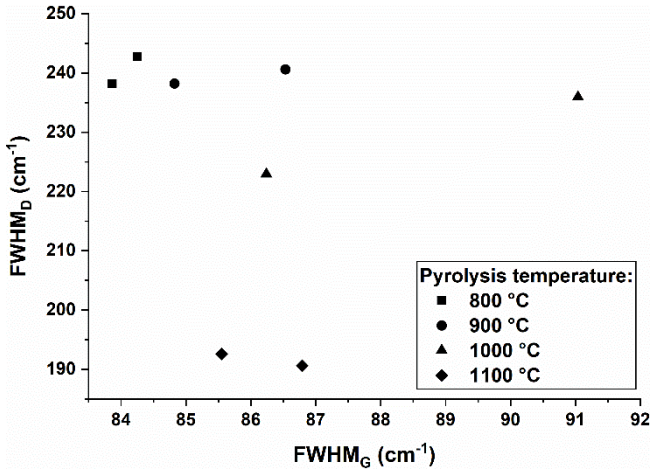

Figure 67:FWHM of the D and G peaks as a function of the pyrolysis temperature.

Although Raman spectroscopy of pyrolytic carbons can provide us with good information on the crystallinity, crystallite sizes and the presence of structural defects, other properties related to the materials structure, such as the sp^2:sp^3 ratio or the level of carbonization, are much harder to analyze. Thus, other characterization methods, such as EELS, XPS or UV Raman spectroscopy are required in order to determine these properties [14], [54], [60].

6.6 Surface roughness

Figure 68 shows AFM images of the surface topography for unpatterned SU-8 and pyrolytic carbon films pyrolyzed at different temperatures.

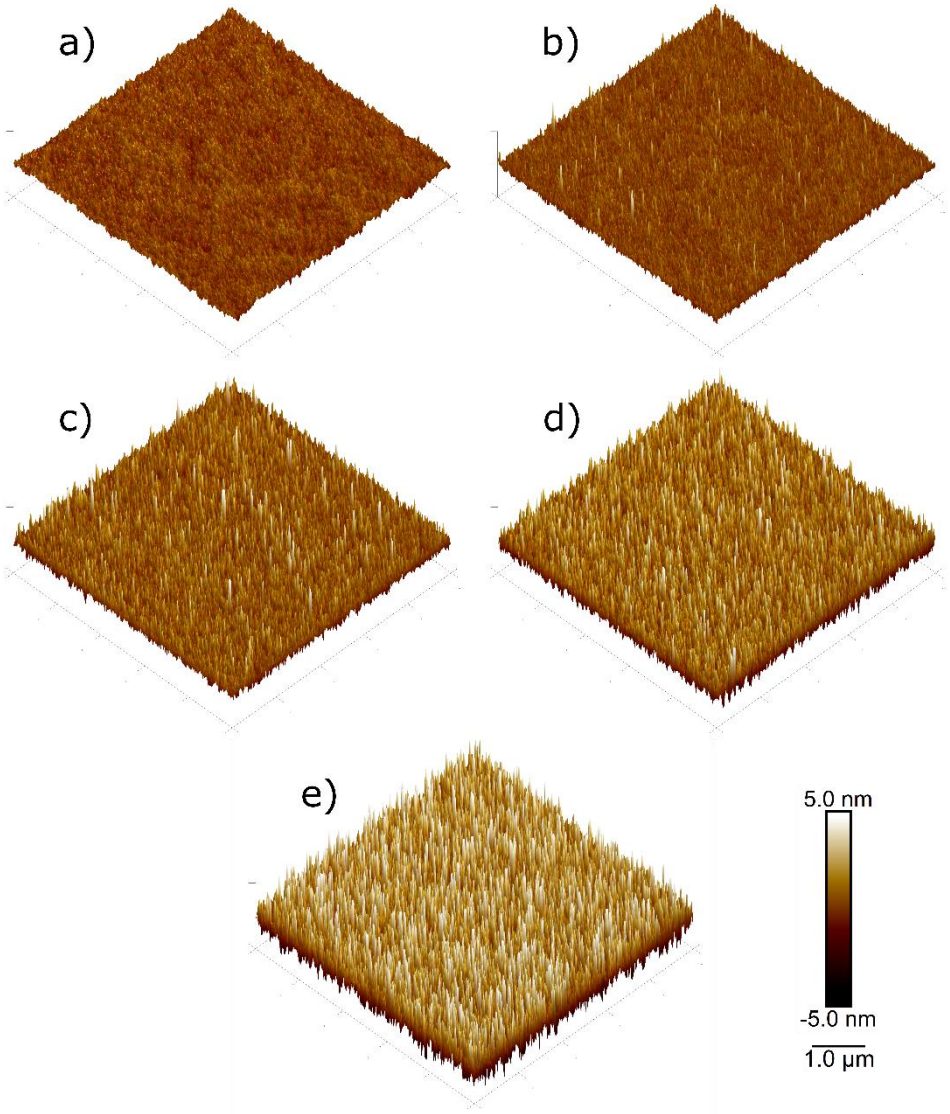

Figure 68: AFM images of (a) SU-8, as well as pyrolytic carbon films pyrolyzed at (b) 800, (c) 900, (d) 1000 and (e) 1100 °C. The images show a clear increase in the surface roughness at higher pyrolysis temperatures, due to the formation of spikes on the surface of pyrolytic carbon.

Before pyrolysis, the SU-8 films possess a very smooth surface with a mean surface roughness of 0.27 nm. During pyrolysis, small nanometer-sized spikes form on the surface of pyrolytic carbon which, consequently, increase the surface roughness of the material. The origin of these spikes is not entirely clear although, they are most likely formed by volatile

atoms which remove themselves by bursting through the surface of pyrolytic carbon, thereby leaving behind small spikes in the surface topography of the material. The spikes reach a height between 5 and 10 nm, with diameters ranging from 50 to 100 nm.

At lower pyrolysis temperatures, the spikes are very few and far in between. As the pyrolysis temperature is increased, the density of spikes significantly rises while their size remains the same. As a result, the mean surface roughness of pyrolytic carbon increases from 0.33 nm, when pyrolyzed at 800 °C, to 1.27 nm, when pyrolyzed at 1100 °C. The increase in spike density is most likely caused by greater decomposition rates of SU-8 at higher pyrolysis temperatures which, in turn, increase the outgassing rates of volatile atoms. As a result, the volatile atoms burst through the surface of pyrolytic carbon more frequently, thus increasing the number of spikes. Figure 69 shows the mean surface roughness (S_a) of SU-8 and pyrolytic carbon as a function of the pyrolysis temperature.

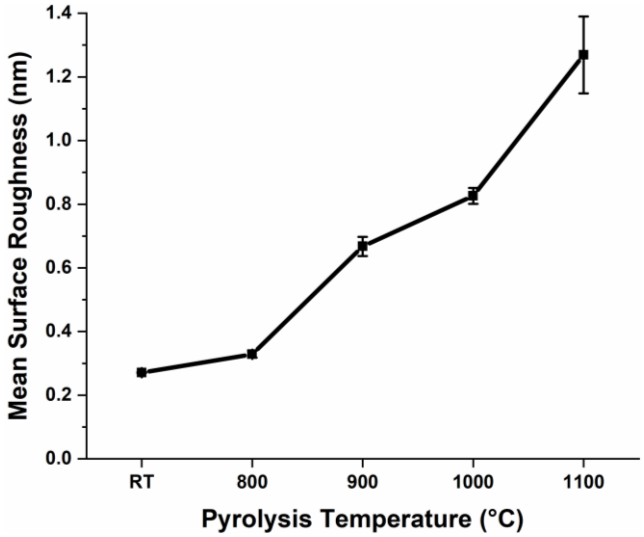

Figure 69: Mean surface roughness of SU-8 and pyrolytic carbon as a function of the pyrolysis temperature.

The results obtained in this study are surprisingly different from previous reports [14], [20], [44], which show that the surface roughness of pyrolytic carbons should not be dependent on the pyrolysis temperatures but rather on the heating rates. The results are even more unexpected as the heating rates used in this study were lower than those used in other published articles. Nevertheless, the surface roughness of pyrolytic carbon is still well within the range of expected values and comparable to that of other pyrolyzed photoresists.

In general, a higher surface roughness is more desirable as it increases the effective surface area of pyrolytic carbon, thereby improving its performance in devices such as electrochemical sensors, cell-based sensors and energy storage systems. On the other hand, a very high surface roughness can potentially also lead to some adversary affects. For example, Brunetti *et al.* [115] demonstrated that an increase in the surface roughness of gold microelectrodes, used in cell-based sensors, above 54.2 nm would cause a cascade of signaling processes which would result in the necrosis of cells. This shows that the surface roughness of the material should always be accounted for, based on the application of the device.

7. Summary and conclusions

The aim of this work was to fabricate and study the issues related to the fabrication of suspended C-MEMS microstructures with varying shapes and sizes, as well as to investigate the properties of unpatterned pyrolytic carbon films in relation to the pyrolysis temperature. Suspended SU-8 microstructures were fabricated with the use of sacrificial layers and pyrolyzed in an inert atmosphere, in order to obtain pyrolytic carbon microstructures. The use of positive photoresist as a sacrificial material has proven to be well suited for the fabrication of suspended SU-8 microstructures. The method allows for a simple fabrication of suspended structures with dimensional accuracies in the range of micrometers, while the sacrificial layer can be easily removed without damaging the SU-8.

While the structural stability of the suspended SU-8 microstructures has shown to be relatively good, the vast majority of fabrication issues would occur during pyrolysis of the resist. Based on the analysis of the fabrication issues surrounding the development of suspended pyrolytic carbon microstructures, we can conclude that from a structural standpoint, pyrolysis of SU-8 microstructures appears to occur in two stages;

(i) The first stage occurs at temperatures up to the first dwell point at 300 °C. During this stage the residual stress is gradually removed from the resist while the high temperatures lead to a thermal expansion of SU-8. While this step may not have any effect on the stability of substrate-bound structures, it has shown to have a much greater influence on the structural stability of suspended SU-8 microstructures. The removal of residual stress and thermal expansion of SU-8 lead to the softening of the resist, thereby causing a negative deflection of the suspended microstructures. The level of deflection primarily depends on the initial structural stability of the suspended microstructure, with larger single-clamped structures having a much lower stability than smaller multi-clamped structures. If the deflection is significant enough for the suspended structure to come into contact with the substrate, it will remain attached to the substrate throughout the pyrolysis process due to stiction forces. The issue becomes more severe as the size of the suspended structures increases and the distance to the substrate decreases.

(ii) The second stage occurs at temperatures from the first dwell point at 300 °C up to the final pyrolysis temperature. This stage involves the outgassing of volatile atoms which subsequently causes the contraction of SU-8. The contraction of the resist first pulls the suspended structures back to their original position, after which the structures experience a positive deflection due to the uneven lateral contraction of the anchor points. As with the negative deflection experienced during the first stage of pyrolysis, the positive deflection is much more extensive with single-clamped microstructures. The shrinking of anchor points also causes the elongation of multi-clamped structures, which subsequently leads to the buildup of tensile stress and can even result in the cracking of the suspended structures.

To the authors knowledge, an analysis of the pyrolysis process for SU-8 microstructures has yet to be conducted in such a way as presented above. While numerous articles discuss the second stage of pyrolysis, there is considerable lack of studies discussing the first stage of pyrolysis. Thus, such an outline will help us better understand the pyrolysis process of SU-8.

Another particularly novel aspect of this work is the fabrication of cup-shaped pyrolytic carbon microstructures. The specific shape of the microstructures and the electrostatic nature of pyrolytic carbon would allow the cups to attract and trap random particles from their surrounding environment. These findings lead us to believe that such structures could potentially be used as a novel method for the trapping of micro and nanoparticles in devices such filtration systems. Thus, further studies into the development and implementation of such structures in C-MEMS devices are encouraged.

Analysis of the unpatterned pyrolytic carbon films shows an increase in the electrical conductivity, surface roughness and crystallinity of the material with higher pyrolysis temperatures. The pyrolytic carbon films exhibit very good electrical properties, with resistivity values ranging from $1.29 \cdot 10^{-4}$ to $2.92 \cdot 10^{-5}$ Ωm. In fact, the electrical resistivity values obtained in this work are amongst the lowest values reported for pyrolyzed resist [20]. At the same time, AFM measurements show an increase in surface roughness of the material from 0.33 to 1.27 nm, as the pyrolysis temperature is raised from 800 to 1100 °C. Although the surface roughness values at higher pyrolysis temperatures are slightly greater than those reported in previous studies [14], [20], [44], a higher surface roughness can be more desirable as in increases the effective surface area of pyrolytic carbon. Based on these results we can conclude that the use of higher pyrolysis temperatures is better suited for purposes of electrochemical sensors and cell-based biosensors as the lower electrical resistivity and higher surface roughness allow for a greater heterogeneous electron transfer between the electrode and electroactive species.

The Raman spectra of the pyrolytic carbon films were found to be much alike to previously reported pyrolyzed resists [20], [53], [65]. As expected, the $I_{(D)}/I_{(G)}$ ratio is reduced from 2.98 to 2.10 as the pyrolysis temperature is raised from 800 to 1100 °C. Based on the $I_{(D)}/I_{(G)}$ ratios, the in-plane crystallite size (L_a) was calculated to increase from 6.45 to 9.15 nm. At the same time, changes in the positions and FWHM of the peaks indicate a continuous buildup of intrinsic stress up to 1000 °C. Upon increasing the pyrolysis temperature to 1100 °C the stress appears to be gradually removed from the material as the crystal structure starts so anneal. To date, very few studies have dealt with the relation between the pyrolysis conditions and the intrinsic stress of pyrolyzed photoresists. The analysis of such relationships are becoming significantly important especially since C-MEMS are starting to expand their use from electrochemical sensors and micro-batteries to micromechanical systems, whose quality can depend on the presence of high levels of intrinsic stress [12].

In conclusion, the results obtained in this work provide an important outlook on the fabrication issues surrounding the development of SU-8 derived suspended pyrolytic carbon microstructures. Further steps towards a better structural stability and higher fabrication success rates can be taken by optimizing the design of the suspended structures, making use

of different sacrificial materials or by utilizing entirely different fabrication methods. Nevertheless, the results obtained in this study will help in the future development of suspended C-MEMS as the complexity in the designs of such systems continues to advance.

Furthermore, the systematic study of different pyrolysis temperatures helps us to better understand the correlation between the pyrolysis conditions and the properties of pyrolytic carbons. Therefore, the results obtain in this study can be used to further develop and optimize the pyrolysis process of polymeric precursors based on the specific application of a C-MEMS device.

References

[1] [1] W. C. Crone, "A Brief Introduction to MEMS and NEMS," in *Springer Handbook of Experimental Solid Mechanics*, 1st edition, pp. 203-228, Springer, 2008.

[2] R. L. McCreery, "Advanced Carbon Electrode Materials for Molecular Electrochemistry," *Chemical Reviews*, vol. 108, no. 7, pp. 2646-2687, 2008.

[3] C. Wang, G. Jia, L. H. Taherabadi, and M. J. Madou, "A Novel Method for the Fabrication of High-Aspect Ratio C-MEMS Structures," *Journal of Microelectromechanical Systems*, vol. 14, no. 2, pp. 348-358, 2005.

[4] C. Wang and M. Madou, "From MEMS to NEMS with carbon," *Biosensors and Bioelectronics*, vol. 20, no. 10, pp. 2181-2187, 2005.

[5] Y. Wang, L. Pham, G. P. S. de Vasconcellos, and M. Madou, "Fabrication and characterization of micro PEM fuel cells using pyrolyzed carbon current collector plates," *Journal of Power Sources*, vol. 195, no. 15, pp. 4796-4803, 2010.

[6] L. Amato, A. Heiskanen, C. Caviglia, F. Shah, K. Zór, M. Skolimowski, M. Madou, L. Gammelgaard, R. Hansen, E. G. Seiz, M. Ramos, T. R. Moreno, A. Martínez-Serrano, S. S. Keller, and J. Emnéus, "Pyrolysed 3D-Carbon Scaffolds Induce Spontaneous Differentiation of Human Neural Stem Cells and Facilitate Real-Time Dopamine Detection," *Advanced Functional Materials*, vol. 24, no. 44, pp. 7042-7052, 2014.

[7] R. Martinez-Duarte, "SU-8 Photolithography as a Toolbox for Carbon MEMS," *Micromachines*, vol. 5, no. 3, pp. 766-782, 2014.

[8] R. Kostecki, X. Y. Song, and K. Kinoshita, "Influence of Geometry on the Electrochemical Response of Carbon Interdigitated Microelectrodes," *Journal of The Electrochemical Society*, vol. 147, no. 5, pp. 1878-1881, 2000.

[9] Y. Lim, J.-I. Heo, M. Madou, and H. Shin, "Monolithic carbon structures including suspended single nanowires and nanomeshes as a sensor platform," *Nanoscale Research Letters*, vol. 8, no. 1, pp. 492, 2013.

[10] K. Malladi, C. Wang, and M. Madou, "Fabrication of suspended carbon microstructures by e-beam writer and pyrolysis," *Carbon*, vol. 44, no. 13, pp. 2602-2607, 2006.

[11] J. Heo, M. Madou, and H. Shin, "Scalable Monolithic Suspended Carbon Nanowire Array Systems as Ultrasensitive Electrochemical Sensing," *15th International Conference on Miniaturized Systems for Chemistry and Life Sciences 2011, MicroTAS 2011*, pp. 1971-1973, 2011.

[12] M. Kurek, F. K. Larsen, P. E. Larsen, S. Schmid, A. Boisen, and S. S. Keller, "Nanomechanical Pyrolytic Carbon Resonators: Novel Fabrication Method and Characterization of Mechanical Properties," *Sensors*, vol. 16, no. 7, pp. 1097-1108, 2016.

[13] J. Kim, X. Song, K. Kinoshita, M. Madou and R. White, "Electrochemical Studies of Carbon Films from Pyrolyzed Photoresist," *Journal of The Electrochemical Society*, vol. 145, no. 7, pp. 2314-2319, 1998.

[14] R. Kostecki, B. Schnyder, D. Alliata, X. Song, K. Kinoshita, and R. Kötz, "Surface studies of carbon films from pyrolyzed photoresist," *Thin Solid Films*, vol. 396, no. 1-2, pp. 36-43, 2001.

[15] S. Ranganathan, R. L. McCreery, S. M. Majji, and M. Madou, "Photoresist-Derived Carbon for Microelectromechanical Systems and Electrochemical Applications," *Journal of The Electrochemical Society*, vol. 147, no. 1, pp. 277 - 282, 2000.

[16] A. Singh, J. Jayaram, M. Madou, and S. Akbar, "Pyrolysis of Negative Photoresists to Fabricate Carbon Structures for Microelectromechanical Systems and Electrochemical Applications," *Journal of The Electrochemical Society*, vol. 149, no. 3, pp. E78-E83, 2002.

[17] B. Y. Park, L. Taherabadi, C. Wang, J. Zoval, and M. J. Madou, "Electrical Properties and Shrinkage of Carbonized Photoresist Films and the Implications for Carbon Microelectromechanical Systems Devices in Conductive Media," *Journal of The Electrochemical Society*, vol. 152, no. 12, pp. J136-J143, 2005.

[18] R. B. Zaouk, "Carbon MEMS from the Nanoscale to the Macroscale: Novel Fabrication Techniques and Applications in Electrochemistry," Doctoral Dissertation, University of California, Irvine, 2008.

[19] Y. M. Hassan, C. Caviglia, S. Hemanth, D. M. A. Mackenzie, D. H. Petersen, and S. S. Keller, "Pyrolytic carbon microelectrodes for impedance based cell sensing," *ECS Transactions*, vol. 72, no. 1, pp. 35-44, 2016.

[20] Y. M. Hassan, C. Caviglia, S. Hemanth, D. M. A. Mackenzie, T. S. Alstrøm, D. H. Petersen, and S. S. Keller, "High temperature SU-8 pyrolysis for fabrication of carbon electrodes," *Journal of Analytical and Applied Pyrolysis*, vol. 125, pp. 91-99, 2017.

[21] B. Pramanick, M. Vazquez-Pinon, A. Torres-Castro, S. O. Martinez-Chapaa, and M. Madou, "Effect of pyrolysis process parameters on electrical, physical, chemical and electro-chemical properties of SU-8-derived carbon structures fabricated using the C-MEMS process," *Materials Today: Proceedings*, vol. 5, no. 3, pp. 9669-9682, 2018.

[22] N. McEvoy, N. Peltekis, S. Kumar, E. Rezvani, H. Nolan, G. P. Keeley, W. J. Blau, and G. S. Duesberg, "Synthesis and analysis of thin conducting pyrolytic carbon films," *Carbon*, vol. 50, no. 3, pp. 1216-1226, 2012.

[23] R. Martinez-Duarte, P. Renaud, and M. J. Madou, "A novel approach to dielectrophoresis using carbon electrodes," *Electrophoresis*, vol. 32, no. 17, pp. 2385-2392, 2011.

[24] S. Jiang, T. Shi, X. Zhan, S. Xi, H. Long, B. Gong, J. Li, S. Cheng, Y. Huang, and Z. Tang, "Scalable fabrication of carbon-based MEMS/NEMS and their applications: a review," *Journal of Micromechanics and Microengineering*, vol. 25, no. 11, pp. 113001, 2015.

[25] R. Martinez-Duarte and M. J. Madou, "SU-8 Photolithography and Its Impact on Microfluidics," in *Microfluidics and Nanofluidics Handbook: Fabrication, Implementation and Applications*, 1st edition, pp. 231-268, CRC Press, 2011.

[26] A. del Campo and C. Greiner, "SU-8: a photoresist for high-aspect-ratio and 3D submicron lithography," *Journal of Micromechanics and Microengineering*, vol. 17, no. 6, pp. R81-R95, 2007.

[27] J. I. Heo, D. S. Shim, G. Turon Teixidor, S. Oh, M. J. Madou, and H. Shin, "Carbon Interdigitated Array Nanoelectrodes for Electrochemical Applications," *Journal of The Electrochemical Society*, vol. 158, no. 3, pp. J76-J80, 2011.

[28] J.-I. Heo, D.-S. Shim, R. Martinez Duarte, M. Madou, and H. Shin, "3-D Carbon Interdigitated Array Nanoelectrodes for Highly Sensitive Sensing of Neurotransmitters," in *14th International Conference on Miniaturized Systems for Chemistry and Life Sciences 2010, MicroTAS 2010*, pp. 1976-1978, 2010.

[29] R. R. Kamath and M. J. Madou, "Three-Dimensional Carbon Interdigitated Electrode Arrays for Redox-Amplification," *Analytical Chemistry*, vol. 86, no. 6, pp. 2963-2971, 2014.

[30] Y. Lim, J.-I. Heo, and H. Shin, "Fabrication and application of a stacked carbon electrode set including a suspended mesh made of nanowires and a substrate-bound planar electrode toward for an electrochemical/biosensor platform," *Sensors and Actuators, B: Chemical*, vol. 192, pp. 796-803, 2014.

[31] J. Lee, D. Sharma, Y. Lim, and H. Shin, "Redox cycling effect at microchannel-integrated sandwich electrodes consisting of a suspended mesh and a substrate-bound planar electrode," *Sensors and Actuators, B: Chemical*, vol. 267, pp. 467-475, 2018.

[32] D. Sharma, J. Lee, and H. Shin, "An electrochemical immunosensor based on a 3D carbon system consisting of a suspended mesh and substrate-bound interdigitated array nanoelectrodes for sensitive cardiac biomarker detection," *Biosensors and Bioelectronics*, vol. 107, pp. 10-16, 2018.

[33] C. Wang, L. Taherabadi, G. Jia, M. Madou, Y. Yeh, and B. Dunn, "C-MEMS for the Manufacture of 3D Microbatteries," *Electrochemical and Solid-State Letters*, vol. 7, no. 11, pp. A435-A438, 2004.

[34] G. T. Teixidor, R. B. Zaouk, B. Y. Park, and M. J. Madou, "Fabrication and characterization of three-dimensional carbon electrodes for lithium-ion batteries," *Journal of Power Sources*, vol. 183, no. 2, pp. 730-740, 2008.

[35] P.-C. Lin, B. Y. Park, and M. J. Madou, "Development and characterization of a miniature PEM fuel cell stack with carbon bipolar plates," *Journal of Power Sources*, vol. 176, no. 1, pp. 207-214, 2008.

[36] M. Beidaghi and C. Wang, "Micro-supercapacitors based on three dimensional interdigital polypyrrole/C-MEMS electrodes," *Electrochimica Acta*, vol. 56, no. 25, pp. 9508-9514, 2011.

[37] G. T. Teixidor, R. A. Gorkin, P. P. Tripathi, G. S. Bisht, M. Kulkarni, T. K. Maiti, T. K. Battacharyya, J. R. Subramaniam, A. Sharma, B. Y. Park, and M. Madou, "Carbon microelectromechanical systems as a substratum for cell growth," *Biomedical Materials*, vol. 3, no. 3, pp. 034116, 2008.

[38] S. Franssila, *Introduction to Microfabrication*, 2nd edition, John Wiley & Sons, 2010.

[39] S. Prakash, and J. Yeom, "Advanced Fabrication Methods and Techniques," in *Nanofluidics and Microfluidics: Systems and Applications*, 1st edition, pp. 87-170, William Andrew, 2014.

[40] D. Sharma, Y. Lim, Y. Lee, and H. Shin, "Glucose sensor based on redox-cycling between selectively modified and unmodified combs of carbon interdigitated array

nanoelectrodes," *Analytica Chimica Acta*, vol. 889, pp. 194-202, 2015.

[41] F. Liu, G. Kolesov, and B. A. Parkinson, "Preparation, Applications, and Digital Simulation of Carbon Interdigitated Array Electrodes," *Analytical Chemistry*, vol. 86, no. 15, pp. 7391-7398, 2014.

[42] B. Si and E. Song, "Recent Advances in the Detection of Neurotransmitters," *Chemosensors*, vol. 6, no. 1, pp. 1, 2018.

[43] M. Politis and O. Lindvall, "Clinical application of stem cell therapy in Parkinson's disease," *BMC Medicine*, vol. 10, no. 1, 2012.

[44] J. A. Lee, S. W. Lee, K.-C. Lee, S. I. Park, and S. S. Lee, "Fabrication and characterization of freestanding 3D carbon microstructures using multi-exposures and resist pyrolysis," *Journal of Micromechanics and Microengineering*, vol. 18, no. 3, pp. 035012, 2008.

[45] S. Hemanth, C. Caviglia, and S. S. Keller, "Suspended 3D pyrolytic carbon microelectrodes for electrochemistry," *Carbon*, vol. 121, pp. 226-234, 2017.

[46] J.-I. Heo, Y. Lim, and H. Shin, "The effect of channel height and electrode aspect ratio on redox cycling at carbon interdigitated array nanoelectrodes confined in a microchannel," *Analyst*, vol. 138, no. 21, pp. 6404-6411, 2013.

[47] A. Hai, J. Shappir, and M. E. Spira, "In-cell recordings by extracellular microelectrodes," *Nature Methods*, vol. 7, no. 3, pp. 200-202, 2010.

[48] S. M. Ojovan, N. Rabieh, N. Shmoel, H. Erez, E. Maydan, A. Cohen, and M. E. Spira, "A feasibility study of multi-site, intracellular recordings from mammalian neurons by extracellular gold mushroom-shaped microelectrodes," *Scientific Reports*, vol. 5, pp. 14100, 2015.

[49] R. P. Feynman, "There's Plenty of Room at the Bottom: An invitation to enter a new field of physics," in *Engineering and Science*, vol. 23, no. 5, pp. 22-36, 1960.

[50] MicroChemicals, "Chromium Etching," Available online at: *www.microchemicals.com/downloads/application_notes.html*, March 2019.

[51] MicroChemicals, "Wet-Chemical Etching of Silicon and SiO_2," Available online at: *www.microchemicals.com/downloads/application_notes.html*, March 2019.

[52] N. Maluf and K. Williams, *An Introduction to Microelectromechanical Systems Engineering*, 2nd edition, Artech House Inc., 2004.

[53] A. Mardegan, R. Kamath, S. Sharma, P. Scopece, P. Ugo, and M. Madou, "Optimization of Carbon Electrodes Derived from Epoxy-based Photoresist," *Journal of the Electrochemical Society*, vol. 160, no. 8, pp. B132-B137, 2013.

[54] K. Jurkiewicz, M. Pawlyta, D. Zygadło, D. Chrobak, S. Duber, R. Wrzalik, A. Ratuszna, and A. Burian, "Evolution of glassy carbon under heat treatment: correlation structure–mechanical properties," *Journal of Materials Science*, vol. 53, no. 5, pp. 3509-3523, 2018.

[55] P. Lucas and A. Marchand, "Pyrolytic carbon deposition from methane: An analytical approach to the chemical process," *Carbon*, vol. 28, no. 1, pp. 207-219, 1990.

[56] D. J. Roddy and C. Manson-Whitton, "Biomass Gasification and Pyrolysis," in

Comprehensive Renewable Energy, vol. 5, pp. 133-153, 2012.

[57] S. Sharma, "Glassy Carbon: A Promising Material for Micro- and Nanomanufacturing," *Materials*, vol. 11, no. 10, pp. 1857, 2018.

[58] S. Sharma, A. Sharma, Y.-K. Cho, and M. Madou, "Increased Graphitization in Electrospun Single Suspended Carbon Nanowires Integrated with Carbon-MEMS and Carbon-NEMS Platforms," *ACS Applied Materials and Interfaces*, vol. 4, no. 1, pp. 34-39, 2012.

[59] J. Robertson, "Diamond-like amorphous carbon," *Materials Science and Engineering: R: Reports*, vol. 37, no. 4-6, pp. 129-281, 2002.

[60] A. C. Ferrari and J. Robertson, "Raman spectroscopy of amorphous, nanostructured, diamond-like carbon, and nanodiamond," *Philosophical Transactions of the Royal Society A: Mathematical, Physical and Engineering Sciences*. vol. 362, no. 1824, pp. 2477-2512, 2004.

[61] S. Jiang, T. Shi, Y. Gao, H. Long, S. Xi, and Z. Tang, "Fabrication of a 3D micro/nano dual-scale carbon array and its demonstration as the microelectrodes for supercapacitors," *Journal of Micromechanics and Microengineering*, vol. 24, no. 4, pp. 045001, 2014.

[62] H. Fredriksson, D. Chakarov, and B. Kasemo, "Patterning of highly oriented pyrolytic graphite and glassy carbon surfaces by nanolithography and oxygen plasma etching," *Carbon*, vol. 47, no. 5, pp. 1335-1342, 2009.

[63] S. Yamada and H. Sato, "Some Physical Properties of Glassy Carbon," *Nature*, vol. 193, no. 4812, pp. 261-262, 1962.

[64] W. S. Rothwell, "Small-Angle X-Ray Scattering from Glassy Carbon," *Journal of Applied Physics*, vol. 39, no. 3, pp. 1840-1845, 1968.

[65] E. Peltola, J. J. Heikkinen, K. Sovanto, S. Sainio, A. Aarva, S. Franssila, V. Jokinen, and T. Laurila, "SU-8 based pyrolytic carbon for the electrochemical detection of dopamine," *Journal of Materials Chemistry B*, vol. 5, no. 45, pp. 9033–9044, 2017.

[66] K. Jurkiewicz, S. Duber, and A. Burian, "Paracrystalline Structure of Glass-Like Carbons," *International Journal of Applied Glass Science*, vol. 7, no. 3, pp. 355-363, 2016.

[67] G. M. Jenkins and K. Kawamura, "Structure of Glassy Carbon," *Nature*, vol. 231, pp. 175-176, 1971.

[68] P. J. F. Harris, "Fullerene-related structure of commercial glassy carbons," *Philosophical Magazine*, vol. 84, no. 29, pp. 3159-3167, 2004.

[69] A. C. Ferrari and J. Robertson, "Interpretation of Raman spectra of disordered and amorphous carbon," *Physical Review B - Condensed Matter and Materials Physics*, vol. 61, no. 20, pp. 14095-14107, 2000.

[70] A. C. Ferrari and J. Robertson, "Resonant Raman spectroscopy of disordered, amorphous, and diamondlike carbon," *Physical Review B - Condensed Matter and Materials Physics*, vol. 64, pp. 075414, 2001.

[71] P. K. Chu and L. Li, "Characterization of amorphous and nanocrystalline carbon films," *Materials Chemistry and Physics*, vol. 96, no. 2-3, pp. 253-277, 2006.

[72] J. M. Vallerot, X. Bourrat, A. Mouchon, and G. Chollon, "Quantitative structural and textural assessment of laminar pyrocarbons through Raman spectroscopy, electron diffraction and few other techniques," *Carbon*, vol. 44, no. 9, pp. 1833-1844, 2006.

[73] E. del Corro, M. Taravillo, and V. G. Baonza, "Nonlinear strain effects in double-resonance Raman bands of graphite, graphene, and related materials," *Physical Review B - Condensed Matter and Materials Physics*, vol. 85, no. 3, pp. 033407, 2012.

[74] N. Ferralis, "Probing mechanical properties of graphene with Raman spectroscopy," *Journal of Materials Science*, vol. 45, no. 19, pp. 5135-5149, 2010.

[75] L. G. Caṇado, K. Takai, T. Enoki, M. Endo, Y. A. Kim, H. Mizusaki, A. Jorio, L. N. Coelho, R. Magalhães-Paniago, and M. A. Pimenta, "General equation for the determination of the crystallite size L_a of nanographite by Raman spectroscopy," *Applied Physics Letters*, vol. 88, no. 16, pp. 163106, 2006.

[76] M. S. Dresselhaus, G. Dresselhaus and P. C. Eklund, *Science of Fullerenes and Carbon Nanotubes*, 1st edition, Academic Press, 1996.

[77] M. Scarselli, P. Castrucci, and M. De Crescenzi, "Electronic and optoelectronic nano-devices based on carbon nanotubes," *Journal of Physics: Condensed Matter*, vol. 24, no. 31, pp. 313202, 2012.

[78] A. Altuna, J. Berganzo, and L. J. Fernández, "Polymer SU-8-based microprobes for neural recording and drug delivery," *Frontiers in Materials*, vol. 2, no. 47, 2015.

[79] R. Yang and W. Wang, "A numerical and experimental study on gap compensation and wavelength selection in UV-lithography of ultra-high aspect ratio SU-8 microstructures," *Sens. Actuator B-Chem*, vol. 110, no. 2, pp. 279-288, 2005.

[80] W. Dai, K. Lian, and W. Wang, "A quantitative study on the adhesion property of cured SU-8 on various metallic surfaces," *Microsystem Technologies*, vol. 11, no. 7, pp. 526-534, 2005.

[81] MicroChem, "SU-8 50-100 Data Sheet," Avialable online at: *www.microchem.com/pdf/SU8_50-100.pdf*, March 2019.

[82] R. L. Barber, M. K. Ghantasala, R. Divan, K. D. Vora, E. C. Harvey, and D. C. Mancini, "Optimisation of SU-8 processing parameters for deep X-ray lithography," *Microsystem Technologies*, vol. 11, no. 4-5, pp. 303-310, 2005.

[83] H. Namatsu, K. Kurihara, M. Nagase, K. Iwadate, and K. Murase, "Dimensional limitations of silicon nanolines resulting from pattern distortion due to surface tension of rinse water," *Applied Physics Letters*, vol. 66, no. 20, pp. 2655-2657, 1995.

[84] P. Abgrall, V. Conedera, H. Camon, A. M. Gue, and N. T. Nguyen, "SU-8 as a structural material for labs-on-chips and microelectromechanical systems," *Electrophoresis*, vol. 28, no. 24, pp. 4539-4551, 2007.

[85] Z. Cui and R. A. Lawes, "A new sacrificial layer process for the fabrication of micromechanical systems," *Journal of Micromechanics and Microengineering*, vol. 7, no. 3, pp. 128–130, 1997.

[86] I. Song and P. K. Ajmera, "Use of a photoresist sacrificial layer with SU-8 electroplating mould in MEMS fabrication," *Journal of Micromechanics and Microengineering*, vol. 13, no. 6, pp. 816-821 2003.

[87] V. Seidemann, J. Rabe, M. Feldmann, and S. Büttgenbach, “SU8-micromechanical structures with in situ fabricated movable parts,” *Microsystem Technologies*, vol. 8, no. 4-5, pp. 348-350, 2002.

[88] V. Conédéra, L. Salvagnac, N. Fabre, F. Zamkotsian, and H. Camon, “Surface micromachining technology with two SU-8 structural layers and sol-gel, SU-8 or SiO_2/sol-gel sacrificial layers,” *Journal of Micromechanics and Microengineering*, vol. 17, no. 8, pp. N52-N57, 2007.

[89] S. D. Psoma and D. W. K. Jenkins, “Comparative assessment of different sacrificial materials for releasing SU-8 structures,” *Reviews on Advanced Materials Science*, vol. 10, pp. 149-155, 2005.

[90] J. Liu, B. Cai, J. Zhu, D. Chen, Y. Li, J. Zhang, G. Ding, X. Zhao, and C. Yang, “A novel device of passive and fixed alignment of optical fiber,” *Microsystem Technologies*, vol. 10, no. 4, pp. 269-271, 2004.

[91] MicroChemicals, “General Properties of AZ/ TI Photoresists,” Available online at: *www.microchemicals.com/downloads/application_notes.html*, March 2019.

[92] MicroChemicals, “Spin-coating of Photoresists,” Available online at: *www.microchemicals.com/downloads/application_notes.html*, March 2019.

[93] MicroChemicals, “Exposure of Photoresists,” Available online at: *www.microchemicals.com/downloads/application_notes.html*, March 2019.

[94] MicroChemicals, “Development of Photoresists,” Available online at: *www.microchemicals.com/downloads/application_notes.html*, March 2019.

[95] MicroChemicals, “Photoresist Removal,” Available online at: *www.microchemicals.com/downloads/application_notes.html*, March 2019.

[96] A. Hartley, R. Miles, N. Dimitrakopoulos, and R. D. Pollard, “SU-8 Beams and Membranes,” *1st EMRS DTC Technical Conference*, 2004.

[97] M. de Jesus Maciel, R. P. Rocha, J. P. Carmo, and J. H. Correia, “Measurement and statistical analysis toward reproducibility validation of AZ4562 cylindrical microlenses obtained by reflow,” *Measurement: Journal of the International Measurement Confederation*, vol. 49, pp. 60-67, 2014.

[98] G. Sengo, H. a. G. M. van Wolferen, and A. Driessen, “Optimized Deep UV Curing Process for Metal-Free Dry-Etching of Critical Integrated Optical Devices,” *Journal of The Electrochemical Society*, vol. 158, no. 10, pp. H1084-H1089, 2011.

[99] F. Ceyssens and R. Puers, “Creating multi-layered structures with freestanding parts in SU-8,” *Journal of Micromechanics and Microengineering*, vol. 16, no. 6, pp. S19-S23, 2006.

[100] J. Melai, V. M. Blanco Carballo, C. Salm, and J. Schmitz, “Suspended membranes, cantilevers and beams using SU-8 foils,” *Microelectronic Engineering*, vol. 87, no. 5-8, pp. 1274-1277, 2010.

[101] P. Abgrall, C. Lattes, V. Conédéra, X. Dollat, S. Colin, and A. M. Gué, “A novel fabrication method of flexible and monolithic 3D microfluidic structures using lamination of SU-8 films,” *Journal of Micromechanics and Microengineering*, vol. 16, no. 1, pp. 113-121, 2006.

[102] F. J. Blanco, M. Agirregabiria, J. Garcia, J. Berganzo, M. Tijero, M. T. Arroyo, J. M. Ruano, I. Aramburu, and K. Mayora, "Novel three-dimensional embedded SU-8 microchannels fabricated using a low temperature full wafer adhesive bonding," *Journal of Micromechanics and Microengineering*, vol. 14, no. 7, pp. 1047-1056, 2004.

[103] S. Tuomikoski and S. Franssila, "Free-standing SU-8 microfluidic chips by adhesive bonding and release etching," *Sensors and Actuators, A: Physical*, vol. 120, no. 2, pp. 408-415, 2005.

[104] S. Sharma, R. Kamath, and M. Madou, "Porous glassy carbon formed by rapid pyrolysis of phenol-formaldehyde resins and its performance as electrode material for electrochemical double layer capacitors," *Journal of Analytical and Applied Pyrolysis*, vol. 108, pp. 12-18, 2014.

[105] Z. Tang, T. Shi, J. Gong, L. Nie, and S. Liu, "An optimized process for fabrication of high-aspect-ratio photoresist-derived carbon microelectrode array on silicon substrate," *Thin Solid Films*, vol. 518, no. 10, pp. 2701-2706, 2010.

[106] A. M. Lyons, L. P. Hale and C. W. Wilkins, "Photodefinable carbon films: Control of image quality," *Journal of Vacuum Science & Technology B: Microelectronics and Nanometer Structures*, vol. 3, no. 1, pp. 447-452, 1985.

[107] R. Natu, M. Islam, J. Gilmore, and R. Martinez-Duarte, "Shrinkage of SU-8 microstructures during carbonization," *Journal of Analytical and Applied Pyrolysis*, vol. 131, pp. 17-27, 2018.

[108] E. Fitzer and W. Schäfer, "The effect of crosslinking on the formation of glasslike carbons from thermosetting resins," *Carbon*, vol. 8, no. 3, pp. 353-364, 1970.

[109] R. Natu, M. Islam, and R. Martinez-Duarte, "Shrinkage Analysis of Carbon Micro Structures Derived from SU-8 Photoresist," *ECS Transactions*, vol. 72, no. 1, pp. 27-33, 2016.

[110] S. Keller, D. Haefliger, and A. Boisen, "Fabrication of thin SU-8 cantilevers: initial bending, release and time stability," *Journal of Micromechanics and Microengineering*, vol. 20, no. 4, pp. 045024, 2010.

[111] H. Zhang, G. Lee, C. Gong, L. Colombo, and K. Cho, "Grain Boundary Effect on Electrical Transport Properties of Graphene," *Journal of Physical Chemistry C*, vol. 118, no. 5, pp. 2338-2343, 2014.

[112] R. A. Serway, *Principles of physics*, 2nd edition, Saunders College Pub, 1998.

[113] C. G. Granqvist and A. Hultåker, "Transparent and conducting ITO films: new developments and applications," in *Thin Solid Films*, vol. 411, no. 1, pp. 1-5, 2002.

[114] A. Merlen, J. Buijnsters, and C. Pardanaud, "A Guide to and Review of the Use of Multiwavelength Raman Spectroscopy for Characterizing Defective Aromatic Carbon Solids: from Graphene to Amorphous Carbons," *Coatings*, vol. 7, no. 10, pp. 153, 2017.

[115] V. Brunetti, G. Maiorano, L. Rizzello, B. Sorce, S. Sabella, R. Cingolani, and P. P. Pompa, "Neurons sense nanoscale roughness with nanometer sensitivity," *Proceedings of the National Academy of Sciences*, vol. 107, no. 14, pp. 6264-6269, 2010.